MEASUREMENT OF THE UNPOLARIZED $K^+\Lambda$ AND $K^+\Sigma^0$ ELECTROPRODUCTION CROSS-SECTION OFF THE PROTON WITH KAOS-SPECTROMETER

DISSERTATION
zur Erlangung des Grades "Doktor der Naturwissenschaften"
am Fachbereich Physik, Mathematik und Informatik
der Johannes Gutenberg-Universität Mainz

Salvador Sánchez Majos
geboren in Alicante, Spain

Institüt für Kernphysik
Johannes Gutenberg-Universität Mainz
February 2012

ABSTRACT

The new stage of the Mainz Microtron, MAMI, at the Institute for Nuclear Physics of the Johannes Gutenberg-University, operational since 2007, allows open strangeness experiments to be performed. Covering the lack of electroproduction data at very low Q^2, $p(e, K^+)\Lambda$ and $p(e, K^+)\Sigma^0$, reactions have been studied at $Q^2 = 0.036(GeV/c)^2$ and $Q^2 = 0.05(GeV/c)^2$ in a large angular range. Cross-section at W=1.75 GeV will be given in angular bins and compared with the predictions of Saclay-Lyon and Kaon Maid isobaric models. We conclude that the original Kaon-Maid model, which has large longitudinal couplings of the photon to nucleon resonances, is unphysical.

Extensive studies for the suitability of silicon photomultipliers as read out devices for a scintillating fiber tracking detector, with potential applications in both positive and negative arms of the spectrometer, will be presented as well.

PUBLICATIONS

Some ideas and figures have previously appeared in the following publications:

[I] S. Sánchez Majos, P. Achenbach, and J. Pochodzalla, *Efficiency studies for a tracking detector based on square, 1.5m long scintillating fibers read out by SiPM*, Nucl. Instr. and Meth. in Phys. Res. A 610 (2009) 502-508.

[II] P. Achenbach, A. Sánchez Lorente, S. Sánchez Majos, and J. Pochodzalla, *Future use of silicon photomultipliers for* KAOS *at MAMI and Panda at FAIR*, Nucl. Instr. and Meth. in Phys. Res. A 610 (2009) 358-361.

[III] S. Sánchez Majos et al. (A1 Collaboration), *Noise and radiation damage in silicon photomultipliers exposed to electromagnetic and hadronic irradiation*, Nucl. Instr. and Meth. in Phys. Res. A 602 (2009) 506-510.

[IV] S. Sánchez Majos, P. Achenbach, and J. Pochodzalla, *Characterisation of radiation damage in silicon photomultipliers with a Monte Carlo model*, Nucl. Instr. and Meth. in Phys. Res. A 594 (2008) 351-357.

[V] P. Achenbach (A1 Collaboration) *Exclusive electroproduction of* K^+ Λ *and* K^+ Σ^0 *final states at* Q^2 = *0.030-0.055 (GeV/c)*^{2}, Eur. Phys. J. A (2012), in press.

[VI] P. Achenbach (A1 Collaboration) *Strange hadrons - strangeness in strongly interacting particles*, Eur. Phys. J. ST 198 (2011) 307-327

CONTENTS

I KAON ELECTROPRODUCTION OFF THE PROTON AT LOW MOMENTUM TRANSFER: THEORETICAL FRAMEWORK AND DIFFERENTIAL CROSS-SECTION MEASUREMENT 1

1 INTRODUCTION 3
- 1.1 Particles, fields and reductionism 3
- 1.2 Scope of the present work 6
- 1.3 Kinematics and cross-section structure 8
- 1.4 Theoretical models 10
- 1.5 Kaon-Maid and Saclay-Lyon isobaric models 14
- 1.6 Previous experiments 20

2 EXPERIMENTAL SETUP AND DATA ACQUISITION 25
- 2.1 Overview 25
- 2.2 Electron beam 25
- 2.3 Target 26
- 2.4 KAOS spectrometer 29
  - 2.4.1 Dipole magnet 29
  - 2.4.2 Experimental determination of transfer matrix. Collimators 32
  - 2.4.3 Dipole field characterization and read out 34
  - 2.4.4 Multiwire proportional chambers 34
  - 2.4.5 Scintillator walls 36
- 2.5 KAOS single arm Trigger 40
- 2.6 Spectrometer B 43
  - 2.6.1 Spectrometer B detector package 43
  - 2.6.2 Scintillator walls 44
  - 2.6.3 Cerenkov detector 44
- 2.7 Coincidence setting 45
- 2.8 Data acquisition and analysis software 47
- 2.9 Kinematical setting 48

3 DETECTION EFFICIENCIES AND DATA ANALYSIS 51
- 3.1 Overview 51
- 3.2 Tracking efficiency 52
  - 3.2.1 Phenomenology of MWPC signals and track reconstruction ambiguities 52
  - 3.2.2 Cluster analysis 54
  - 3.2.3 Track finding method 55
  - 3.2.4 Efficiency counters 55
  - 3.2.5 Scintillator walls top-bottom timing used for vertical position reconstruction 58
  - 3.2.6 Efficiency definition and results 61
- 3.3 Scintillator walls inefficiencies 63

3.4 Collected data and runs selection 65
3.5 Particle identification 67
3.6 Generic cuts applied to the data 69
3.7 Reaction channel ID 73
3.8 Scaling method for cross-section extraction and Monte Carlo simulation 73
3.9 Systematic errors 78
4 CONCLUSIONS 81

II FEASIBILITY STUDIES FOR TRACKING DETECTORS 87
5 PROTOTYPING AND EFFICIENCY MEASUREMENTS 91
5.1 Introduction 91
5.2 Experimental set-up 91
5.3 Experimental results 95
5.4 Detection efficiencies for highly relativistic electrons 98
5.5 Modeling of long scintillating fibers read out by SiPM 98
6 NOISE AND RADIATION DAMAGE 103
6.1 Introduction 103
6.2 SiPM characterization 103
6.3 SiPM irradiation with the electron beam 104
6.4 SiPM irradiation by hadronic and electromagnetic background 106
6.5 Damage characterisation with a Monte Carlo model 109
6.5.1 The Monte Carlo model for the detector output 109
6.5.2 Observed damage 114
7 CONCLUSIONS 117
A THEORETICAL BACKGROUND 119
A.1 Overview 119
A.2 Transition charge density 120
A.3 Relativistic scattering in an external electromagnetic field 121
A.4 Scattering in the field of the evolving hadronic system 123
A.5 From the S matrix to the cross-section. The leptonic and hadronic Tensors 125
A.6 Constrains on the cross section structure due to Gauge invariance 127
A.7 Explicit form of the leptonic tensor 128
A.8 ϕ dependence 130
A.9 Final expression for the cross-section 131
A.10 Virtual and real photons 132

BIBLIOGRAPHY 137

Part I

KAON ELECTROPRODUCTION OFF THE PROTON AT LOW MOMENTUM TRANSFER: THEORETICAL FRAMEWORK AND DIFFERENTIAL CROSS-SECTION MEASUREMENT

1 INTRODUCTION

The order and connection of ideas is the same as the order and connection of things.

— Spinoza, Prop. 7, Part.II, Ethics

1.1 PARTICLES, FIELDS AND REDUCTIONISM. A SHORT PHILOSOPHICAL EXCURSUS IN AN EXPERIMENTALIST THESIS

Twentieth century will be remembered as truly revolutionary in the history of physics. The reason is twofold: First, a complete new conceptual framework was introduced; resulting in a new quantum-relativistic paradigm, the principles of which had to be satisfied by any physical theory. Second, new laws were discovered for three of the four fundamental known interactions (although one of them escaped all attempts of quantization).

Admittedly, the conceptual difficulties related with quantum mechanics (and also, but more subtlety, with the theory of relativity[1]), might be considered as the result of an unfinished revolution, and new ideas could be necessary for a conceptually satisfying (and maybe deeper) description of the physical world. But, as Newton laws will always have validity in a restricted sense, the theoretical constructions of relativistic quantum field theory will survive as a powerful set of ideas for a detailed description of particle physics.

Even so, there is -within the existing paradigm- a hint of a completely different issue that sits at the very roots of the idea of science itself. Ironically, this difficulty is also a part of the scientific production of the last century, and the result of the non linear structure of the discovered field equations from which non trivial emergent behavior is suspected (or already known[2]). Properties of non-linear systems cannot be aggregatively obtained from their constituents [2]. We will see later that hadrons are highly mysterious objects, for which an structural picture analogous to the successful atomic theory might be too naive. In fact, the very concept of constituent blocks or particles is somehow alien to interactive quantum field theory [3, 4].

Since the formulation of the special theory of relativity, it was a must for any physical theory to fulfill the stringent symmetry principle of

1 For a delightful description of the major epistemological defect of special relativity (in Einstein words) see [1].

2 In the case of QCD, notorious examples are constituent quarks and confinement. None of these is obvious from the QCD Lagrangian.

Lorentz invariance. Non relativistic theories could still deal with low speed phenomena, but they had to be considered just approximations of more general covariant laws. When relativistic wave equations were studied, it become clear that the interpretation of the wave function as a probability amplitude was untenable; and the only way out of the many encountered problems was a second quantization where the functions of space and time, previously considered as mathematical tools for the description of particles, had to be taken as the actual physical entities to be quantized [5]. Particle phenomenology was a byproduct of quantum mechanical field behavior. That this was really the case became more and more transparent when quantum fields were studied in curved space-times, where the field equations were modified by the presence of the nontrivial backgrounds and the demand of general covariance. Fock spaces could not be constructed in a natural way from these modified equations and asymptotic states could only be employed for some particular metrics. In a certain way, the whole space was the interaction region. Quoting Wald [3], we might say: "The particle interpretation/description of quantum field theory in flat space-time has been remarkably successful to the extent that one might easily get the impression that, at a fundamental level, quantum field theory is really a theory of particles. Note, however, that the definition and interpretation of particle states relies heavily on the presence of a time translation symmetry."

A naive but quite extended approach to "particle physics" seems to lead towards the idea of a hierarchical structure in nature, giving rise to the possibility of a truly reductionist point of view concerning scientific theories.

Each science has its own entities and laws, seen as the result of the dynamics of more fundamental objects, which in turn can be split in a downer level into another entities and rules. This prejudice has received support from several sciences where the reduction has been partially achieved. As a paradigmatic example, the successful explanation of the hydrogen atom properties in terms of the interaction of an "electron" and a "proton" seems to validate this idea. It is really remarkable that the complex dynamics of the coupled electromagnetic and Dirac quantum fields can be compressed into such a simple model and there is a priori no reason to think that such a strong reduction will be possible for other interacting fields.

This "ontological weakness" of the entities is of high relevance in hadronic physics. Although exotic phases with quarks and gluons as convenient degrees of freedom are predicted by QCD in extreme situations, most of the collected experimental data concerns the physics of hadrons. In fact, quarks were suggested in 1964 as a convenient way of organizing the plethora of baryons and mesons discovered in particle accelerators or in experiments with cosmic rays. As bound states of QCD, hadron properties should be, at least in principle,

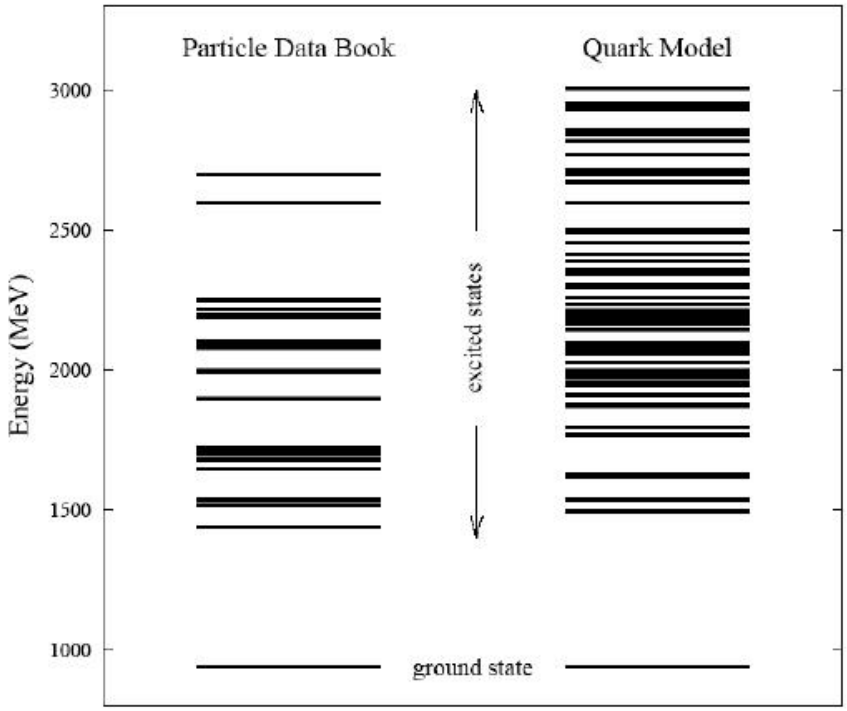

Figure 1: Nucleon resonances as reported by Particle Data Group and as predicted by a constituent quark model [6].

theoretically computable. Unfortunately, perturbative methods are useless for this purpose due to the large value of the coupling constant describing the strength of the interaction among quarks and gluons within a hadron. The original heuristic picture from which rigorous QCD was derived has been developed to the point of being able to predict a rich spectrum of hadronic resonances. The so called "constituent quark model", which treats baryons as a composition of three valence quarks, has been very successful in predicting many measured properties. Constituent quarks means massive quarks, in contrast to the nearly massless u, d, s quarks of the QCD Lagrangian. A qualitative explanation for the appearance of these masses is the spontaneous chiral symmetry breaking, but it is far from obvious how the transition from the expected "soup of quark and gluon fields" to the three valence quarks actually happens. Indeed, it is not even clear whether or not this simple model contains the necessary ingredients to accurately match the actual hadronic spectrum. The constituent quark model seems to predict too many states as compared to the actual observed resonances (see Fig. 1). These so called "missing resonances" could be the result of an oversimplified model or just the indication of an inappropriate excitation method. This last explanation has been supported by Capstick and Roberts [6] who suggested that some missing resonances couple strongly to hyperon final state channels of photoproduction. Their model predicts that a number of them will

appear in the $K + \Lambda$ channel. Photo and electro-production processes have been studied by means of isobaric models (see section 2.12). This models use a set of interchanged resonances for the description of the reaction. This intermediate language has been developed in much the same way as chemistry speaks about different substances participating in their reactions. If these models are correct, the need of one of the "missing resonances" for a correct description of the experimental data might be considered as partial evidence for its existence. Clearly, a solution of this "missing resonances" problem would be very valuable for guiding theoretical efforts of understanding the dynamics and origin of valence quarks from QCD, the success of which would be a proof of its validity in the hadronic energy scale.

As a first step in an ambitious program dedicated to strangeness physics at the Mainz Microtron (MAMI), the reactions $p(e, K^+)\Lambda$ and $p(e, K^+)\Sigma^0$ have been studied with an specialized spectrometer in a kinematical region not covered yet by any previous experiment. These interesting reactions sit exactly at the interface between a hadron and a quark description of nuclei and subnuclear processes. As compared to the simpler case of pion production, the dynamics of strangeness production is known to be more involved since the large strange quark mass sets a reaction threshold in the so called third resonance region where many excited states of the proton can be created.

The physical results provided in this research will contribute to the world data-base for the complete experimental characterization of these important reactions. Hadrodynamic theories are still poorly constrained by the existing data (specially for the case of electroproduction) but severe difficulties have already been experienced when trying to describe some observables. It is still an open and very interesting question, as we have seen, whether or not this hadronic "entities" governed by the "laws" dictated by effective lagrangians will be able to capture in detail the observed experimental phenomenology.

1.2 SCOPE OF THE PRESENT WORK

The door to strangeness production was opened at the Institute for Nuclear Physics in Mainz with the upgrading of the electron accelerator. Since Feb 2007, the MAMI-C accelerator facility is operational allowing energies up to 1.6 GeV. The study of these new reaction channels was not possible with any of the existing spectrometers in the experimental hall of the A1 collaboration since their central track length was too long for an efficient detection of the short living strange mesons. As a fundamental part of this thesis, the participation in the setting up of a new short orbit magnetic spectrometer optimized for kaon detection (KAOS) will be described. KAOS was successfully operated at the GSI facilities for many years having an important list of scientific achievements. This thesis will present the first physical

results obtained with the spectrometer after its installation in Mainz. Extensive studies for the suitability of a large tracking detector based on long scintillating fibers read out by a new and promising type of solid state photon detector will also be shown.

The organization of the contents is as follows:

PART I:

Chapter 1: We will first set the stage by discussing the kinematics and the general structure of the cross-section in kaon electroproduction reactions. Effective hadrodynamic theories, used for modeling this process, will be presented next with some detail for their later comparison with our measured results. We will finish by reviewing previous experimental efforts, both in photo and electroproduction reactions.

In chapter 2, we provide a complete description of the experimental setup used for the coincident detection of K^+ and e^- needed for reaction characterization. Calibration work performed during the setting up of KAOS spectrometer will be presented as well. The new flexible tracking trigger based on FPGA logic modules conceived to minimize random coincidences generated by the large electromagnetic background is also discussed. The two kinematic settings analyzed in this thesis and measured during the years 2008 and 2009 are presented in this chapter since they involved an experimental challenge due to the minimum angle needed for the electron spectrometer.

Chapter 3 begins with a detailed description of the spectrometer characterization, both by dedicated efficiency measurements and computer simulations. A careful study of the inefficiencies caused by the aged scintillator walls and their particular geometry motivates a proposal for a renewed wall. The analysis of the physics runs performed during the years 2008 and 2009 is explained. Differential cross-sections for Λ and Σ^0 electroproduction at very low momentum transfer are given for angular bins. The chapter continues with a brief discussion of systematic errors and finishes with the introduction of the model dependent scaling method for the cross-section extraction used to optimize the existing statistics.

Finally, chapter 4 will address the physical significance of the results obtained in this experiment.

PART II consisting on chapters 5, 6 and 7, is a substantial component of this thesis. It presents an extensive study carried out in parallel to KAOS construction and cross-section measurement about the feasibility of a long scintillating fiber based tracking detector read out by a promising new type of photon detector: silicon photomultiplier. Results on radiation hardness, efficiency measurements for a prototype and computer modeling are shown. This investigations were very welcome by the community since at the time of their publication

there was almost no information for researchers who wanted to make use of these new type of detectors.

Appendix A presents a detailed derivation of the general structure of kaon electroproduction cross-section. This departure from standard schematic presentations typically encountered in experimental thesis is the result of my personal interest in theoretical physics and it attempts to provide a useful reference for a better understanding of the presented results and a unified source for future students. It is the hope of this author that the effort to compile and digest the material used for this derivation had resulted in a pedagogical presentation at a level easily understandable for experimentalists.

1.3 KINEMATICS OF $e + p \rightarrow e' + K^+ + Y$ AND CROSS-SECTION STRUCTURE

In the standard terminology used in inelastic scattering, hyperon electroproduction off the proton, where the outgoing electron and kaon are detected in coincidence and the produced Λ or Σ^0 is reconstructed, is called an exclusive reaction [7].

Full kinematical characterization of the reaction is given by the following five four momenta:

- $p_e = (E_e, \vec{p}_e)$ for the incident electron.
- $p'_e = (E'_e, \vec{p'}_e)$ for the scattered electron.
- $p_p = (m_p, \vec{0})$ for the proton target.
- $p_K = (E_k, \vec{p}_k)$ for the produced kaon.
- $p_Y = (E_Y, \vec{p}_Y)$ for the unobserved hyperon.

where the components of the four vectors have been given in the lab frame where the proton is at rest.

Energy-momentum conservation for this reaction expressed by $p_e + p_p = p'_e + p_Y + p_K$ imposes 4 conditions upon the 20 kinematical variables. Since all particles are on their mass shell ($p^2 = m^2$), five extra degrees of freedom are eliminated. Electron and proton initial states are under the experimentalist control leaving finally only $20 - 4 - 5 - 6 = 5$ variables free. The scattered electron transfers energy and momentum to the proton by interchanging a virtual photon with four momentum $q_\mu = p_{e_\mu} - p'_{e_\mu} = (\omega, \vec{q})$. The Lorentz invariant formed by squaring this four vector is usually called in the literature the four momentum transfer or simply the momentum transfer. It is easy to prove that for relativistic electrons in the lab frame we have:

$$Q^2 = -(q_\mu)^2 \approx 4E_e E'_e \sin^2 \frac{\theta_e}{2} \tag{1.1}$$

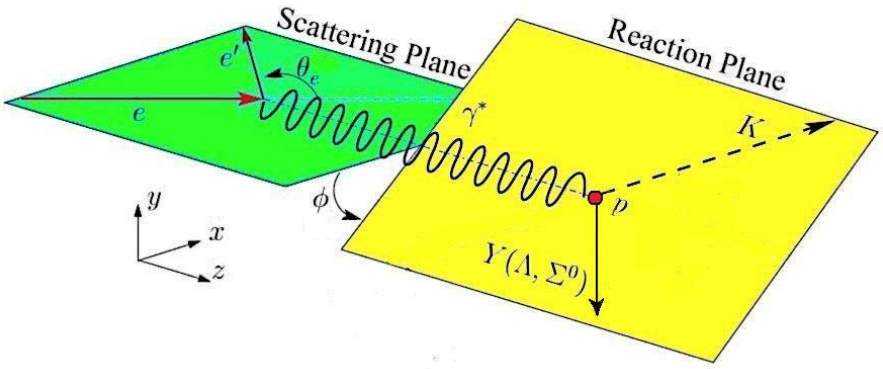

Figure 2: The electron scattering and hadronic reaction planes. Note that for photoproduction there is no scattering plane.

Another important invariant is the mass squared of the system recoiling against the electron (i.e. the virtual photon-proton system) usually called center of mass energy.

$$s = W^2 = (q_\mu + p_\mu)^2 = M_p^2 - Q^2 + 2M_p(E_e - E'_e) \tag{1.2}$$

Where again the last expression holds in the lab frame where the proton is at rest.

The electroproduction cross-section is usually expressed in a form useful for comparison with photo-production experiments in terms of the kaon center-of-mass angles. As we have seen, energy momentum conservation, mass shell conditions and initial proton and electron state knowledge allows the coincidence cross-section to be written in terms of a five-fold differential cross section:

$$\frac{d^5\sigma}{dE'_e d\Omega_{e'} d\Omega^*_K} \tag{1.3}$$

In this expression, angles and energy are chosen since those are variables directly related with the experimental arrangement.

The connection to photoproduction experiments can be made even closer if we replace the electron variables $(\cos\theta_e, E'_e)$ in (1.3) by (W, Q^2) and integrate out the electron azimuthal angle ϕ_e (since clearly only the relative angle between the electron scattering plane and the hadronic plane defined by the outgoing hyperon and kaon have physical meaning. See Fig. 2). The cross-section in these new variables will give us the density of events (for unit integrated luminosity) in the space (W, Q^2, Ω^*_K). This density can be calculated from the corresponding one in the space $(E'_e, \cos\theta_e, \Omega^*_K)$ by relating the two differential elements of volume via the Jacobian of the transformation.

$$\frac{\partial(E', \cos\theta_e)}{\partial(Q^2, W)} = \begin{vmatrix} \frac{\partial E'}{\partial Q^2} & \frac{\partial E'}{\partial W} \\ \frac{\partial(\cos\theta_e)}{\partial Q^2} & \frac{\partial(\cos\theta_e)}{\partial W} \end{vmatrix} = \frac{W}{2EE'm_p} \tag{1.4}$$

This allows us to write:

$$\frac{d^4\sigma}{dW dQ^2 d\Omega_K^*} = 2\pi \frac{W}{2EE' m_p} \frac{d^5\sigma}{dE' d\Omega_{e'} d\Omega_K^*} \tag{1.5}$$

We will prove (see appendix A) that, at first order in perturbation theory, kaon electroproduction can be seen as caused by "radiated" virtual photons the flux of which is determined by the electron variables. The cross-section will take the form:

$$\frac{d^5\sigma}{dE' d\Omega_{e'} d\Omega_K^*} = \Gamma \frac{d^2\sigma}{d\Omega_K^*} \tag{1.6}$$

where Γ will be interpreted as the flux of virtual photons per electron scattered into dE' and $d\Omega_{e'}$. We will absorb the Jacobian factor into the virtual photon flux when (W, Q^2) variables are used.

The remaining term is called in the literature virtual photon cross-section. Its structure is strongly constrained by the known electromagnetic interaction. Appendix A will show that it decomposes into four contributions from various combinations of virtual photon polarizations as

$$\frac{d\sigma}{d\Omega_K^*} = \frac{d\sigma_T}{d\Omega_K^*} + \epsilon \frac{d\sigma_L}{d\Omega_K^*} + \epsilon \frac{d\sigma_{TT}}{d\Omega_K^*} \cos 2\phi + \sqrt{2\epsilon(1+\epsilon)} \frac{d\sigma_{LT}}{d\Omega_K^*} \cos\phi \tag{1.7}$$

where

$$\epsilon = \left(1 + \frac{2|\vec{q}|^2}{Q^2} \tan^2 \frac{\theta_e}{2}\right)^{-1} \tag{1.8}$$

is a parameter measuring the degree of transverse linear polarization of the virtual photon.

1.4 THEORETICAL MODELS

Electroproduction processes have been proved to be a valuable tool for investigating the hadronic spectrum and the electromagnetic structure of the nucleon [7]. Although it is believed that the Standard Model (SM) [8, 9] provides the right theoretical framework for their complete description, the non perturbative nature of QCD at low energies precludes a direct comparison of experiments and theory. This is due to a unique feature of the strong coupling constant which does not decrease but increases when the interacting particles move further apart [10]. This frustrating situation has been partially alleviated with the use of Lattice QCD but there is still a long way to go before actual cross-sections can be computed numerically [11].

For those processes in which the quark masses can be neglected and the external momenta are small, the effective field theory constructed with a Lagrangian consistent with the (approximate) chiral symmetry of QCD, called Chiral perturbation theory (ChPT), provides a valid computational scheme [12]. Chiral lagrangians result very successful for pion electroproduction but due the relatively large strange quark mass serious difficulties appear in the calculation of processes involving kaons. ChPT kaon production calculations have been performed only up to 100 MeV over threshold. The results are encouraging as the comparison with the existing data is reasonably good but still insufficient for a theoretical description of KAOS measurements where energies over threshold of 150 MeV have been used [13].

A successful description of photoproduction has been obtained with hadronic field theories. This approach is based on effective degrees of freedom, mesons and baryons treated as a single entities, characterized by properties such as mass, charge, spin, form factors, and coupling constants (e.g. [14, 15, 16]). As we have seen, electroproduction processes can be formally reduced to the binary process of photoproduction by a virtual photon.

The different s, t and u diagrams for the lowest-order $p(\gamma^*;K)Y$ amplitude can be classified in non-resonant and resonant types, and are shown in Figs. 3 and 4 respectively. The names of the different channels correspond to the relevant Mandelstam variable describing the momentum exchanged in a particular diagram. Only hyperon resonances can be exchanged in the u-channel due to the conservation of strangeness. Finite decay widths are taken into account by modifying the propagator denominators in the s channel with the substitution: $s - m_R^2 \to s - m_R^2 + im_r\Gamma_R$ where m_R is the mass of the interchanged particle in the diagram and Γ_R its width. Also visible in Fig. 4 is a high precision measurement by the CLAS collaboration for the total photoproduction cross-section as a function of the CM energy. A clear resonance structure sitting on a continuous background near threshold can be observed. This general structure is nicely explained by the isobaric model as only the propagators in the s-channel terms involving an excited state can reach their poles. The t- and u-channel diagrams and the ground state nucleon s-channel term can not reach their poles because of energy-momentum conservation and can be seen as background contributions.

There is some ambiguity with respect to the structure of the KYN vertex in the sense that pseudo-scalar or pseudo-vector coupling for the interaction Lagrangians are possible. This issue has been studied by several authors but neither of the two possibilities has yet been confirmed as correct [17].

This approximation, where unitarity is lost, gives rise to the so called isobaric models (originally introduced by [18]). Coupled-channels (or rescattering) effects can be analyzed in the more general framework

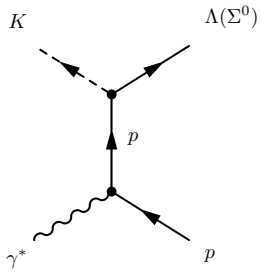

(a) s-channel born term

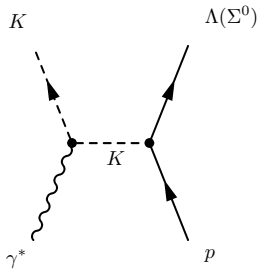

(b) t-channel born term

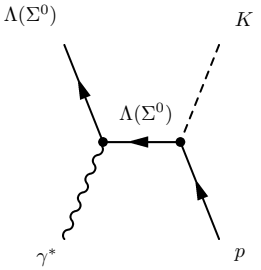

(c) u-channel born term

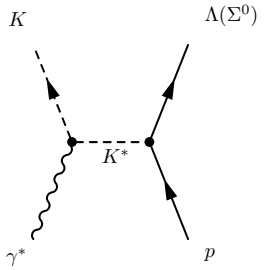

(d) t-channel extended born term

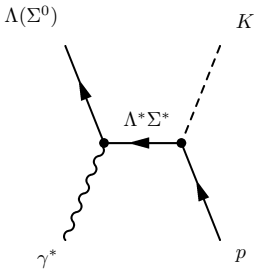

(e) u-channel extended born term

Figure 3: Non resonant contributions. The diagrams for the s,t and u channels can be divided in born and extended born terms depending on whether or not a resonance is interchanged.

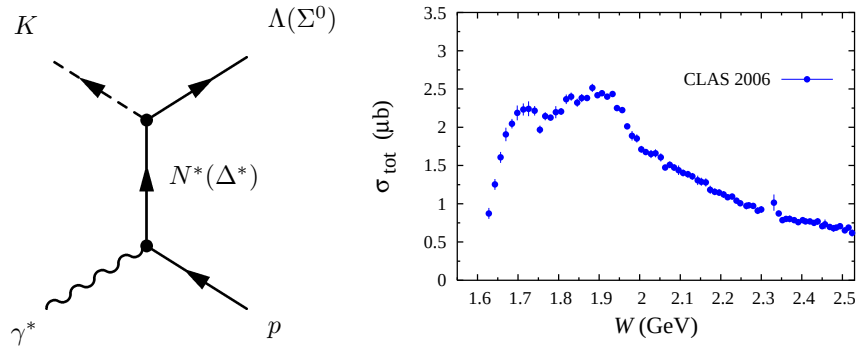

(a) Resonant s-channel Feynman diagram where excited nucleon and delta states are interchanged. Finite decay widths are taken into account by modifying the propagator denominators in the s channel with the substitution: $s - m_R^2 \rightarrow s - m_R^2 + im_r\Gamma_R$ where m_R is the mass of the interchanged particle in the diagram and Γ_R its width.

(b) Total KY photoproduction cross section as a function of the center of mass energy. On top of continuous background generated by the diagrams if Fig. 3 a clear resonant structure is observed. This feature can be explained by the s channel diagram shown on the left as only s-channel terms involving an excited state can reach their poles

Figure 4: Resonant contributions

of K-matrix formalism [19]. Although it has been proved that their contribution can be important [20], the large number of parameters involved generates a serious complication.

Including unitarity properly also implies serious difficulties with crossing symmetry, which is straightforwardly imposed at the tree level [21]. It is clear, however, that many issues concerning the basic reaction mechanisms can be clarified at the level of isobaric models. On the other hand, the unknown coupling parameters in the selected Feynman diagrams include to some extend final-state interactions as they have to be fitted to the data. The price to pay is that these coupling constants lose some of their physical meaning and cannot easily be compared to couplings from other reactions.

Several choices are possible concerning the set of resonances (compared to that of pion photoproduction, which is dominated basically by one nucleonic resonance), the baryonic and mesonic form factors needed to handle the internal structure of the hadrons at the interaction vertexes and the way to restore gauge invariance after their inclusion. The resulting models have to be fitted to the existing data set in order to fix their phenomenological parameters. A comparison with quark model predictions can then be considered as a test of their validity. A particularly interesting possibility is the search for resonances predicted by those models but not yet observed in pion nucleon reactions (see Section 1.3). A word of caution is necessary here. Although quite a lot of physical insight can be obtained by

means of the isobaric models, it is not clear whether or not the fine description needed to conclude categorically the existence of some missing resonance can be achieved with them.

In the following sections, a more detailed explanation of the two most successful isobaric models will be given. It will be shown that these two models disagree by more than 30 percent at very forward center of mass kaon angles were the cross-section is larger.

1.5 KAON-MAID AND SACLAY-LYON ISOBARIC MODELS

There are six isospin channels of elementary kaon photoproduction,

1. $p(\gamma K^+)\Lambda$
2. $p(\gamma K^+)\Sigma^0$
3. $p(\gamma K^0)\Sigma^+$
4. $n(\gamma K^0)\Lambda$
5. $n(\gamma K^0)\Sigma^0$
6. $n(\gamma K^+)\Sigma^-$

Most of the existing models try to describe simultaneously all hyperon channels. It is clear that this approach is adequate, as they are interrelated with each process involving diagrams having different combinations of the same coupling constants [3].

Kaon photoproduction has a relatively large threshold. The reaction is fully located in the so called third resonance region. A large number of resonances are potential candidates to participate in it, according to the known PDG states and quark models. Typically only those with reasonable branching ratios to the K+ (Λ,Σ) channels are taken into account [22] but still a set of 20 to 30 resonances has to be considered.

Further constrains can be obtained by imposing limits in the coupling constants for the KNΛ and KNΣ vertexes derived from an assumed weakly broken SU(3) symmetry. It can be shown [23] that a violation of 20 percent gives rise to the following allowed intervals: $-4.4 < \frac{g_{KN\Lambda}}{\sqrt{4\pi}} < -3$ and $0.8 < \frac{g_{KN\Sigma}}{\sqrt{4\pi}} < 1.3$. Crossing symmetry is used in addition by imposing the theoretical relation between the amplitudes for strangeness photoproduction $\gamma p \to K^+\Lambda$ and the radiative capture processes $K^-p \to \gamma\Lambda$.

It has been shown in high-energy hadron-hadron interactions that including all resonances in the t and s channels would amount to double counting [24, 25]. This duality is taken into account in some models, although it is not clear whether or not it strictly applies to low

3 Hadronic coupling constants can be related using isospin symmetry: $g_{K^+\Lambda p} = g_{K^0\Lambda n}$, $g_{K^+\Sigma^0 p} = -g_{K^0\Sigma^+ p} = g_{K^0\Sigma^+ p}/\sqrt{2} = g_{K^+\Sigma^- n}/\sqrt{2}$, $g_{K^+\Sigma^0\Delta^+} = g_{K^0\Sigma^0\Delta^0} = g_{K^0\Sigma^0\Delta^+} = -\sqrt{2}g_{K^0\Sigma_+\Delta^+} = \sqrt{2}g_{K^+\Sigma^-\Delta^0}$

energy kaon production. Some models have been constructed in which kaon resonances were excluded but it does not seem to be possible to describe the resonant structure observed near threshold without s-channel nucleonic resonances. It is usually assumed that only spin 1/2 nucleonic resonances are necessary for a proper description near threshold but larger spins may intervene in the reaction mechanism as energy increases. Models without those resonances have been able to fit high energy data as well, what might be an indication of an active role of duality with the kaon t resonances mimicking the higher s channel spin nucleonic ones [26, 27].

Propagators for spin>1/2 resonances are not unique. Some prescription has to be taken implying another source of troublesome variability [28].

Isobaric models with bare vertices show a divergence at higher energies, which clearly points to the need for introducing hadronic form factors. A correct description of vertex dressing effects must be done in terms of individual hadronic form factors for each kinematic channel. When phenomenological models are used instead, gauge invariance is lost. Current conservation is a must of the reaction dynamics and in order to restore it the simplest option is to add contact-type currents. Unfortunately, there is not unique method to define this contact term. Two popular prescriptions are due to Ohta and Haberzettl [29, 30].

Although the valence quarks of Λ and Σ are the same, both differ in their isospin values being $I(\Lambda) = 0$ $I(\Sigma) = 1$. When combined with $I(K^+) = 1/2$, isospin conservation in strong interactions forbids the participation of the Δ resonances in the s channel for Λ production. Once a set of resonances has been chosen, according to the principles explained above, an elementary operator is constructed based on a transition matrix element of the form:

$$M_{fi} = \overline{u}(p_Y) \sum_{j=1}^{6} A_j(s,t,k^2) M_j u(p_N)$$

Where s and t are the usual Mandelstam variables, and the gauge and Lorentz invariant matrices M_j are given for example in [31, 32].

$M_1 = \frac{1}{2}\gamma_5(\not{\epsilon}\not{k} - \not{k}\not{\epsilon})$
$M_2 = \gamma_5\left[(2q_k - k)\cdot\epsilon P\cdot k - (2q_k - k)\cdot kP\cdot\epsilon\right]$
$M_3 = \gamma_5(q_k\cdot k\not{\epsilon} - q_k\cdot\epsilon\not{k})$
$M_4 = i\epsilon_{\mu\nu\rho\sigma}\gamma^\mu q_K^\mu \epsilon^\rho k^\sigma$
$M_5 = \gamma_5(q_k\cdot\epsilon k^2 - q_k\cdot k k\cdot\epsilon)$
$M_6 = \gamma_5(k\cdot\epsilon\not{k} - k^2\not{\epsilon})$
with
$P = 1/2(p + p\prime)$ and $\epsilon^\mu = \epsilon^\mu_{photon}$ for photoproduction and $\epsilon^\mu = e\overline{u}_e(k_f)\gamma^\mu u_e(k_i)\frac{1}{k^2}$ for electroproduction.

Depending on the selection used, different sets of amplitudes A_j are obtained. Some studies have taken the path of including a large

amount of resonances at first and letting a fit to existing data to decide which of them were more active in the reaction dynamics. Obviously, the large number of fitting parameters generates doubts about the uniqueness of the solution obtained by this method.

Table 1: Model Kaon-Maid for Λ and Σ^0 production. Parameters of assumed resonances.

resonance	$(I)J^{\pi}$	mass(MeV)	width(MeV)	g1/v	g2/t
$K*(892)$	1^-	892	50	-0.787	-2.628
K1(1270)	1^+	1273	90	3.810	-2.408
N(1650) S_{11}	$\frac{1}{2}(\frac{1}{2}^-)$	1655	150	-0.133	0.000
N(1710) P_{11}	$\frac{1}{2}(\frac{1}{2}^-)$	1710	100	-0.258	0.000
N(1720) P_{13}	$\frac{1}{2}(\frac{3}{2}^+)$	1720	150	-0.046	-0.614
N(1895) D_{13}	$\frac{1}{2}(\frac{3}{2}^-)$	1895	370	1.101	0.634
Δ(1900) S_{31}	$\frac{3}{2}(\frac{1}{2}^-)$	1900	200	0.106	0.000
Δ(1910) P_{31}	$\frac{3}{2}(\frac{1}{2}^-)$	1910	250	0.322	0.000

The isobaric model by Bennhold et al. (Kaon-Maid in the following [33]) uses spin 1/2 and 3/2 s-channel resonances, S11(1650), P11(1710), P13(1720) and the missing resonance D13(1895) predicted by the constituent quark model by Capstick and Roberts and calculated to have a significant $K\Lambda$ decay width. For $K^+\Sigma^0$ production, the two Δ-resonances $S_{13}(1900)$ and $P_{13}(1910)$ are added. Phenomenological form factors are used at the hadron vertexes to account for the high W region behavior and the Haberzettl method is used to restore gauge invariance. Kaon resonances $K^*(890)$ and $K_1(1270)$ are included in the t channel. No hyperon resonances are used in this model. Coupling constants are obliged to fulfill the SU(3) constrains explained above. The Kaon-Maid version used in this thesis was fitted to the older SAPHIR data [34]

In the original Kaon-Maid model the longitudinal coupling constants to N^* resonances appeared unreasonably large (see table 1), and cut-off parameters unreasonably small. In addition, some inconsistencies in convention for the amplitudes in the electromagnetic form factors in the born terms and in the couplings to spin-3/2 resonances were found and corrected. A reduced version of the model was defined by setting these longitudinal couplings to zero.

As an example Fig. 5 shows the contributions of the different resonances in this reduced version to the total Λ and Σ^0 cross-sections in our kinematics (See chapter 2). We will also make use of a new version of Kaon-Maid that uses very small longitudinal couplings. In this version four nucleon resonances, $D_{15}(1675)$, $D_{13}(1700)$, $F_{15}(2000)$, and $D_{15}(2200)$ were added to the previous set and the free parameters of the model were re-fitted to describe the new world data on the

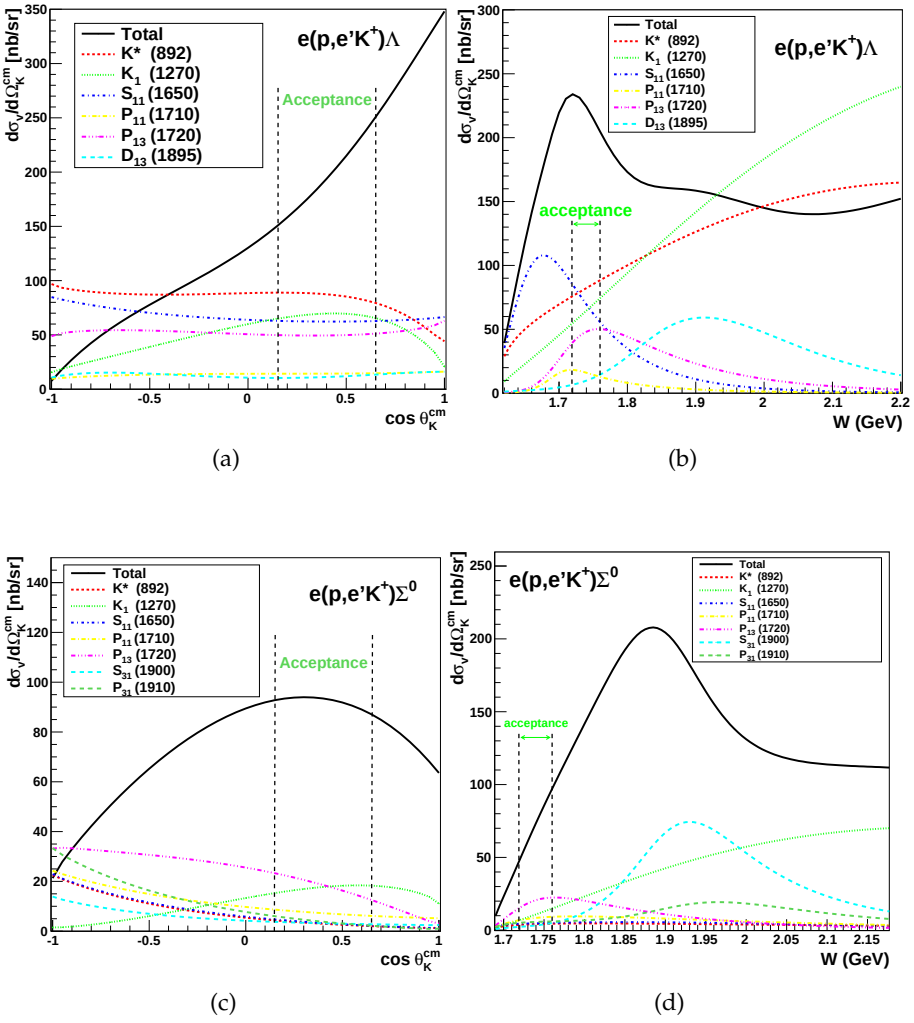

Figure 5: Contributions of the different resonances to the total cross-section as a function of kaon angle and total energy in the center of mass system in Λ and Σ^0 production for Kaos kinematics (W = 1.750 GeV, Q^2 = 0.036, GeV^2, ϵ = 0.4) as predicted by the reduced Kaon-Maid model. The resonant structure in the N* channels is clearly visible in plots (b) and (d).

photo and electroproduction. This will be the extended variant in what follows.

Table 2: Model Saclay-Lyon for Λ and Σ^0production. Parameters of assumed resonances.

resonance	$(I)J^\pi$	mass (MeV)	width (MeV)	g1/v	g2/t
$K*(892)$	1^-	892	50	-0.055	0.162
K1(1270)	1^+	1273	90	-0.194	-0.346
N(1440) P_{11}	$\frac{1}{2}(\frac{1}{2}^+)$	1440	350	-0.015	0.000
N(1720) P_{13}	$\frac{1}{2}(\frac{3}{2}^+)$	1720	150	-0.040	-0.141
N(1675) D_{15}	$\frac{1}{2}(\frac{5}{2}^-)$	1680	150	-0.630	-0.047
Λ(1405) S_{01}	$0(\frac{1}{2}^-)$	1407	50	-0.416	0.000
Λ(1670) S_{01}	$0(\frac{1}{2}^-)$	1670	35	1.754	0.000
Λ(1810) P_{01}	$0(\frac{1}{2}^+)$	1810	150	-1.955	0.000
Σ(1660) P_{11}	$1(\frac{1}{2}^+)$	1660	100	-7.331	0.000
Δ(1910) P_{31}	$\frac{3}{2}(\frac{1}{2}^+)$	1910	250	0.649	0.000
Δ(1232) P_{33}	$\frac{3}{2}(\frac{3}{2}^+)$	1235	131	-0.466	-1.876
Δ(1920) P_{33}	$\frac{3}{2}(\frac{3}{2}^+)$	1920	200	0.048	0.290

The version of the Saclay Lyon model [26, 35] (see table 2) used in this thesis (SL-A) shares with Kaon-Maid the same kaon resonances and the SU(3) constrains on the main coupling constants. The set of resonances goes up to spin 5/3 and only coincides with Kaon-Maid in the N(1720) for Λ production and in the $P_{13}(1910)$ Δ resonance for Σ. Spin 1/2 hyperon resonances are used instead of hadronic form factors for counterbalancing the strength of the Born terms through a destructive interference with these u-channel resonances.

S-LA and Kaon-Maid are good representatives of two main groups of these isobaric models which differ in the assumption of the hadronic form factors. Altought hadronic form factors are suposed to be important for the proper description of the process at large photon lab energies (since they suppress the cross section as a function of energy), this effect can also be accomplished in models without hadronic form factors. where the suppression is realized by inclusion of some hyperon resonances and nucleon resonances with higher spin (3/2 and 5/2). However, the method is not so convincing since the use of hadronic form factors is more flexible and simultaneously takes into account the fact that nucleons are composite objects. Models in which hadronic form factors. are not assumed and which include only one hyperon resonance overpredict the photo-production cross sections for photon energies larger than 2 GeV. Fig. 6 shows predicted cross-sections for KAOS kinematics ($Q^2 = 0.036$ $(GeV/c)^2$ and W = 1.67 GeV). It can be readily seen that in the region of very forward an-

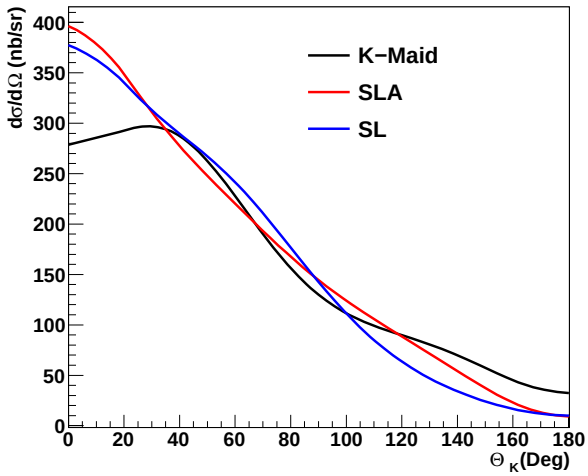

Figure 6: Model predictions at KAOS kinematics ($Q^2 = 0.036$ $(GeV/c)^2$ and W = 1.67 GeV) for full angular range. Similar results are obtained for S-L, S-LA and Kaon-Maid at large angles. Strong damping is observed for small kaon angles in Kaon-Maid.

gles these two types of isobaric models provide substantially different results for the cross section. The models with hadronic form factors reveal a damping of the cross section whereas the models without hadronic form factors continue rising.

Although no data are available for comparison, the strong damping predicted by models with hadronic form factors is believed to be far from realistic [36]. This issue is one of main open problems in Kaon electroproduction [37]. Apart from the important discussion about the role of hadronic form factors in meson photoproduction a full understanding and modeling of kaon electroproduction is an essential ingredient for hypernuclear physics.

Calculations of the cross section for production of hypernuclei depend on two main ingredients: the elementary-production operator and the nuclear and hypernuclear structure information. Understanding hypernuclear structure consequently relays heavily on getting the uncertainty regarding the elementary process well under control. Since hypernuclear studies are an important part of KAOS physics program, this issue is of importance. As a first step towards this important kinematical region, this thesis is dedicated to the measurement of Kaon electroproduction cross-section at very low momentum transfer although at only moderate kaon center of mass angle.

Future experiments with KAOS spectrometer will address this crucial angular region where the cross section reaches its maximum value while different isobaric models widely disagree.

1.6 PREVIOUS EXPERIMENTS

Kaon electroproduction experiments started in the early 70s, when the scaling behavior of deep inelastic electron scattering was well documented but almost no data was available for exclusive channels. The experimental activity was concentrated in Cambridge Electron Accelerator (CEA), the Wilson Synchrotron Laboratory (Harvard-Cornell) and the Deutsches Elektronen-Synchrotron (DESY), being mainly focused on the differences in the production dynamics between Λ and Σ^0 [38, 39, 40, 41]. The experimental arrangements consisted on dual-arm spectrometers (as in the case of the measurement presented in this thesis. See chapter 2) with limited kinematic coverage across the center-of-momentum angles. Interestingly, these experiments were designed to collect data at very forward angles (note half-quadrupoles completed with mirror iron plates in Fig. 8). As we shall see in the next sections, this region is of crucial importance since theoretical models widely disagree there. Unfortunately, the data quality was in general poor and this issue remains as one of the most important open ploblems in the field [37]. Despite their limited angular coverage,

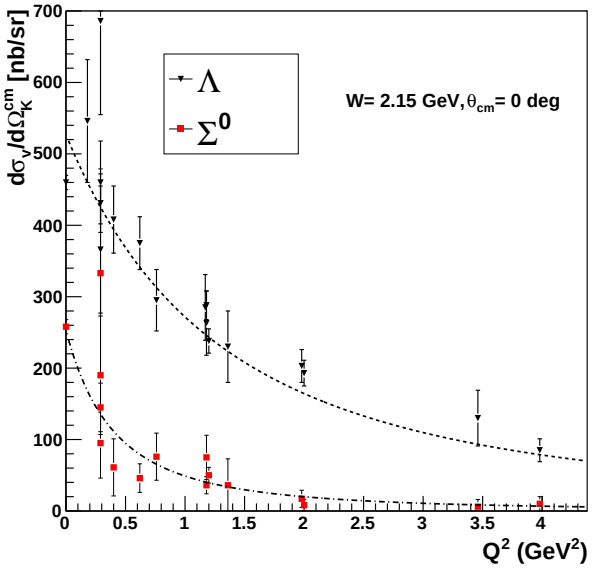

Figure 7: Q^2 dependence of the $K^+\Lambda$ and $K^+\Sigma^0$ electroproduction cross-section at center of mass energy W=2.15 GeV. Data is from Cambridge Electron Accelerator (CEA), the Wilson Synchrotron Laboratory (Harvard-Cornell) and the Deutsches Elektronen-Synchrotron (DESY), and has been scaled in the hadronic energy W to 2.16 GeV and in the polar kaon center of mass angle to zero when necessary. Dipole fits to the data are also shown by dashed lines.

clear differences between Λ and Σ^0 production mechanisms could be observed. Fig. 7 shows the collected data scaled to zero degrees in kaon polar angle and to W = 2.15 GeV as in [39, 42]. It can be seen that

Σ^0 cross-section falls much faster than Λ with Q^2. A rough Rosenbluth separation performed by Bebek et al. [39] allowed to conclude that only the transversal component of the cross-section (σ_T) contributed for Σ^0, but both transversal and longitudinal (σ_L) were relevant for Λ production.

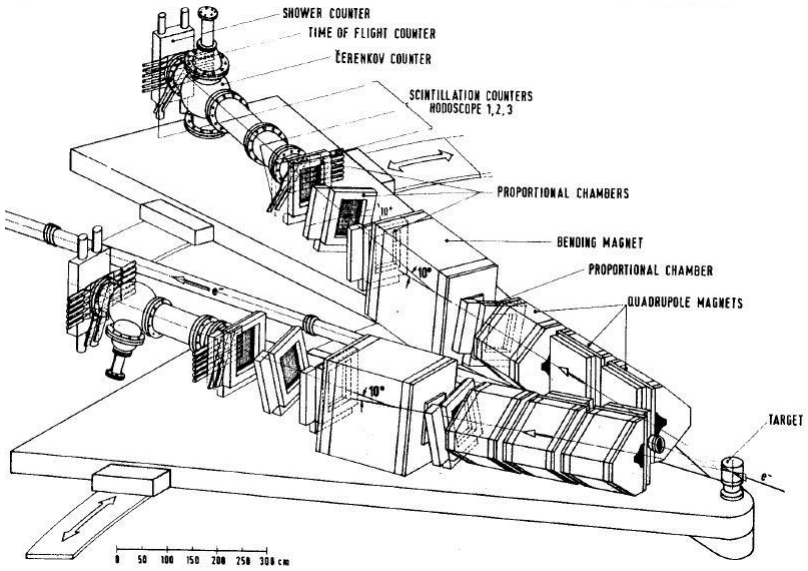

Figure 8: Spectrometer tandem at DESY showing standard arrangement of kaon electroproduction experiments during the 70s. The electron beam hits a 10 cm long hydrogen target. Similar spectrometers detect the scattered electron and produced kaon in coincidence. Trajectories through the dipole are reconstructed with the help of four multiwire proportional chambers for momentum determination and tracked back to the target for angular reconstruction. PID was based on time of flight and Cherenkov signals.

The new era of kaon electro and photo-production experiments started in the 90s. High duty electron accelerators allowed drastic reduction in statistical errors what allowed an identification of resonance structures especially in the Λ channel [43]. From 1993 up to 1998, SAPHIR collaboration in Bonn delivered several high quality data sets for kaon photoproduction with energies up to 2.6 GeV [44, 45, 46, 47, 48]. The data analyzed in [45] showed for the first time a resonance structure at $W \approx 1900$ MeV. It was claimed [49] that this structure could be explained by $D_{13}(1895\ \text{MeV})$, one of the missing resonances (see Fig. 9) predicted by quark models. LEPS at SPRING8 in Japan and GRAAL at the European Synchrotron Radiation Facility in France have also contributed to a rich set of photoproduction data in several isospin channels, including single and double polarization observables [50, 51, 52, 53]. The most ambitious experimental program covering both photo and eletro-production is being carried out at Jefferson Laboratory (Thomas Jefferson National Accelerator Facility) since 1996. Man power and experimental facilities are sufficient to

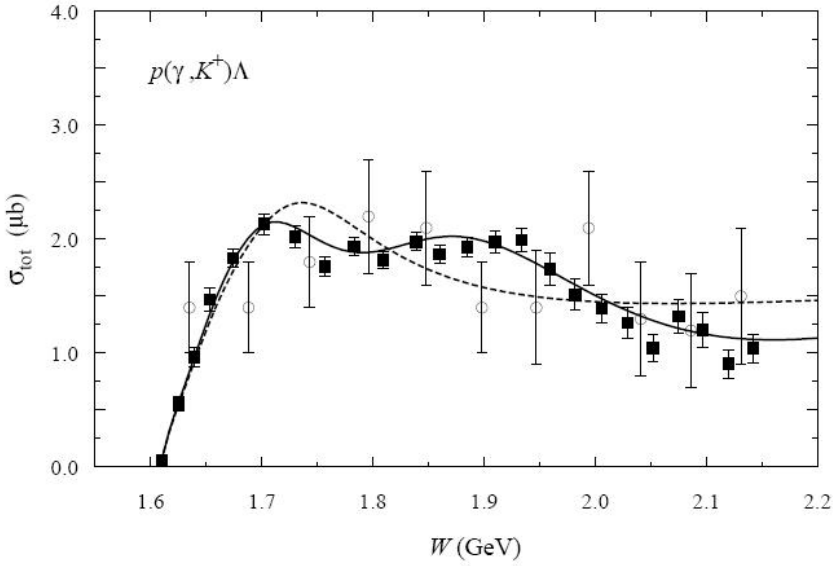

Figure 9: Total cross section for $K^+\Lambda$ photoproduction on the proton. Model predictions with and without the D13(1960) resonance are shown by solid and dashed lines respectively. SAPHIR data are denoted by the solid squares, old data are shown by open circles. Source [49]

achieve the final goal of measuring enough photoproduction observables to construct the complete set of four complex amplitudes that define the reaction completely in the next few years. Up to now, CLAS collaboration in experimental Hall B has published photoproduction cross sections with almost full angular coverage (with the important exception of very forward cm kaon angles) at energies up to 2.54 GeV [43]. This data disagreed with the previous SAPHIR results [48], specially in forward and backward regions. An independent analysis of a different CLAS data set obtained for pentaquark searches, but which also provided abundant data for the $K^+\Lambda$ channel, confirmed the previous results. There was also good agreement between CLAS and LEPS [51] measured cross-section at forward angles. A statistical study using four different isobar models [54] showed that SAPHIR data was coherently shifted down with respect to CLAS results. The controversy in this point seems to be settled in favor of CLAS data. Results from CLAS [55] confirmed the earlier measurements of GRAAL [52] and LEPS [50] for hyperon recoil polarization P and beam asymmetry Σ with improved precision and broader energy coverage. Results on beam-recoil observables for linear (Ox,Oz) and circularly polarized photons (Cx,Cz) were also presented in [55] and [56] respectively. This data indicated quite unexpectedly that Λ polarization had a strong tendency to be in the direction of the spin of the incoming photon. The effect of these new data in the isobaric models was a considerable simplification of the corresponding structure function, selecting a few

out of the many possible candidate resonances. Cx and Cz results indicated that the excitation of P13(1900) (instead of D_{13}(1895 MeV)) resonance was apparently necessary to fit the data [57].

The amount of data for electroproduction is substantially smaller. Hall C experiment E93-018 at Jlab performed the first precise Rosenbluth separation of cross-sections into longitudinal and transverse parts [42]. CLAS results for the transfer of longitudinal polarization of the virtual photon to the produced hyperon were also published in [58]. Latest results concern the first measurements of the longitudinal-transverse polarized structure function in electron scattering from an unpolarized target [59]. This data poses a new challenge to the models since strong interference effects have been observed. A1 collaboration has also recently measured this observable (before its completion as a double arm spectrometer) using one of the existing spectrometers for electron detection. This experiment continues the series of measurements at low Q^2 initiated in this thesis.

2 EXPERIMENTAL SETUP AND DATA ACQUISITION

Physicists like to think that all you have to do is say, these are the conditions, now what happens next?

— Richard Feynman

2.1 OVERVIEW

The experimental setup employed for the kaon electroproduction campaigns of 2008 and 2009 is presented in this chapter. Since this PhD thesis is the first one showing physical results of KAOS spectrometer, a detailed description of the apparatus and calibration work will be provided. The flexible tracking trigger system based on programmable FPGA chips is explained at the end of the chapter.

2.2 ELECTRON BEAM

The Mainz Institute for Nuclear Physics possesses a unique continuous wave electron accelerator in Europe. Its main scientific goal is the study of the hadronic structure by means of real and virtual photons produced by the electron beam. The Mainz Microtron (MAMI) produces electrons up to 1.5 GeV in four accelerating stages called MAMI A1, A2, B and C. The first three sections use race track microtrons (RTM). Electrons produced by a thermionic source are accelerated by normal conducting accelerating cavities powered by klystrons at 2.45 GHz, and circulated with the help of two symmetric dipole magnets in each stage, reaching a final energy of 855 MeV [60]. The fourth stage, MAMI C, was completed in 2007. The designing principle was modified to provide a more compact structure that fitted the available space, since just scaling the RTM to 1.5 GeV would have implied large modifications of the experimental facilities (the two bending magnets would have had a weight of approx. 4000 tons). A harmonic double sided microtron (HDSM) was considered an optimum solution. Acceleration is performed by two antipararell linacs and the circulation is performed by four 90° bending magnets instead of two at 180°. For longitudinal stability reasons, one of the two linacs is operated at double frequency than the other [61].

The accelerator can deliver unpolarized[1] electron beams with a maximum current of 100 μA. The beam root mean square (RMS) energy spread at 1.5 GeV is 110 keV.

Beam position is periodically controlled by removing the cryotarget and using a calibrated fluorescent screen monitored by a camera located in the scattering chamber. Beam rasterization is used to avoid local overheating of the liquid target. A typical centered and rastered beam is shown in Fig. 10:

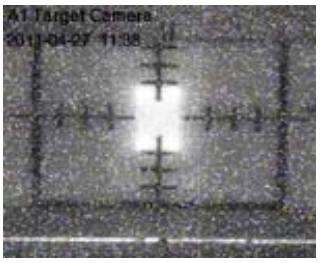

Figure 10: Example of centered and rastered beam profile observed in the calibrated screen

Current monitorization is continuously performed by means of a Foster probe. Two toroidal coils sense the magnetic field created by the electron beam. The induced current is a measurement of the beam intensity. This information is encoded in the data stream for the luminosity calculation.

The floor plan of the experimental and accelerator areas is shown in Fig.11. A beam transport system delivers the MAMI beam to four experimental halls: A1 (electron scattering), A2 (experiments with real photons), A4 (parity violating electron scattering) and X1 (experiments with x-rays).

MAMI C was conceived for a new generation of experiments in the realm of strangeness physics. The A1 collaboration operates three high precision spectrometers, but their large central track length precludes the efficient detection of the the sort lived strange mesons. KAOS spectrometer was added to the existing setup as an specialized apparatus for Kaon detection.

2.3 TARGET

Ideally, a pure proton target can be obtained by using liquefied hydrogen in thermodynamic equilibrium (orbiting electrons do not disrupt measurements at these energies). A series of technical difficulties have to be addressed in order to approach this ideal target. The power transfered by the beam is dissipated in the form of heat in the target volume. In order to avoid local boiling or density fluctuations, the

1 Highly polarized beams are also possible and have been recently used in kaon electroproduction experiments.

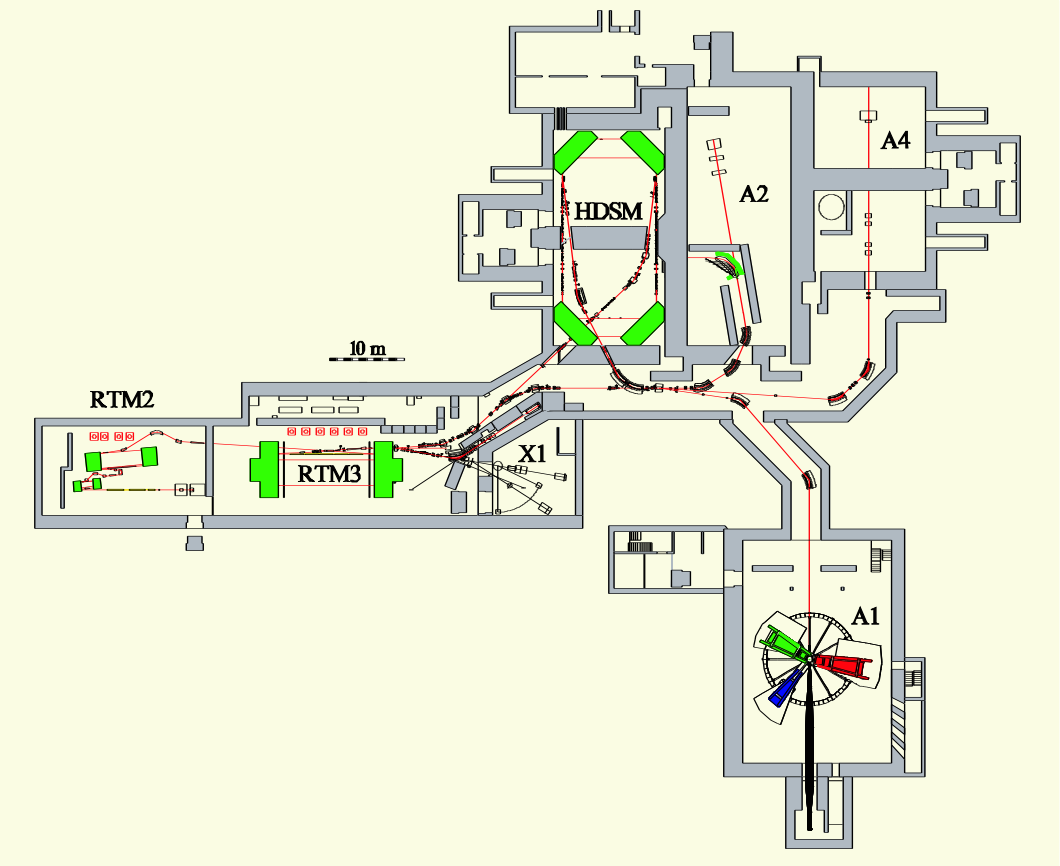

Figure 11: Schematic view of MAMI facilities showing accelerator stages based on three race track microtrons (RTM), one harmonic double sided microtron (HDSM) and experimental halls: A1 dedicated to electron scattering, A2 experiments with real photons, A4 parity violating electron scattering, X1 experiments with x-rays.

liquid has to be cooled and rapidly circulated. This requirement is essential for an stable luminosity, and consequently for a reliable cross section extraction. A Philips-Sterling machine with a cooling power of 75 W is routinely used for cooling the hydrogen target. The target is maintained at constant temperature and pressure by the following procedure: The Philips machine liquefies hydrogen, which is then transported to the target vessel by a transfer pipe. A second closed cooling loop containing the target hydrogen and continuously circulated by a dedicated fan interchanges heat with the external circuit. This heat is transported back to the compressor completing the thermodynamic cycle (See Fig. 12). The target cell 49.5 mm long with rounded end caps and made out of a 10 μm Havar walls is placed in the Basel-Loop. The geometry of the cell is optimized for enhancing the luminosity while keeping low the energy losses.

Because the MAMI electron beam has such a small transverse size at high currents, power density is sufficient to generate excessive local heating. In addition to the constant circulation of the target liquid hydrogen, beam rasterization is also used to avoid this problem. The electron beam is deflected transversely, and the corresponding displacement value is in an event by event basis recorded in the data stream for offline energy loss corrections.

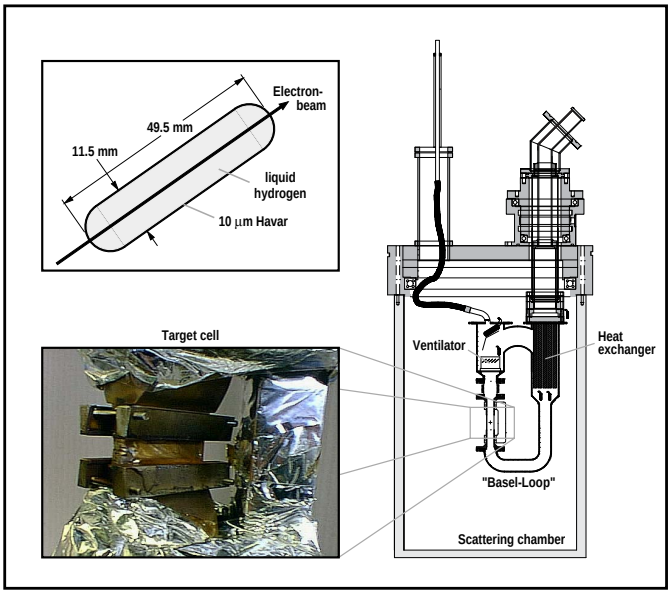

Figure 12: Cryo target used in the experiment. The target cell (top left) is mounted in a scattering chamber (right). Liquefied hydrogen is transported to the target vessel by a transfer pipe. A second closed cooling loop (Basel-Loop) containing the target hydrogen and continuously circulated by a dedicated fan interchanges heat with the external circuit. Stability of the liquid phase is essential for a precise determination of the luminosity. Temperature and pressure of the liquid are continuously measured. Figs. from [62].

2.4 KAOS SPECTROMETER

KAOS was originally designed as a compact spectrometer for meson detection in heavy ion collisions at the GSI facilities in Darmstat, and was successfully operated during the 1990s. Positively charged particles were focused vertically by a quadrupole magnet into the 20 cm gap of the following analyzing pole shoe dipole. During May and June 2003, KAOS magnets, together with associated electronics and detectors, were brought to Mainz. For its conversion into a double arm spectrometer dedicated to kaon electroproduction experiments, the quadrupole was removed as it could not provide focusing for both charge states. In addition, shortening the effective length of the magnetic system resulted in a reduced flight path and a higher survival probability [2]. During a first phase, and for the data analyzed in this thesis, one of the existing spectrometers (B) was used for electron detection. Positively charged particles at moderated angles were detected with KAOS spectrometer. Fig. 13 shows the experimental hall of the A1 collaboration. The three large vertically deflecting spectrometers A, B and C colored in red, blue and green respectively, can be freely rotated for measurements at different angles. KAOS (in purple), at measurement position, can be seen on the right hand side of the exit beam line (metallic cone), sitting on a red platform. Some angular freedom is given by a system of hydraulic positioning feet. The platform with the spectrometer can be moved from a parking position to a measurement position by means of a system of hydraulic pressure cylinders on skid-tracks. The detector package of the spectrometer consists of two multiwire proportional chambers for track determination, and two scintillator walls for timing and triggering purposes (see Fig. 14). In the next sections a complete description of KAOS magnet and detectors will be provided.

2.4.1 *Dipole magnet*

Although force and acceleration are not parallel vectors in general for relativistic particles as can be seen from:

$$\vec{F} = \frac{d\vec{p}}{dt} = \frac{d\left(\frac{m_0\vec{v}}{\sqrt{1-v^2/c^2}}\right)}{dt} = \frac{d\left(\frac{m_0}{\sqrt{1-v^2/c^2}}\right)}{dt}\vec{v} + \frac{m_0}{\sqrt{1-v^2/c^2}}\vec{a}$$

(where a term proportional to the velocity vector arises as a consequence of the relativistic definition of linear momentum), if only magnetic forces are responsible of the particle motion, the perpendicularity of force and velocity expressed by the Lorentz force $\vec{F} =$

2 Recently, small angle coincidence experiments have been performed with two dipole bending magnets bringing the electron beam into KAOS at zero degrees.

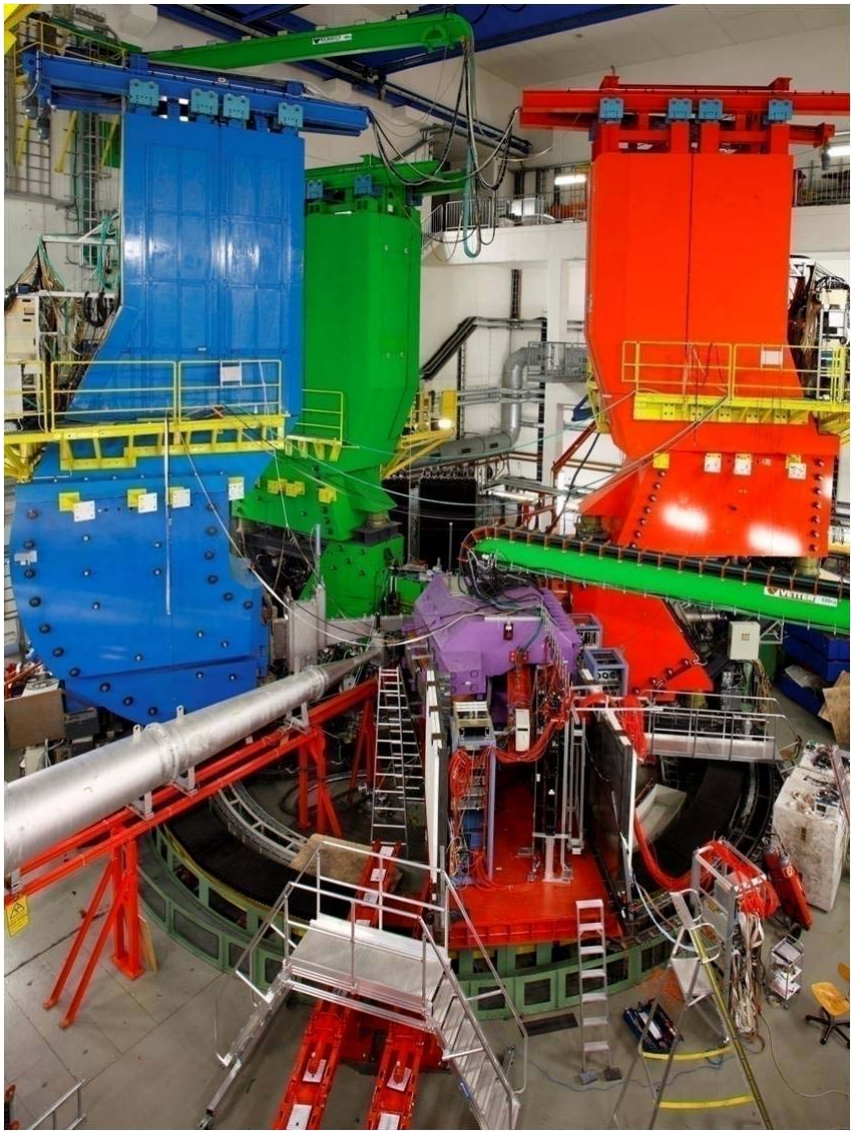

Figure 13: Experimental hall of the A1 collaboration. The three large vertical spectrometers (blue, green and red) have been complemented with KAOS (purple). KAOS can be moved from measurement position to parking position, sliding the red platform where it sits along the two rails visible in the picture. This allows the recovery of the full angular range of the vertical spectrometers.

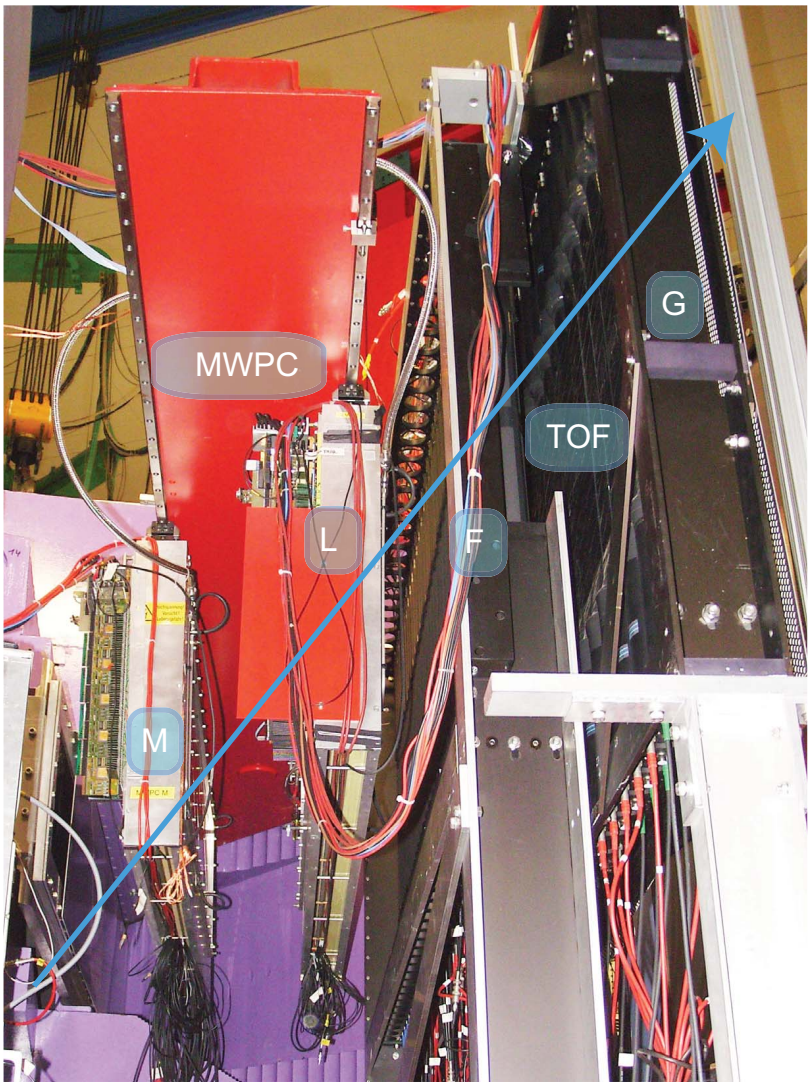

Figure 14: Detectors equipping KAOS spectrometer at the time of data taking. From left to right: MWPC(M), MWPC(L) and the two scintillator walls F (overlapping with the focal plane) and G used for tracking trigger.

$q\vec{v} \times \vec{B}$, combined with the relativistic version of the vis viva theorem $\int_a^b \vec{F} \cdot d\vec{r} = \Delta(m(v)c^2)$, allows us to write:

$$\vec{F} = q\vec{v} \times \vec{B} = \frac{m_0}{\sqrt{1 - v^2/c^2}} \vec{a}$$

This equation is identical to the Newtonian one, with the replacement of the particle mass by the "relativistic mass" $m(v) = \frac{m_0}{\sqrt{1-v^2/c^2}}$. Flat trajectories are thus circles of radius $r = \frac{|\vec{p}|}{q|\vec{B}|}$. This relation allows a momentum determination based on the measurement of a geometrical quantity what defines the physical principle at work in magnetic spectrometers.

Dipole magnets generate an almost constant magnetic field. If the geometrical shape of the space region where the dipole field is present is properly designed, focusing of particles with equal momentum but different starting angles from a source point can be accomplished, at least in first approximation. KAOS dipole magnet was designed with the shape of a shoe to provide approximately equal flight time for the same particle species and still keeping good focusing characteristics thus allowing a particle identification (PID) by time of flight (TOF) and momentum determination simultaneously. The price to pay is a relatively curved focal surface that has to be properly parametrized [63]. For its use as a double spectrometer, the other side of the magnet, which is simply a straight line, at an angle of 71° with respect the entrance window will be used. As PID is not critical for the negative arm of the spectrometer, this is not an important issue.

The first-order focusing is achieved with a bending of the central trajectories by 45°. In close analogy with optical lenses, dipole magnets can be described in first approximation by a transportation matrix, the elements of which have a clear physical interpretation. An enlargement of the spot where particles are generated in the dispersive direction is measured by a magnification factor M_x. Chromatic aberration is put to good use, as it provides the necessary momentum separation. This crucial property of a magnetic spectrometer is called dispersion (D), and when combined with the effective spot size (due to magnification), provides a measurement of the first order resolving power of the spectrometer: $R1 = \frac{D}{M_x \sigma_0}$. This translates into a momentum resolution given by: $\frac{\Delta p}{p} = \sqrt{(\sigma_x^2 + M_x^2 \sigma_0^2)/D^2}$ where σ_x is the spatial resolution in the focal plane and σ_0 the beam spot size. Table 3 summarizes the main characteristics of KAOS and B spectrometers.

2.4.2 *Experimental determination of transfer matrix. Collimators*

In order to have a more precise control of the acceptance of the spectrometer and for calibration purposes, a set of collimators movable by a motor controlled system was installed in front of the entrance

Table 3: Spectrometers properties

Property	Spectrometer B	KAOS
maximum momentum	870 MeV	2100 MeV
momentum acceptance	15%	50%
solid angle acceptance	5.6 msr	10.4 msr
dispersive angle acceptance	4 deg	10.5 deg
non-dispersive angle acceptance	1.15 deg	0.8 deg
length of central trajectory	12.03 m	5.3 m
angle of focal plane	47 deg	45 deg
length of focal plane	1.8 m	1.2 m
dispersion at central trajectory	8.22 cm/%	2.4 cm/%
magnification at central trajectory	0.85	2.0
dispersion to magnification	9.64 cm/%	1.2 cm/%
1st order resolving power	19 000	2 400
1st order momentum resolution	$< 10^4$	10^3

window. A wide rectangular collimator was used during data taking to limit the acceptance of the spectrometer, in order to avoid the background produced by collisions with the inner faces of the dipole. As it was found later, an error in the collimator height resulted in effective collimation only for the horizontal angle. Vertical collimation was effectively achieved by the geometrical cut introduced by the detector package of the spectrometer.

An experimental evaluation of dipole transfer matrix[3] was accomplished by means of a sieve collimator made of 20 mm thick lead with 16 holes, 5 mm in diameter each at a distance of 1000 mm from the target. Elastically scattered electrons on carbon and tantalum targets were used for this purpose.

The energy of the detected electrons depends on the scattering angle θ'_e due to the recoil of the target of mass M as follows:

$$E_{e'} = \frac{E_e - E_X(1 + E_x/(2Mc^2))}{\eta}$$

being

$$\eta = 1 + 2E_e/Mc^2 \sin(\theta_{e'}/2)$$

and E_X the excitation energy of the target respectively. Heavy targets result in an small kinematic broadening providing an efficient source of almost monochromatic electrons. Energy corrections are calculated

3 A first order transfer matrix was calculated by means of a dedicated Geant simulation in [63].

via a Taylor expansion in the angular variable, and used to evaluate the accuracy of the momentum reconstruction. Fig. 15 shows the reconstructed polar and azimuthal target angles. The remaining uncorrected optical aberrations can be observed from the deviations to the nominal hole coordinates in the figure.

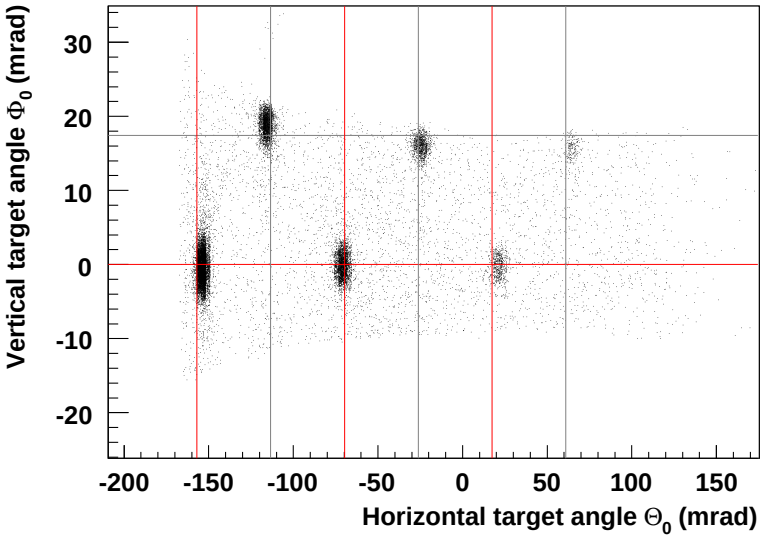

Figure 15: Elastically scattered electrons of 450MeV energy, back-traced from the detector system of the Kaos spectrometer to the target.

2.4.3 *Dipole field characterization and read out*

During the experiment, field monitorization was performed by means of a Hall probe situated within a short aluminum tube, located in one of the vacuum flanges of the dipole. Since the available field maps were referred to a magnetic field value given at the center of the magnet, a calibration of the Hall probe was necessary. Precise central field values were measured with a set of variable precision NMR probes. The corresponding magnetic field at the Hall sensor position was recorded as well, giving rise to a calibration curve. The calibration parameters were used for the determination of the field value used in the spectrometer simulation (see chapter 3). Hall probe reading showed a high stability of the dipole magnet during the kaon electroproduction campaigns of 2008 and 2009.

2.4.4 *Multiwire proportional chambers*

In order to reconstruct the trajectories of the particles, two large area multi-wire proportional chambers (MWPC), situated behind the vacuum chamber were put into service. Both MWPW (called M and L) have a sensitive area of 35×120 cm^2. Their position resolution is 0.5 mm (FWHM). Particle trajectories outside the dipole magnet are

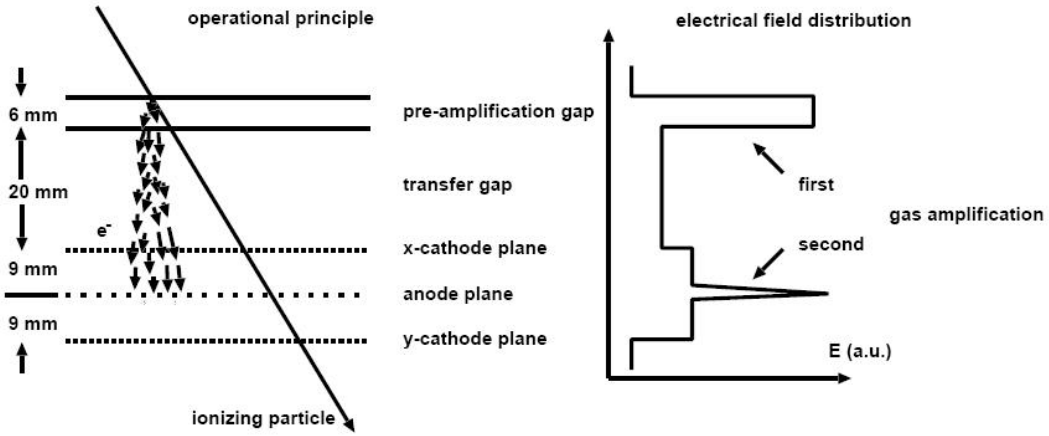

Figure 16: Electrodes and electric field configuration of MWPC

straight lines determined by the two points (x_M, y_M) and (x_L, y_L) provided by the chambers. The momentum of a particle is obtained by calculating the intersection of the measured trajectory with the focal plane. A distinctive characteristic of these chambers is that they a have a first preamplifying stage (see Fig. 16 for an schematic view of field and electrodes structure). Charge amplification is achieved there, allowing smaller voltages to be used between anode and cathode planes and still achieving efficient particle detection (by this method, heavily ionizing particles profusely produced in ion collisions at the GSI did not generate sparks, improving the overall behavior of the chambers and reducing the mechanical tension suffered by the long wires thus minimizing their deformation). Five cathode wires are read out by a common preamplifier, and the deposited charge is integrated by ADCs mounted in the chambers frame. Read out electronics is based on transputer chips. Since the MWPC documentation provided by the GSI was not detailed enough, some inverse engineering had to be performed in the laboratory for detectors, in order to gain the necessary knowledge about their electronics (see [64] for a detailed description of MWPCs electronics an read out system employed for their use in KAOS spectrometer.).

The gas mixture used at the GSI contained heptane as a quenching gas. For safety reasons, a decision was taken of using isobutan for their operation in Mainz.

Just at the beginning of this thesis, efficiency studies performed with ^{90}Sr with an small chamber of the same type, used originally between quadrupole and dipole magnet, showed that minimum ionizing particles could be detected at efficiencies of the order of 98%. Extensive studies for optimum HV values and appropriate gas mixtures were also carried out (see Fig.17). These results, in addition to the experience achieved during beam time operation, lead to the following optimum values for the gas mixture and voltages: Ar: 84%, CO_2: 9%

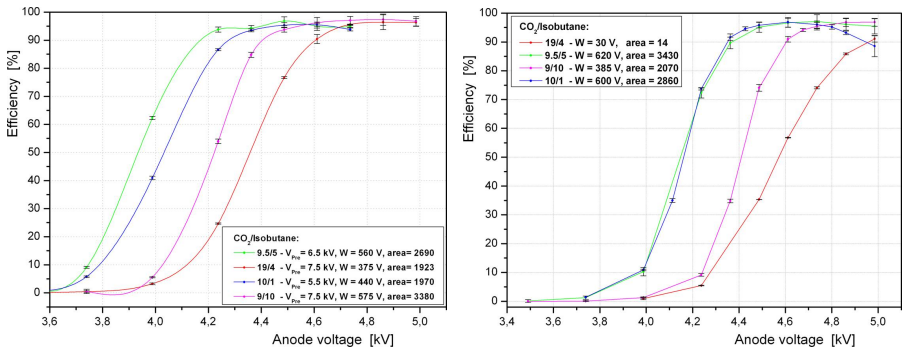

(a) (b)

Figure 17: Measured efficiency for a set of different gas mixtures and pregap voltages as a function of the anode voltage. A saturation region or plateau is observed in all cases and a clear dependency of the plateau starting point on the other operating parameters can be seen. The effect of the pregap is shown in subfigure (b) where the pregap voltage is set to zero. Larger anode voltages are needed to achieve the same detection efficiency.

and isobutan (C4H10): 7% at an anode voltage of 4.8 kV, and a pre-gap voltage of 7.5 kV. For their final installation in KAOS platform, the gas tubing system was renewed, optimizing gas flow and ensuring mixture uniformity within the chamber volume.

2.4.5 *Scintillator walls*

Two scintillator walls, labeled F and G, are used as timing and trigger detectors in the positive arm KAOS detector package. The F detector, located approximately in the focal plane of the spectrometer, consists of 30 plastic scintillators paddles (38 cm x 3.7 cm x 2 cm) of type Pilot F (modern equivalent: BC408) and 8 cm long lucite light guides. The paddles are tilted by 37° around the longitudinal axis in order to achieve an almost perpendicular flight path of the incoming particles into the 3.7 cm face. The total length covered by the wall is 1.89 m. The scintillators are read out in both ends by 2 in. Hamamatsu R1828 phototubes to allow for light propagation compensation.A momentum resolution of about 4% is obtained with these 3.7 cm wide paddles.

The G detector was added to the system permitting the implementation a rough angular selection trigger. It also consists of 30 scintillator paddles (47 cm x 7.5 cm x 2 cm), with a purely flat geometry spanning a length of 2.2 m and read out by the same type of phototubes. Plastic scintillator material is BC408. This fast scintillators (2.1 ns decay constant) are very suitable for time of flight measurements and still feature a large absorption length of 380 cm.

2.4.5.1 *Read out electronics*

Scintillator paddles are grouped in sets of eight channels (see Fig. 18). Analog signals from top and bottom photomultipliers are directed to a sum and splitter card (GSI SU 1601). 12% of the signal charge is delayed 250 ns until the trigger condition is generated and integrated by a LeCroy 1885F ADC, and 88% is sent to the constant fraction module CF8105. Eight inputs are handled simultaneously and fed after a logic delay module (GSI 1610:500 ns) as start signals into the LeCroy 1875 TDC by a flat cable. Both Lecroy modules are located in a FASTBUS crate.

The sum output is used as a top bottom coincidence first level trigger condition. The signal is discriminated and then sent to the main positive arm trigger, implemented in the FPGA based VUPROM logic module. [4]

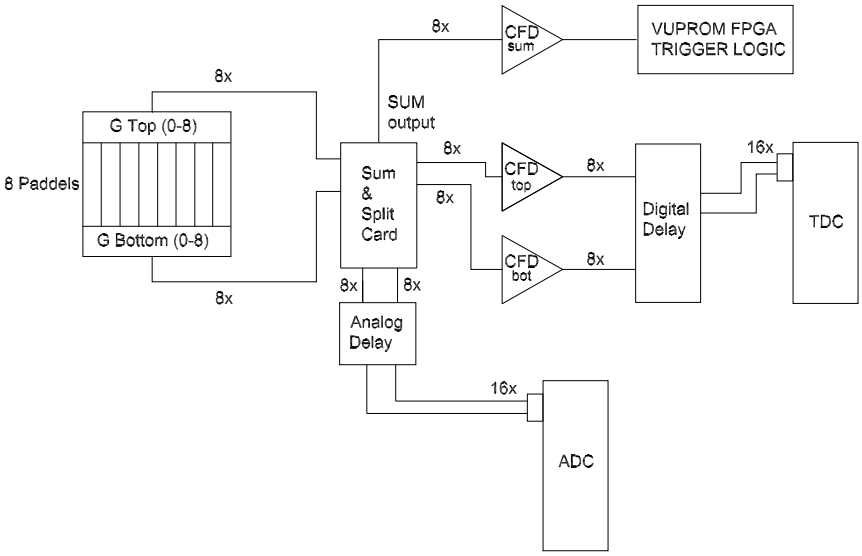

Figure 18: Scheme of scintillator walls electronics. See text for explanation.

2.4.5.2 *Calibration*

Both walls were in use for several years at the GSI. After the necessary refurbishment, a complete characterization was performed in order to decide whether or not their use for electroproduction experiments at Mainz was feasible. Time resolution and absorption length were measured for a sample paddle with a set of trigger detectors for cosmic muons, that allowed a reliable hit position determination

4 CFD, splitters and delays were used previously in the GSI setting. All modules were checked prior to their installation in KAOS electronic racks.

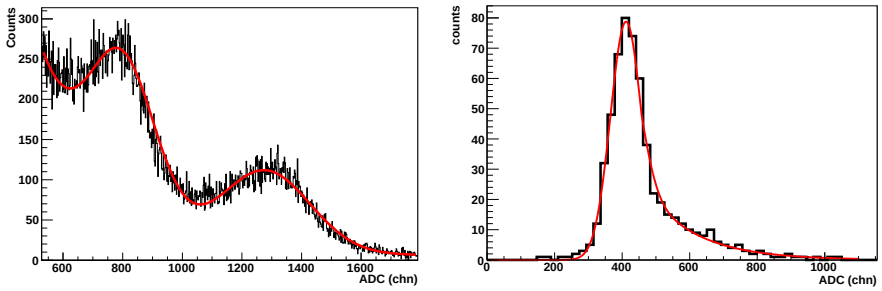

(a) (b)

Figure 19: (a) Calibration ADC spectrum of a sample paddle (G-21 top) excited at its centre with monoenergetic electrons from a $^{207}_{83}Bi$ radioactive source. Two peaks, corresponding to 0.481 MeV and the superposition of the 0.975 and 1.047 MeV lines, are clearly visible. 120 histograms for each of the seven HV values used in the calibration were fitted automatically by two Gaussians plus an exponential background. (b) Calibration ADC spectrum of F sample paddle excited with beam electrons going through KAOS working in reverse polarity. A single Gaussian with an exponential tail is fitted to the m.i.p energy histogram.

with an accuracy of 1 cm. The study showed a clear deterioration of the optical properties of the plastic material, resulting in absorption lengths almost one order of magnitude smaller than expected. Time resolution was also affected as it scales with the square root of the number of detected photons (the resulting value was FWHM=200 ps). This reduced resolution was still sufficient for the time of flight PID needed at KAOS. The decision was taken of maintaining the existing paddles for the first physical measurements of the spectrometer.

A first calibration of the walls was performed with a $^{207}_{83}Bi$ source. Fig. 19(a) shows the clear double peak structure obtained by exciting the paddles at their center with the internal conversion electrons of energies 0.481, 0.975 and 1.047 MeV. A dedicated hardware trigger, consisting of the oring of the 60 top and bottom signal coincidences, was arranged for this purpose. The source was displaced from scintillator to scintillator for each of the seven calibration voltages between 1800 V and 2400 V. The automatized analysis of these 840 histograms was performed by a dedicated software. A pedestal localization and elimination was followed by a peak finding algorithm, complemented with a fitting routine where a model based on the sum of two Gaussian peaks and an exponential background was assumed. The set of seven ADC values obtained for each PMT was assumed to follow a relation of the type: $chn = aV^b$. A linear fit in a log-log plot was used to extract the calibration parameters a and b.

Unfortunately, the bad condition of many of the scintillator paddles did not allow a convergence of the peak finding algorithm for all

channels. This calibration was thus considered provisional and used for testing purposes in the first KAOS runs. Final calibration was performed during beam time working KAOS dipole in reverse polarity and detecting the minimum ionizing electrons. A cut in the MWPCs measured position allowed a selection of electrons going through a narrow band in the center of the paddles, providing a clear energy signal (see Fig. 19 (b)).

2.4.5.3 *Absorption*

Absorption coefficients for F and G paddles were obtained by fitting an exponential function $Q(y) = Ce^{-y/L}$ to the -corrected for path length- ADC histograms. Values of the order of 1 m were found for G wall. F paddles showed a much poorer performance being the average absorption length 25 cm. For data analysis, the most convenient method to correct light absorption was proved to be the use of geometrical average of top and bottom charge values ($\sqrt{Q_{top}Q_{bottom}}$), as this quantity does not depend of the vertical coordinate due to the cancelation of the two exponentials.

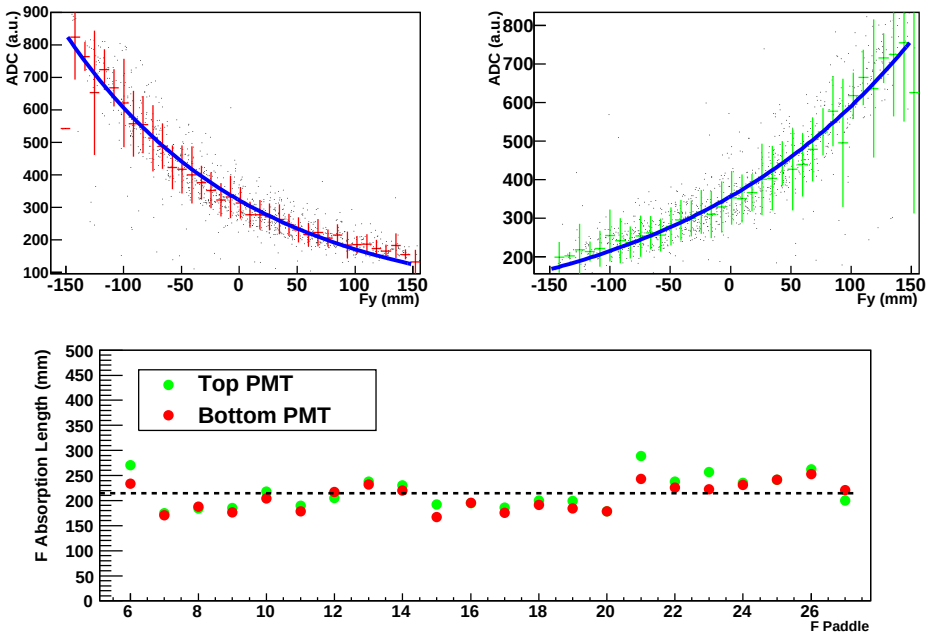

Figure 20: Top: Absorption fits for top and bottom PMTs for a representative F paddle. Bottom: Absorption lengths obtained from the fits to all F paddles. Dotted black line shows the low average value resulting for these aged paddles.

2.5 KAOS SINGLE ARM TRIGGER

Most of particle physics reactions of interest nowadays are rare and appear in highly noisy environments were reaction selectivity becomes a crucial issue. Trigger systems with increasing levels of sophistication have been devised through the years in order to cope with these situations.

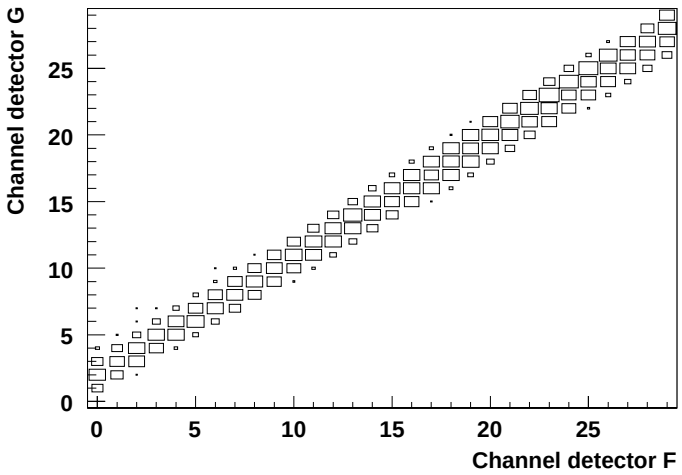

Figure 21: Histogram of paddle hits in both scintillator walls. The logic rejects any event off the diagonal band.

Field programmable gate arrays (FPGA) have been used extensively for this purpose. The main advantages of FPGA over conventional logic modules are their intrinsic flexibility and their highly compact form factor. High density connectors are employed to handle a large numbers of channels with a single module reducing significantly electronics complexity.

In order to deal with the large background expected in KAOS spectrometer at the detectors location, a clever arrangement was devised in which the two available scintillator walls were used for triggering purposes in addition to their function for PID. A dedicated Geant simulation showed a clear hit pattern for valid events in the scintillator walls (see Fig. 23). Two universal logic experimental VME modules (VULOM), equipped with a VIRTEX 4 FPGA and ECL front panel inputs (up to 32), and outputs (up to 32) designed at the GSI electronics laboratory, were tested at first (their performance in a real experiment had not been checked before).

According to the simulation, all tracks included in the acceptance could be represented by formulas like: $T = [F1 \wedge (G3 \vee G4 \vee G5)] \vee [F2 \wedge (G4 \vee G5 \vee G6)]$, where $\wedge$ and $\vee$ are symbols for AND and OR logic functions respectively. VHDL code implementing this logical functions was used to program the modules. The compiled program could be loaded into the FPGA via a JTAG connector or directly by means of the VME interface. The program was stored in a dedicated

64MB flash memory and automatically loaded after powering up. Two VULOM units were necessary to cope with the 90 valid combinations, given by the track conditions. The input signals to the FPGA modules were generated by a constant fraction discriminator model CF8105. An amplitude threshold was applied to 88% of the sum of top and bottom PMTs signals rooted to this modules. Due to absorption in the plastic material, the sum signal had the following dependency with respect to the position along the scintillator: $V(y) = V_t(0)e^{\alpha y} + V_b(0)e^{-\alpha y}$. Assuming for simplicity that $V_t(0) = v_b(0)$, it can be easily shown that this function has a minimum at y=0. If a threshold voltage is chosen for the sum signal so that a minimum ionizing particle crossing perpendicularly the scintillator paddle at its center is accepted, then any other hitting point or angle will be accepted as well. If this threshold level is high enough, random coincidences due to dark counts top-bottom are largely reduced.

Random coincidence rate was measured for the maximum threshold value that allowed the pion energy loss band at central TOF hight to be fully observed in the ADC histograms. The resulting values per paddle were in the order of a few Hertz. The tracking trigger condition reduced this rate to zero for all practical purposes. In addition, a partial reduction of real neutral particle background was obtained already at this level, as the energy deposition of these particles was substantially lower than the one given by m.i.p. The new trigger system was tested during the first KAOS/A1 beam-time in Nov. 2007. Beam currents up to 10 μA of 855 MeV electrons on a carbon target (225 mg/cm^2) were used. Particle identification was carried out successfully, and despite the relatively small distance from the target area to the electronics, the logic modules did not show any misbehavior. Fig. 2 histograms the number of coincidences for each pair of F and G scintillator paddles. The diagonal band corresponds to the valid trajectories shown in Fig. 23. When the trigger requirement is removed by loading an OR condition of all paddles in the FPGAs, the off diagonal pairs in the plot are generously populated, a sign of the high electromagnetic background. Background suppression depends on the threshold imposed on the summing discriminators. At 500 nA and a sum signal threshold of 30 mV, the raw trigger rate changed from 49 kHz to 1 kHz, while at 310 mV the reduction was from 1.7 kHz to 1.4 Hz.

In a second stage the two Vulom modules were substituted by a new generation of devices, VUPROM, with 256 I/O channels. This VME module is equipped with a Virtex-4 FPGA chip, capable of operating at 400 MHz. This setup also allowed an easy reprogramming via VME bus and had a full flexibility concerning the combinations of paddles allowed for an arbitrary trigger as all channels were handled by the same module.

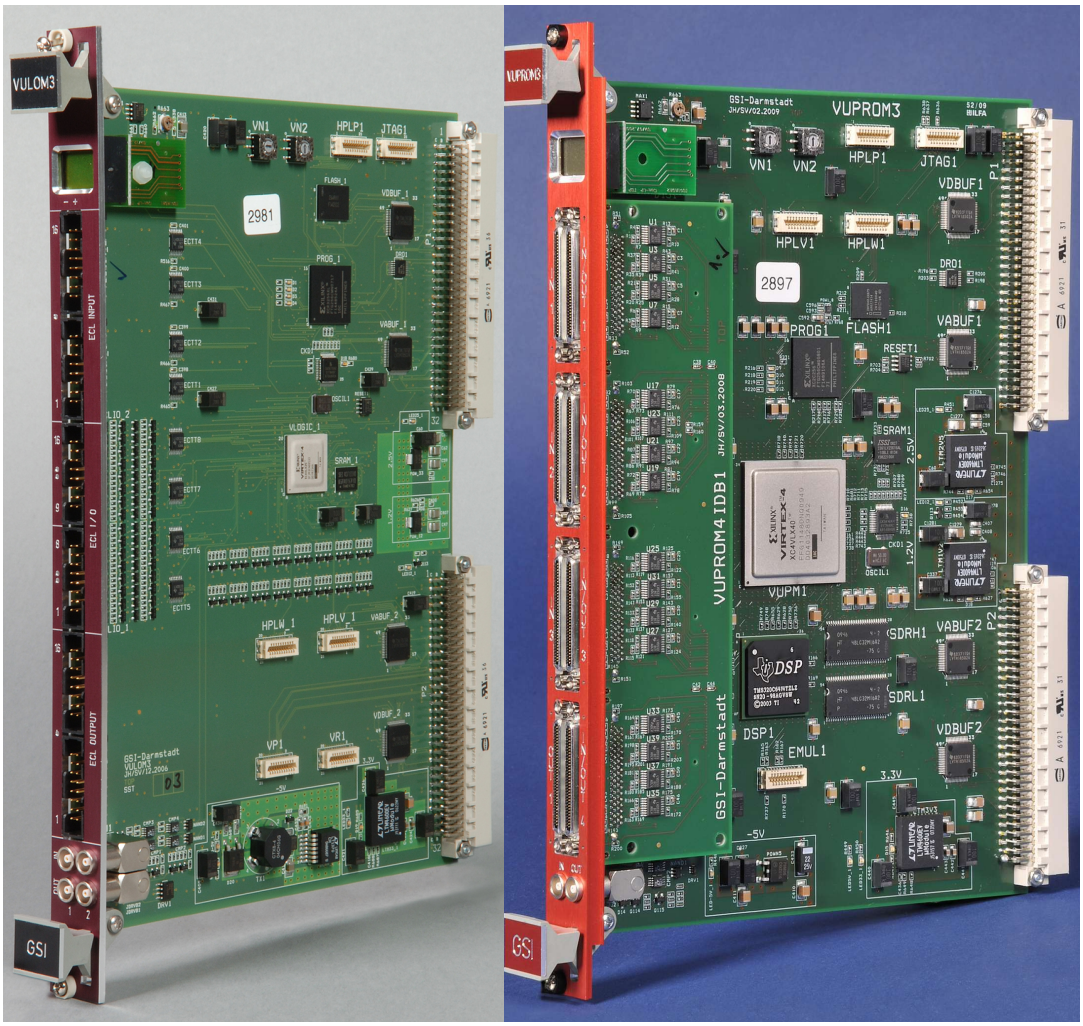

(a) (b)

Figure 22: Photographs of first (left) and second generation (right) FPGA logic modules: VULOM and VUPROM used in the tracking trigger for the positive-arm of the KAOS spectrometer. Both VME modules were equipped withs VIRTEX-4 FPGA chips and flash memory. Different trigger programs could be loaded into the FPGA via a JTAG connector or directly by means of the VME interface. VUPROM allowed a larger number of channels to be handled by the same module (256 I/O channels) by means of high density connectors.

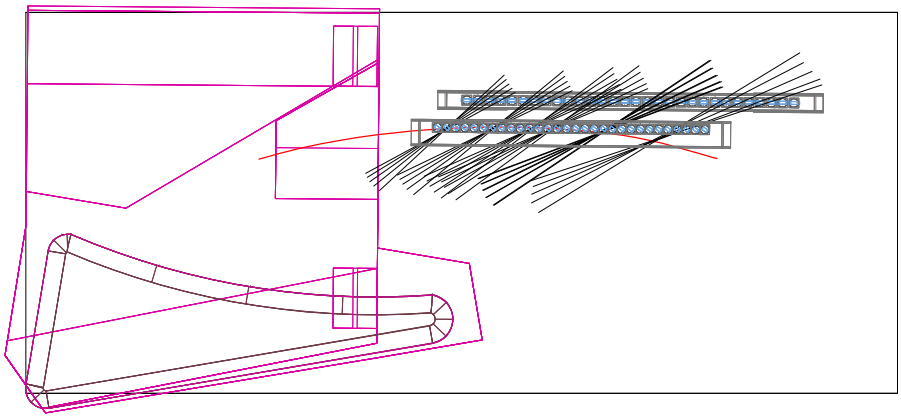

Figure 23: Scheme of the KAOS/A1 platform with pole shoes, magnet yokes, focal plane, and scintillator walls. Kaon trajectories crossing both walls are defining a pattern used for the logic implemented in the VULOM modules.

2.6 SPECTROMETER B

Spectrometer B optics is made by a unique dipole magnet (clam-shell) ,with point-to-point focusing in both planes (see Fig. 24). This construction permits to have a narrower spectrometer which can reach small scattering angles (down to 7°).

This spectrometer can also be tilted for reaching out of plane angles up to 10°. The central momentum is determined by setting the central magnetic field of the dipole. A rough determination of the field is made with hall probes in the first part of the magnet setting cycle. Typically, the magnet is cycled up to saturation and then back to set value. A precise determination of the field is then performed with one of the four nuclear magnetic resonance probes (NMR), covering different ranges and fed into the data analysis software.

2.6.1 *Spectrometer B detector package*

Track determination is carried out in spectrometer B by means of two vertical drifts chambers (VDC), set at about 45° with respect to the horizontal. These detectors make use of the known drift velocity of electrons in the gas mixture (80% ethane and 20 % argon), to get a more precise position determination by measuring the drift time (typical drift time = 200 ns). Timing signal is provided by the segmented planes of plastic scintillators placed immediately afterwards.

Within each of the chambers there are two planes of wires. The first one measures the position of the track in the dispersive plane. In the second, the wires are rotated 40° relative to the first in order to measure a projection in the non-dispersive plane. Spatial resolution differs for both planes due to the projection being 200µm for the dispersive plane and 400µm in the non-dispersive plane.

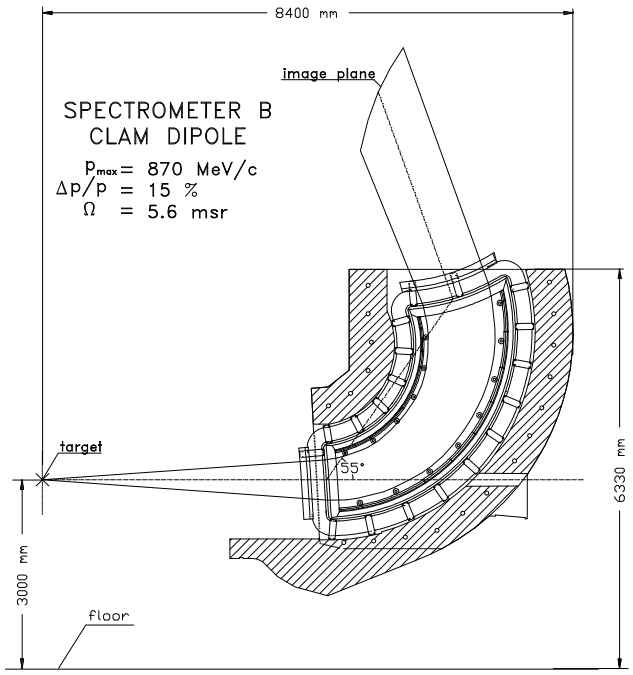

Figure 24: Spectrometer B dipole. From [65]

.

2.6.2 *Scintillator walls*

Spectrometer B is equipped with two segmented plastic scintillator planes. Each plane consists of 14 paddles (14*16 cm^2 each), read out by photomultipliers. They generate the trigger for the data acquisition of the spectrometer and provide the stop signal needed by the drift chambers. The first plane is called dE. It is 3mm thick and it is used for PID based on energy loss. Thicker scintillators (10 mm) are used in the second wall (ToF) for highly resolving time of flight measurements.

Energy deposition PID is not possible for pions, electrons or positrons, and for this purpose, a Cerenkov detector is used.

2.6.3 *Cerenkov detector*

Cherenkow detector is based on the light cone generated inside a transparent radiator when the particle speed exceeds light speed in the medium.

Seen on top of Fig.25, is the triangular shaped volume filled with freon gas (index of refraction: 1.0012). A set of mirrors is used to reflect the light back to the photomultipliers. Threshold values for electrons and pions are radically different. Electrons with more than 10 MeV/c momentum will be detected while pion detection requires a much larger momentum of at least 2.4 GeV/c. With a beam energy of 1.5 GeV this momentum is never achieved. Detection efficiency for this detector is nearly 100 %. As negative pion contamination was found

to be important during the test beam times, Cherenkov cuts were imposed on the data for reaction identification (see sec. 4.7).

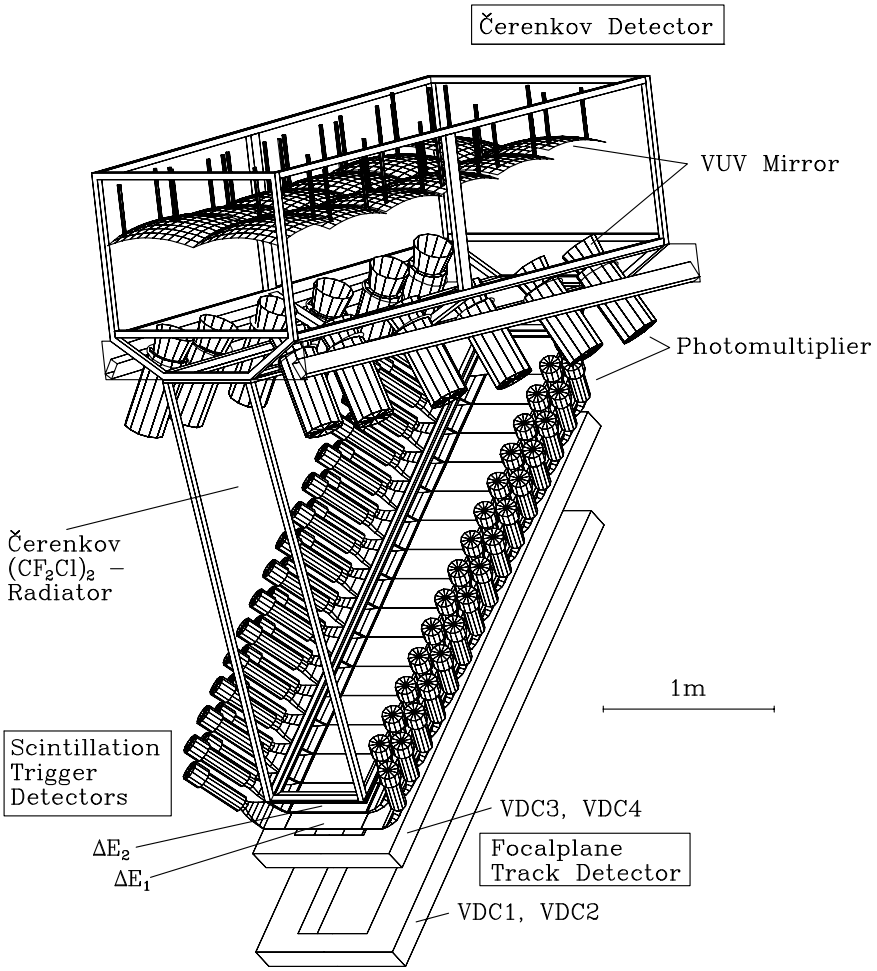

Figure 25: Detectors equipping spectrometer B. From bottom to top: vertical drift chambers, two planes of segmented plastic scintillators and a gas Cherenkov detector. From [65]

2.7 COINCIDENCE SETTING

Strangeness conservation allows tagging the electroproduced strange barion by detecting the outgoing associated kaon. Simultaneous detection of the scattered electron is used to calculate the missing mass of the system $p(e, e'K^+)$ [5], allowing hyperon identification.

5 Four momentum for the missing hyperon will be given by:

$$(E_Y, P_Y) = ((\nu + m_p - E_k), (\vec{q} - \vec{p}_k))$$

squaring we get:

$$m_Y^2 = (\nu^2 - |\vec{q}|^2) + (E_k^2 - |\vec{p}_k|^2) + 2\nu m_p - 2E_k(\nu + m_p) - 2\vec{q} \cdot \vec{p}_k$$

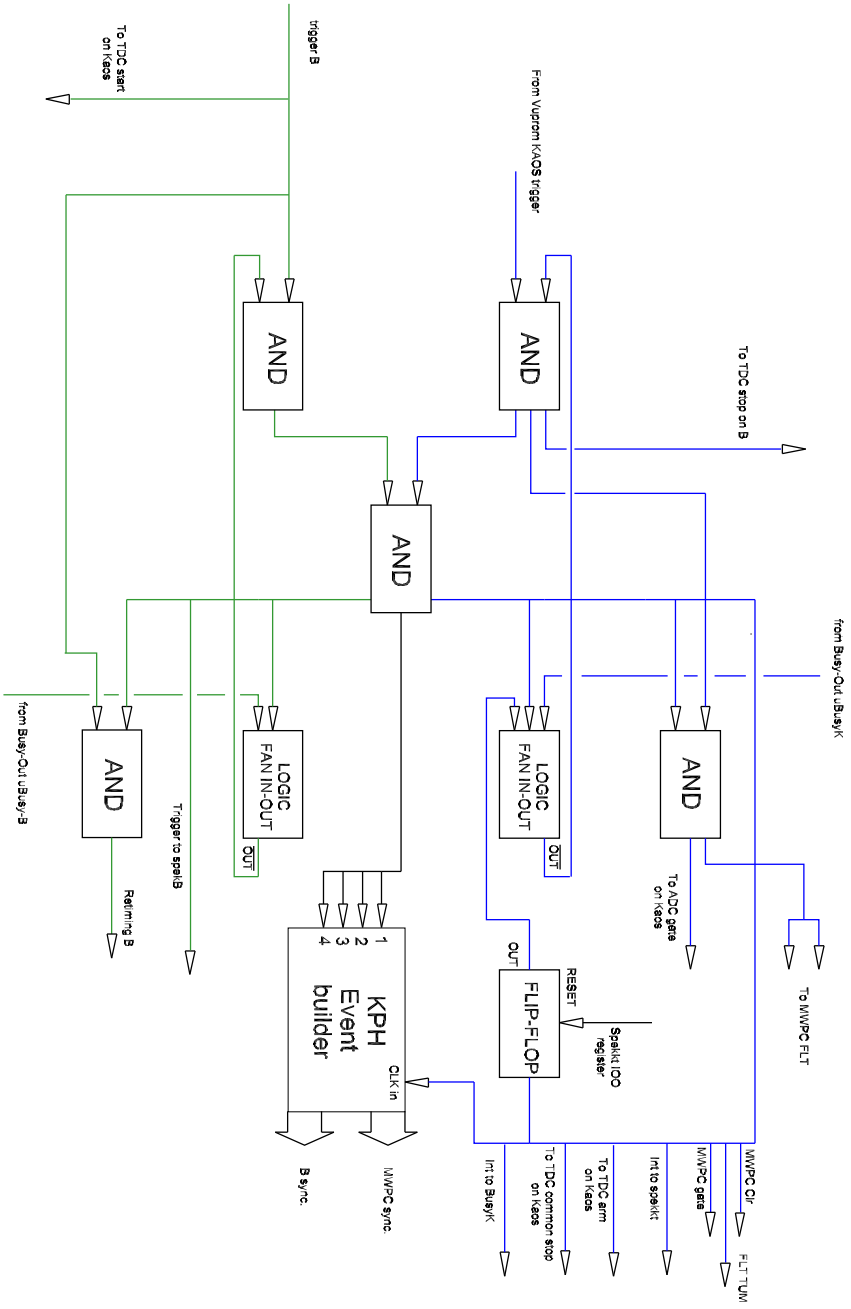

Figure 26: Simplified scheme of coincidence trigger system. Coincident single arm trigger signals arriving from Spectrometer B and KAOS logic (arrows on the left) are allowed to generated a valid trigger signal when DAQ is not busy. Arming and common stop signals for the TDC, gate signals for the ADC, interrupt signals for the front-end CPU, and additional trigger signals for the MWPC hardware (arrows on the right) are generated for each trigger event. These events are conveniently labeled for synchronisation by the in house made event builder module.

As it was mentioned in section 2.6, spectrometer B was chosen as the electron arm spectrometer. Among the set of three spectrometers it was the natural candidate, as it allowed the most forward angle electron detection (needed to maximize virtual photon flux). Both single arm triggers were combined with a dedicated coincidence electronics, shown in Fig. 26. Essentially, coincidences were recorded when data acquisition system for KAOS and spectrometer B were not busy with previous event processing. The more noise-prone KAOS trigger signal was placed inside a large spectrometer B coincidence window, in order to reduce random coincidences and dead time. Coincidence electronics was placed on KAOS platform, and trigger commands and TDC common signal had to be routed back via long coaxial cables to spectrometer B. An in house made electronic module (KPH Event bilder) labeled the events for their positioning in the data stream.

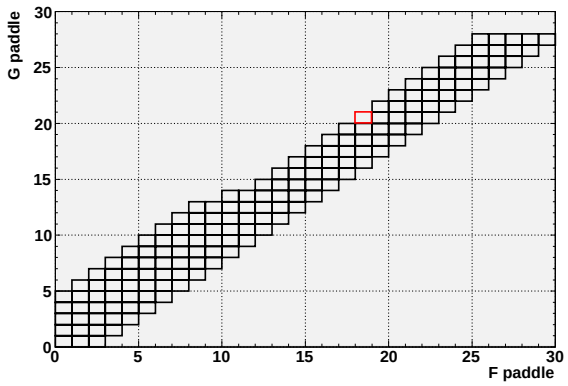

Figure 27: F vs G paddle combinations implemented in the FPGA based tracking trigger. The red square was incorrectly excluded from the logic. This error, although marginal, was conveniently handled in the simulated acceptance of the spectrometer where tracking logic was included.

2.8 DATA ACQUISITION AND ANALYSIS SOFTWARE

The set of detectors described in the previous sections provide the information needed for reaction characterization. Analog signals, generated by photomultipliers and wire chambers, are integrated and digitalized. Time differences of discriminated signals are also transformed for computer processing by TDCs in FASTBUS or CAMAC crates.

---

or:

$$m_Y^2 = -Q^2 + m_k^2 + 2\nu m_p - 2E_k(\nu + m_p) - 2\vec{q}\cdot\vec{p}_k$$

Once all the data for a trigger event has been digitalized, a home made dedicated software called Aqua++ running on Linux based VME front-end computers (located in the spectrometer platform), loads it on Aqua-defined structures. KAOS front-end CPUs are called spekk and spekkt and read the data of the MWPCs and scintillator walls respectively. The structured data from the different detectors is sent via a TCP/IP protocol through the ethernet to the online1 machine in the control room. The data goes trough a joining process first, and then is dispatched to the event-builder, where it is merged according to the information from modules that label the events of each detector, indicating event number and type. Run files with the information of positive and negative arm detectors are finally generated. This files are analyzed with another component of the A1 software package (COLA++) for event reconstruction. The final goal of this analysis is the determination of the detected particles four momenta at the target. For this purpose corrections based on energy loss on known structures and detectors are applied and track reconstruction is performed according to wire chambers information.

2.9 KINEMATICAL SETTING

For the kaon electroproduction runs, the maximum achievable energy was used. 1507 MeV electrons accelerated through the four stages explained in section 2.2 collided with a liquid-hydrogen target. Co-

Table 4: Laboratory kinematics of the kaon electroproduction campaigns of 2008 and 2009. Most of the data was taken at setting II with Λ and Σ^0 hyperons within the spectrometer acceptance.

Setting	Q^2	W	ϵ	$q_{e'}$	$\theta_{e'}$	p_K	θ_K
——	$(GeV/c)^2$	GeV	(trans.)	GeV/c	deg	GeV/c	deg
I	0.050	1.67	0.54	0.455	15.8	Λ: 0.466	-31.5
II	0.036	1.75	0.39	0.318	15.5	Λ: 0.642 Σ^0: 0.466	-31.5

incidence data was taken at two different settings with kaons in a large in-plane angular range, θ_K =21-43 deg, and in the momentum range of 400-700MeV/c. Scattered electrons were detected at a central spectrometer B angle of 15°.

Most of the data was taken in a configuration with both Λ and Σ^0 within the spectrometer acceptance. This setting with a central momentum in KAOS of 530 MeV/c and a central momentum in spectrometer B of 327 MeV/c was used during part of the 2008 beam time and continued by a longer data-taking campaign in 2009. The mean four-momentum transfer squared in this setting was Q^2 = 0.036

$(GeV/c)^2$. Table 4 shows the complete list of kinematical variables for both settings.

KAOS single arm trigger was implemented by means of the allowed F-G combinations shown in Fig. 27. This pattern was slightly wider than strictly needed to warranty a 100 % trigger efficiency. During data analysis a missing combination was localized (marked in red in the figure) and properly handled in the Geant simulation used for the acceptance calculation (see sec. 3.8).

3

DETECTION EFFICIENCIES AND DATA ANALYSIS

In short, his wits being quite gone, he hit upon the strangest notion that ever madman in this world hit upon, and that was that he fancied it was right and requisite, as well for the support of his own honour as for the service of his country, that he should make a knight-errant of himself, roaming the world over in full armour and on horseback in quest of adventures, and putting in practice himself all that he had read of as being the usual practices of knights-errant.

— Don Quijote de la Mancha
Miguel de Cervantes

3.1 OVERVIEW

A major task during the setting up and characterization of KAOS spectrometer was the determination of detection efficiencies for the multiwire proportional chambers and scintillator walls. As such, small detection inefficiencies are not problematic as long as they are well under control. For that purpose studies concerning tracking efficiency were particularly important since a large electromagnetic background was expected at the detectors location [63]; making the determination of kaon tracks difficult, as many spurious signals of similar amplitude were present in the chambers at any time. Generally speaking, tracks of heavily ionizing particles in low noise environments had a larger probability of being properly reconstructed, and tracking efficiency deteriorated with increasing beam currents.

This chapter begins by presenting the particular signal phenomenology characteristic of this type of MWPCs and the method developed to handle the multiple irregular clusters typically encountered during the spectrometer operation. Track determination was based on a maximum likelihood method where different quality factors were assigned to each candidate track considering known correlations between signals in both chambers and TOF walls. The efficiency of this method measured with a dedicated set of scintillator counters is discussed in the following sections. A clear improvement was achieved by including the vertical coordinate in the TOF paddles calculated by means of top-bottom time differences. We analyze the implementation of this additional quality factor and its impact on the tracking performance.

The particular geometry of the F wall and its aged scintillators were also an important source of detection inefficiencies. Section 4.4 is dedicated to a careful discussion of these problems. A proposal for the replacement of this wall will also be presented.

The rest of the chapter is devoted to the analysis of the data collected during the 2008 and 2009 kaon electroproduction campaigns. We begin by explaining data set characteristics and quality criteria. Particle identification methods based on time of flight and energy deposition, and the corresponding cut efficiencies are presented, along with some fine tunning methods for further detector calibration. Missing mass technique used for reaction channel ID and background subtraction based on coincidence time side bands are also explained. The chapter continues by introducing the scaling method employed for optimizing the existing data and discussing the sources of systematic errors. Finally, the Monte Carlo simulation used for acceptance calculations is presented and compared with experimental results.

3.2 TRACKING EFFICIENCY

3.2.1 *Phenomenology of MWPC signals and track reconstruction ambiguities*

As it was mentioned in chapter 2, the two multiwire proportional chambers utilize a two-stage gas amplification. They consist of a plane of anode wires with a pitch of 2 mm, symmetrically sandwiched between two planes of cathode wires (with a shorter spacing of 1 mm), along with two meshes of woven fabrics of plastic, called grid and transfer; coated with a nickel layer, making up two planar electrode structures, called transfer-gap and pre-amplification gap. The cathode wire directions are orthogonal to each other, the wires of the anode plane are in the diagonal direction, making an angle of 45 deg.

The purpose of the two MWPCs is the determination of the particle track outside the dipole magnet. Ideally, the transversal coordinates x and y would be accurately measured and the straight line connecting the hits in the planes defined by L and M would coincide with the actual track of the detected particle. However, ambiguities will appear when more than one particle crosses the chambers during the microsecond span the charge integrating window is opened. For the case of multiplicity 2, the eight coordinates can in principle be combined to give 16 different tracks. The situation, of course, gets even more complicated when several background particles are detected in a single trigger event. Additional difficulties arise as a consequence of the complex electrode structure of this type of wire chambers. Since charged particles usually cross the chambers with some angle, the pregap amplified signal (drifting perpendicularly to the MWPC plane) will be displaced with respect to the weaker direct signal in the cath-

ode planes. These two signals however are sufficiently separated in time, and an appropriately chosen charge integrating window could in principle get rid of the unwanted doubling. Another observed phe-

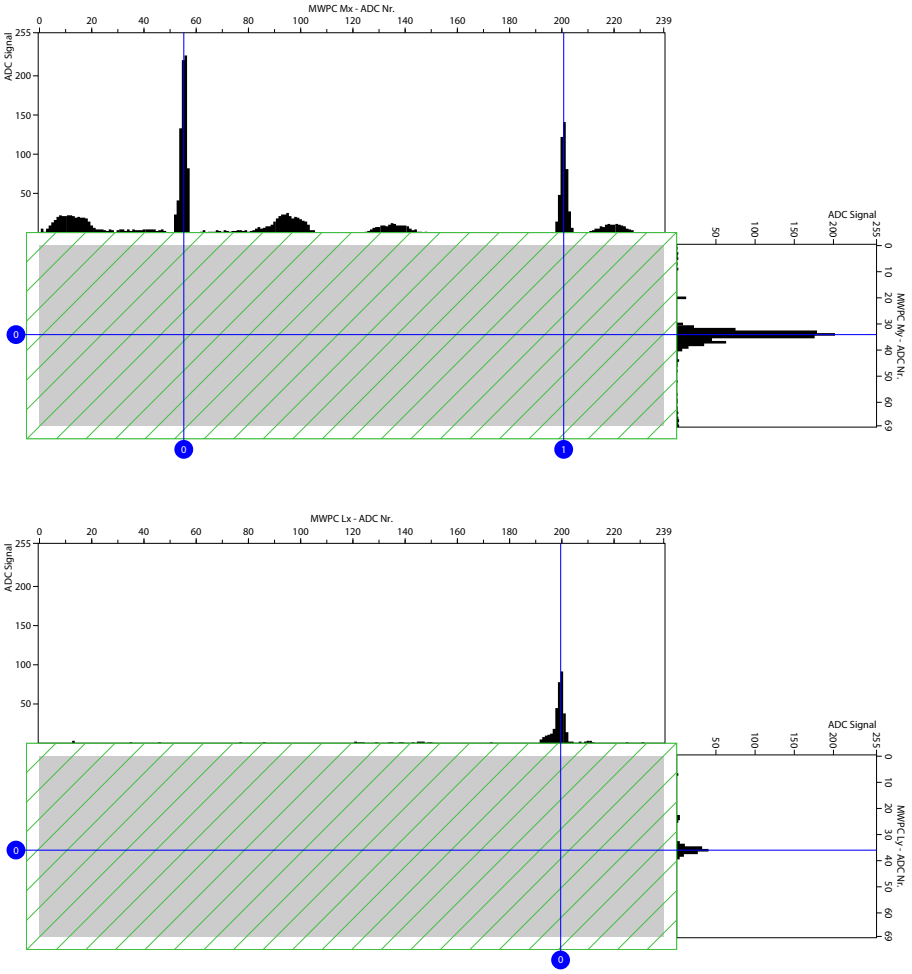

Figure 28: Sample event in MWPCs where rejected satellite peaks are clearly visible in Mx. The cluster algorithm also disregards the asymmetric shape of My and Lx peaks for the center of charge calculation and rejects small noise signals.

nomenon is related with the capacitive coupling between anode and cathode. Satellite peaks (see Fig. 28) are generated in strong correlation with the vertical position. Here, also the time signature is clear enough, and the unwanted peaks can be removed by an appropriate integration window for single hit cases. Unfortunately, these effects can not be completely accounted for, since the only reference time is given by the trigger signal, and particles delayed or advanced in time will have a shifted signal signature. As a consequence, in multiple hit events a complex ADC pattern will be observed in both coordinate directions. The width, amplitude and shape of the resulting peaks strongly depends on the variation of gas mixture, high voltages and particle trajectory angle.

3.2.2 *Cluster analysis*

For single hit events, a well defined peak like cluster will populate several ADC channels in both coordinate directions. As the FWHM of the distribution of the induced charge is known to be nearly equal to twice the anode-to-cathode gap, clusters of 3-5 read-out strips are expected for the signals. The position of the center-of-charge of the ion avalanche along the anode wires does in principle provide, for this simple case, a good measurement of the actual coordinates of the intersection point of the particle track with the grid plane [1]. For higher multiplicities, the situation is substantially more complicated: Noisy channels, multiple hits on the chamber, induced signals in the electronic chain and drifting charges will in general result in a complex spectrum where it will be far from obvious how to define a single cluster. Clearly, the charge centroid, simply evaluated from the measured charges on all cathode channels, will not correspond to the trajectory position. Therefore, it is of practical importance to find an algorithm which gives the best position resolution and highest efficiency, using a limited number of cathode strips of selected clusters. A careful study of signals phenomenology performed by Professor Achenbach ended up in an algorithm whose implementation resulted in a substantial improvement of the tracking system. We quote it here for completeness but we refer to [66] for further details:

Peak positions are determined by calculating the centre-of-charge from a restricted number of cathode channels forming a cluster. Clusters are defined by neighboring cathode strips with ADC values above a given threshold. A cluster must consist of at least 2 ADC channels and can include a maximum of 1 ADC channel with a value below threshold. Each cluster is further analysis for its internal structure to identify possible peak positions as follows: A truncated cluster is created around the channel with the charge maximum. It extends to the left and to the right for 2 channels, if the charge values for these channels are below a minimum of 90% of the charge in xmax. The truncated cluster extends at most up to the limits of the original cluster or up to a channel with only a minimum of charge. For clusters that reach the 8-bit maximum of the ADC the counting of channels starts at the left and right limits of the saturation plateau. If no such structure is found the cluster is discarded. This procedure ensured that a truncated cluster corresponds to a peak-like structure. Next, the summed charge in the truncated cluster is compared to the charge outside the peak region. If the latter is larger than 30% in the x-planes of the MWPC or larger than 1% in the y-planes of the MWPC and the outside region is wider than the required minimum for a cluster, a

1 Note that, altought measured signals are induced and read out from the cathode planes, the actual hit position is located in the grid plane since the avalanche starts there and drifts towards the anode perpendicularly to all planes thus conserving the coordinates value.

separate cluster is created. The difference between the x- and y-planes is attributed to the different appearances of pick-up charges on the cathode wires. The extension of the new cluster is depending on the distribution of charges. For a large charge close to the original peak, i.e. within 2 channels, the new cluster extends to the peak region, otherwise to the border region. This construction avoids the creation of extra clusters when fluctuations appear in the tails of the original peak.

Fig. 28 shows a typical event where this algorithm has successfully localized the physical events. Satellite peaks and small noisy signal have been rejected and the asymmetries of two peaks are not considered for the center of charge calculation.

3.2.3 *Track finding method*

Once a set of clusters has been found for both chambers and coordinated directions, a typically large number of tracks can be formed by grouping them in different ways. A set of quality factor is assigned to each candidate track, considering the correlation between the induced signals in both cathodes for a given chamber and the angular restrictions imposed by the spectrometer acceptance. Additional quality factors are obtained by studying the coherency with the information provided by the scintillator walls. In a first version of the tracking code, only hit paddle number was utilized for comparison with the predicted intersection points of the candidate track with the walls planes. In an improved version of the code, timing information from top and bottom photomultipliers was also used to define a vertical position reconstruction quality factor (see section 4.2.5). The resulting overall quality for a given track defines a measure of its likelihood as a real particle track [66]. If the track with maximum likelihood reaches a convenient quality threshold, is returned by the code and employed by the analisys software to determine particle kinematical variables.

3.2.4 *Efficiency counters*

A dedicated set of efficiency counters were built to measure tracking efficiency for the abundant pions and protons at currents up to 4 μA. The relatively large overlap between the created charge for these two particle species permitted the extraction of the corresponding value for the K^+ mesons. In order to reduce as much as possible any perturbation on the particle trajectory, a 5 mm thick BC408 scintillator plastic was chosen. A rectangular piece of small dimension ($3 \times 3 cm^2$) was connected to an optical guide and read out by a Hamamatsu tube type R1828. When attached to the MWPC, the active area of the counters was vertically centered. The detectors could be easily rotated out of the acceptance to eliminate any disturbance on data taking

Figure 29: Efficiency counters placed in front of the MWPCs. A 3cm x 2cm x 0.5 cm piece of BC408 plastic scintillator vertically centered in the active area of the chamber is connected to a light guide 20 cm long and read out by a Hamamatsu PMT. Another twin counter is placed in front of MWPC L. A typical track crossing chamber M is shown in green. In order to define an event for the efficiency measurements, a hit in proper F and G paddles is also demanded to insure that MWPC L is also crossed before a possible decay

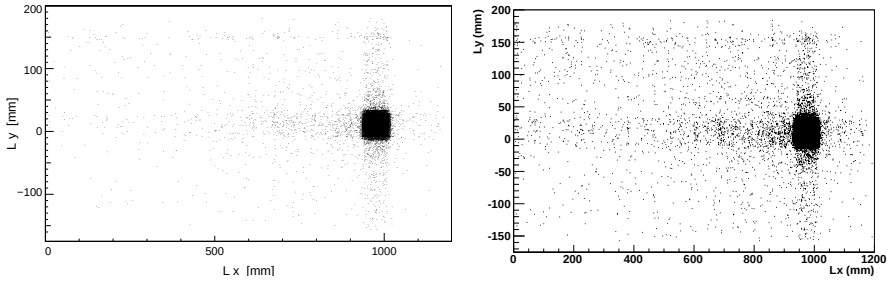

(a) 2uA (b) 4uA

Figure 30: Reconstructed x and y coordinates in MWPC L at 2 and 4 uA beam currents for efficiency counters triggered events. The rectangular acceptance defined by the efficiency counters on the MWPCs planes is clearly observed. Crossing bands are the result of wrong x or y reconstruction. Clearly, track finding becomes increasingly complicated for large beam currents as a result of the high multiplicity generated by background tracks.

runs. Both detectors were placed at the same relative position in their respective chambers (see Fig. 29, for a photo of the efficiency counters placed at their working position and a standard track crossing both detectors).

KAOS flexible logic based on FPGA universal logic modules (VUPROM) allowed the implementation of a trigger for the efficiency counters. An specific program was created that triggered the data acquisition system whenever a coincidence of both detectors was observed. Threshold values allowing minimum ionizing particles to be detected with almost 100 % efficiency were chosen in the corresponding CFDs. The counters were fully integrated in KAOS read out electronics so that TDC and ADC information was also available. Spare channels were used for this purpose.

Fig. 30 shows the reconstructed x and y coordinates in the MWPC L when coincidences of both efficiency counters were used for triggering the data acquisition for beam currents of 2 and 4 μA and the same number of events. The projected area of the small scintillator on the chamber is clearly visible. The bands in the x and y directions are the result of events where one of the coordinates was wrongly reconstructed. It is apparent that larger currents lead to more errors of the track finding algorithm.

Fig. 31 shows a typical case where the right track (in black) has been found after the rejection of many other cases (in yellow and grey), where the corresponding likelihood was calculated to be smaller. The difficulty of the problem is clear. In the data analysis, a track will be accepted if its quality factor is beyond an appropriately chosen threshold value. As an example, events in the two bands shown in Fig. 30 are typically rejected as they present a very low quality factor.

Some tracking efficiency is also lost since within the set of rejected tracks there is a non zero probability of having correct ones.

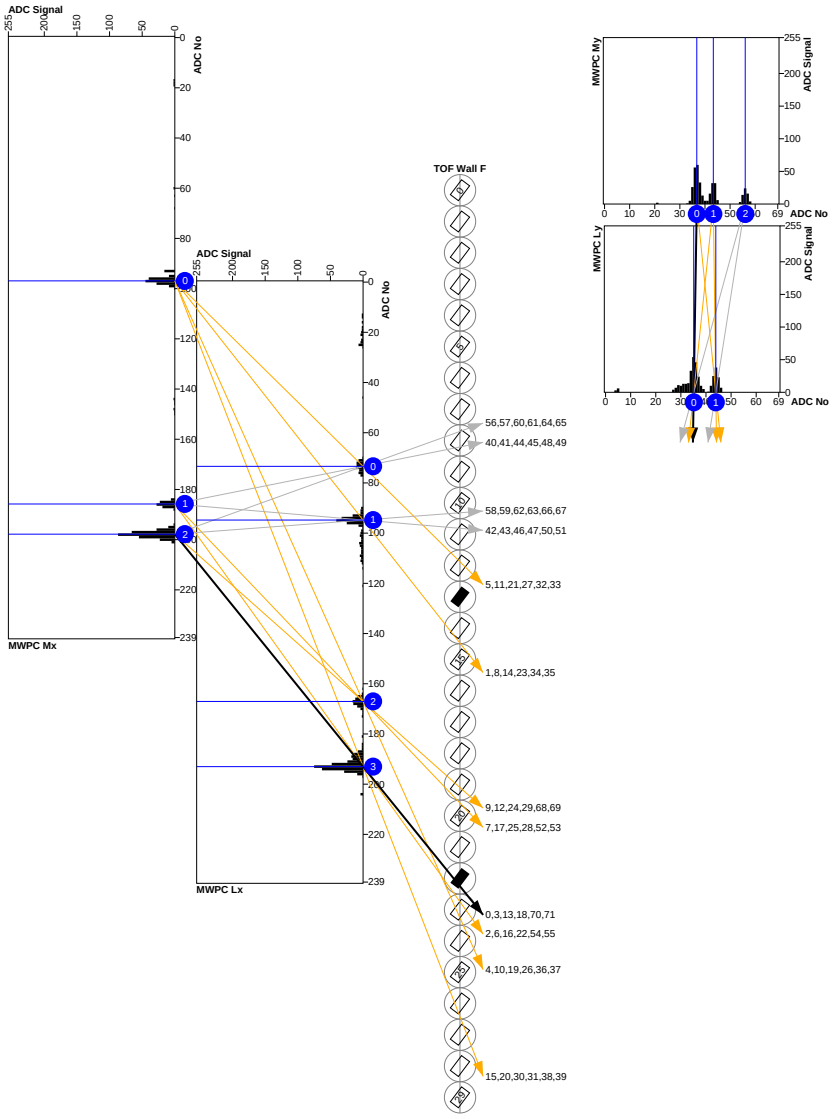

Figure 31: Reconstructed tracks in a typical event, triggered by a coincidence of the two efficiency counters. Hits on F wall as well as MWPC ADC channel values are shown in black. The correct track, thick line, has been singled out among other candidates using the highest quality criterium.

3.2.5 *Scintillator walls top-bottom timing used for vertical position reconstruction*

MWPCs duty is to provide accurate information about the trajectory of charged particles. Unfortunately, as it has been explained, several factors give rise to ambiguities that make the task of track determination difficult. The inclusion of the efficiency counters in the detector system

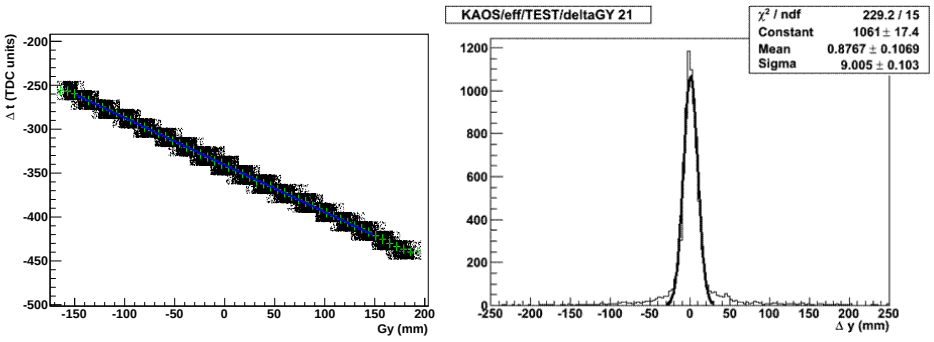

(a) (b)

Figure 32: (a) Linear fit used for calibration of the time difference for a sample G wall paddle. The fit was done to the set of points obtained by subtracting a constant background from each bin, and then taking the average of the time difference at each y position bin. (b) Position resolution achieved with top-bottom time difference. The curve was obtained by choosing a 1 mm band around $G_y = 0$ and histograming the time based G_y position. The resulting FWHM = 2.1 cm averages the contributions from protons and pions.

revealed that approximately 40 % of the miss-reconstructed tracks had only the vertical coordinate in one of the two detecting planes wrongly determined. The fact that scintillator walls are equipped with PMTs on top and bottom extremes for each paddle and their independent TDC read out, allows a rough determination of two more vertical coordinates for the intersecting points of the particle trajectory with F and G walls. This method is based on the fact that typical time resolutions for this type of scintillator walls are in the order of a few hundred ps. Taking into account that effective light speed in the plastic material can be even smaller than half the speed of light in vacuum, position resolutions of a few centimeters can in principle be obtained (see Fig.32(b)). This allows for a strong condition to be imposed on track candidates. Fig. 32(a) shows an example of the linear fit used for calibration of the top-bottom time difference. The fit was done to the set of points obtained by subtracting a constant background from each bin and then taking the average of the time difference at each Y position bin [2].

2 During this calibration procedure, an anomalous band was discovered in the histograms slightly over the background level (see Fig. 33). The investigation of its origin proved that it only appeared in coincidence events. A dedicated study showed that reflected signals traveling back from the splitter input to the PMT and then forward again were able to cross the CFD threshold level (if the original amplitude was large enough). The corresponding CFD outputs created a new single arm trigger signal with a fixed time delay. Only one of the original start signals (wall F) followed the arm signal generated by the delayed random coincidence at sufficient distance to be accepted (since cable length for both walls was not equal). That explained the observed fact that absolute time values for F were much larger than for G. The different slope of the anomalous band was related to the fact that the amplitude of

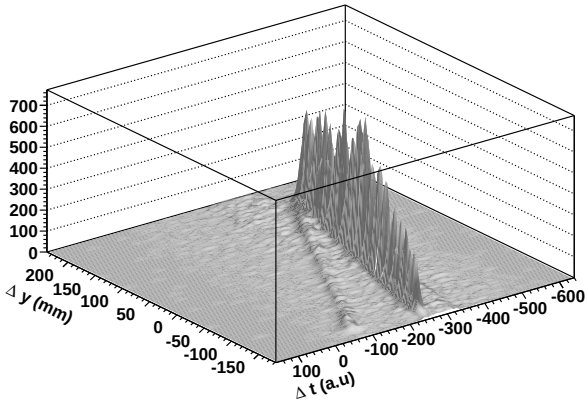

Figure 33: An anomalous band with a modified slope can be observed in Δt vs Gy (left structure), as a consequence of the time delay of reflected signals that are able to cross the low threshold used in the CFD (see foot note).

The fit parameters for all paddles in F and G where introduced in the data analysis software and used to predict the Y coordinate from the measured top-bottom time differences. Tracks predicted by the hits in the MWPC were projected to F and G and the corresponding hit position was compared with the time-based calculation. A quality factor was calculated according to the degree of coincidence of both numbers. Once the corresponding quality factor was included in the track finding algorithm, the improvement in the Y coordinate reconstruction was notorious (see Fig. 34)

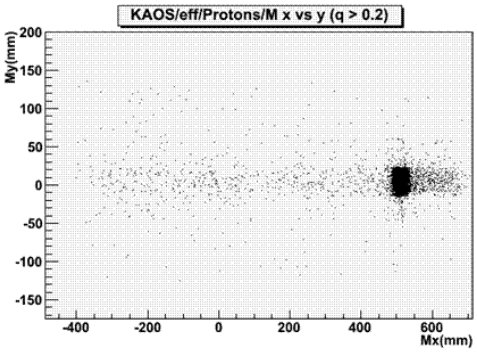

Figure 34: Effect on the reconstructed coordinates in M chamber when the quality factor extracted from the Top-Bottom time difference is used. Tracks in the vertical band (wrong y coordinate) almost disappear when this factor is included in the likelihood calculation.

the reflected signal was very small entering the regime in which the CFD showed a strong walk effect.

3.2.6 *Efficiency definition and results*

We will define an intrinsic efficiency for each chamber, considering that a particle has been detected whenever a cluster or more are localized in both coordinate directions -a somehow relaxed definition-. If a track can be formed out of the clusters measured in both chambers, we will count it as genuine detection and define a corresponding track efficiency. If the track with the maximum likelihood happens to be within the acceptance region of the efficiency counters, we will catalog it as a valid track. The ratio of this type of events and the trigger events[3] constitutes a precise enough and experimentally determinable definition of tracking efficiency. All these defined efficiencies depend to some extend on the cluster analysis and the reconstruction parameters. We found these numbers to be strongly dependent on the signal

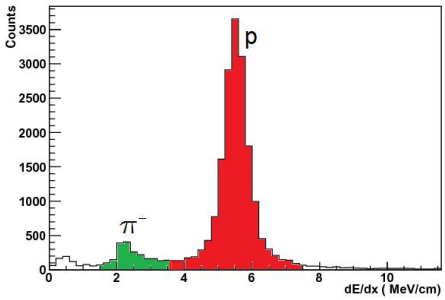

Figure 35: ADC spectrum for a G paddle within the acceptance of the efficiency counters. Protons and pions are neatly separated by their energy deposition. Separated efficiencies for these particles are given table 5.

amplitudes. Fig. 35 shows the ADC spectrum of the G paddle in the center of the acceptance of the efficiency counters. A clear separation of pions and protons can be achieved by their different energy deposition. A cut in this magnitude allows a particle specific calculation of the tracking efficiency. Table 5 shows the results of the efficiency measurements for different beam currents [4]. The large overlap between induced charge for pions and protons allowed a determination of the tracking efficiency as a function of collected charge (see fig. 36(a)). The resulting curves were used to extract kaon tracking efficiency showing variations in the range 75%–90%.

Tracking efficiency was also evaluated as a function of track quality (see Fig. 36(b)). The continuous increase of the efficiency with the

3 Further conditions are actually included to define a trigger event for these efficiency measurements: An event is defined in the efficiency runs by demanding a hit in F between channels 20 and 23 and in G between 19 and 22. Time signals in F or G are also demanded. These restricted class of events guaranties that the L chamber has also been crossed by the charge particle and defines the efficiency used in the cross section determination.

4 The stability of these results was evaluated by taking periodic runs during 2 weeks, showing only small variations of no more than 2 %.

Table 5: Tracking efficiencies defined in the text for beam currents up to 4 μA. Differences between both MWPCs are due to an slightly larger gain for chamber L. Efficiencies for protons are significantly larger than for pions, specially at large beam currents, since their large energy deposition allows an easy discrimination in the background of minimum ionizing particles as compared to the pion case where signal and background amplitudes are very similar.

Beam current	intrinsic		Tracking			Protons		Pions	
I(μ A)	L	M	any track	L	M	L	M	L	M
1	99.3	99.6	98.3	96.3	95.6	97.7	96.9	85.5	83.7
2	99.5	99.7	98.2	95.0	93.1	96.6	94.8	82.4	78.8
3	99.6	99.8	98.2	93.2	90.3	94.9	92.1	80.4	75.2
4	99.6	99.8	98.1	91.6	87.4	93.7	89.8	75.2	68.0

quality proved that quality was a good indicator of correctness in the reconstruction.

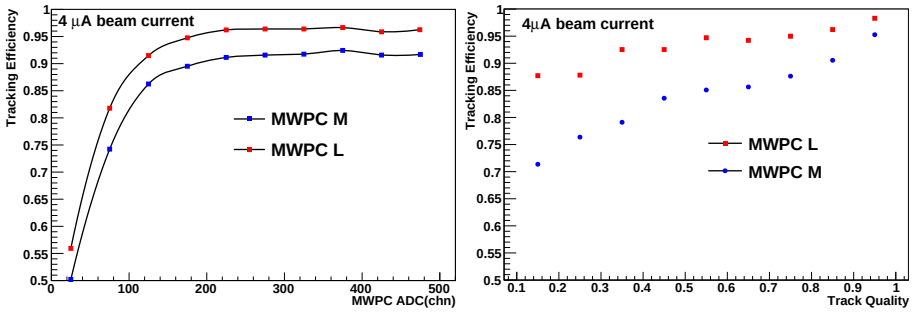

(a) (b)

Figure 36: (a) Tracking efficiency as a function of deposited charge in L at 4 μA, the maximum beam current employed during data taking. Separated values for both chambers are given, considering whether or not the selected track had coordinates within the acceptance defined by the efficiency counters. (b)Tracking efficiency evaluated at equally spaced track quality intervals for a beam current of 4 μA. A track is consider properly reconstructed if it falls on the acceptance defined by the efficiency counters. The plot proves that track quality is a good indicator of correctness in the reconstruction.

3.3 SCINTILLATOR WALLS INEFFICIENCIES

F wall scintillators are tilted in the direction of the incoming particles. In the kinematics used during the 2008-2009 beam times, the gaps between the paddles resulted in inefficiencies mainly for low momentum and large angle.

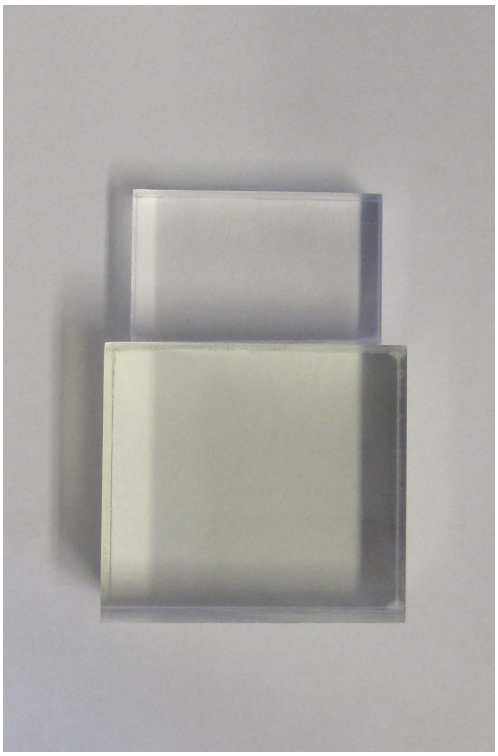

Figure 37: Aging due to radiation damage for a piece of F wall plastic scintillator as compared to a new scintillator of the same type.

There was a troublesome midarea where positively charge particles touched just slightly the plastic bars, and due to the relatively large aging of the plastic scintillators (see fig. 37), and depending on the threshold applied to the CFD, part of the events were lost. Fig. 38 shows the results of a Geant simulation where a variable degree of inefficiency as a function of the kaon momentum and angle of the trajectory is seen for a threshold accepting perpendicular incidence of minimum ionizing particles. This inefficiencies, although disturbing, were properly accounted for in the data analysis via their influence on the calculated generalized acceptance of the spectrometers.

With the removal of the magnetic quadrupole used at GSI for vertical focusing, the acceptance of KAOS spectrometer was limited by both scintillator walls and MWPC vertical dimensions. Fig. 39 shows the result of a Geant simulation where particles generated at the target were tracked trough the magnet until their hit position in the planes defined by F and G. The horizontal lines are the actual detector edges. It can be seen that there is a substantial acceptance reduction due to

the scintillators size. A KAOS at MAMI matching design would have

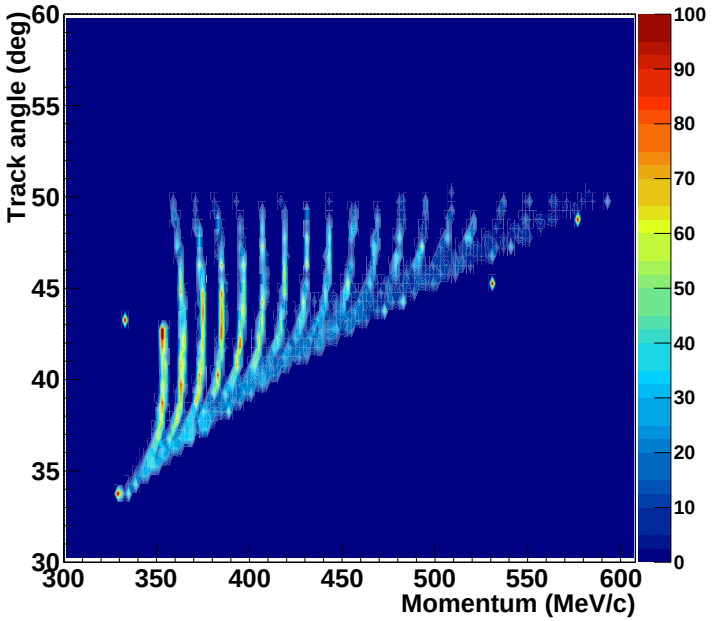

Figure 38: Inefficiencies due to the gaps between F wall scintillators. The angle is measured with respect to the normal of the MWPC. A threshold is set in the simulation so that minimum ionizing particles are detected for perpendicular incidence on F paddles.

vertically extended continuous walls for correcting both efficiency reduction problems. A replacement of the F wall would improve the overall performance of the spectrometer.

At the time of submitting this thesis, a new scintillator wall (H) designed by Florian Schulz during his Diplom Arbeit [67] is already fully functional at KAOS spectrometer. Mimicking G wall a set of 30 new paddles (580 x 70 x 20 cm^3) of the same material type (BC-408) have been used to construct a continuous flat surface. The existing phototubes have been reused for the new wall, since their performance was considered correct. G wall has been relocated to the previous F position and the new (vertically larger) H wall has been placed at a larger distance from the focal plane to allow single arm time of flight measurements. Excellent time resolution of the order of 300 ps is achieved due to the much larger light yield of the new scintillators and the high quality optical cement and assembling techniques employed. An independent tracking algorithm have been developed based on walls segmentation, top bottom time differences and the newly implemented Cherenkov detector. The set of quality factors extracted for track evaluation can be tuned to single out particle species, allowing a scintillator walls plus Cherenkov mode operation of the spectrometer. The larger acceptance of the spectrometer in this operation mode has

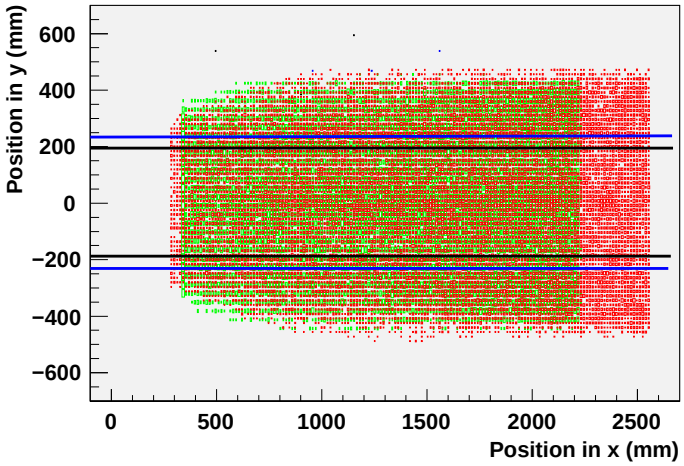

Figure 39: Trajectories simulated by Geant, only limited by the geometrical acceptance of the magnet window, are tracked till the planes defined by F and G. Horizontal lines show actual wall sizes (F in black and G in blue). It is clear that large inefficiencies results from the limited vertical dimensions of the Walls.

been employed in a first hypernuclear experiment, where only Kaon tagging at low momentum resolution was needed.

3.4 COLLECTED DATA AND RUNS SELECTION

KAOS experimental program started with two kaon electroproduction campaigns in the years 2008 and 2009. The detailed knowledge of the spectrometer performance and operation acquired during several previous characterization beam times allowed an almost failure free data taking. Altought most of the runs were taken at 2 μA, data was also taken at 4 μA and 1 μA [5]. Kinematics was chosen so that Λ an Σ^0 reaction channels falled within the acceptance (this excludes the first half of the 2008 data where only Λ production was studied).

The data collected in 2008 corresponds to effectively 6 days of beam time with a total integrated luminosity of 284 fbarn^{-1}. The main kaon electroproduction campaign carried out in 2009 accumulated 244 hours of beam time at 2 μA (14 % dead time), and 38 hours at 4 μA (45 % dead time). This resulted in a total luminosity-after corrections- of aproximately 2300 fbarn^{-}1.

A slightly reduced set of physical runs was obtained after several diagnostic tests to exclude possible undetected problems during data taking. Coincidence rate, kaon production rate, luminosity, beam current and data acquisition system dead time where monitored for this purpose (see Fig. 41).

5 Tracking efficiency was well under control at these other currents, as it was explained above.

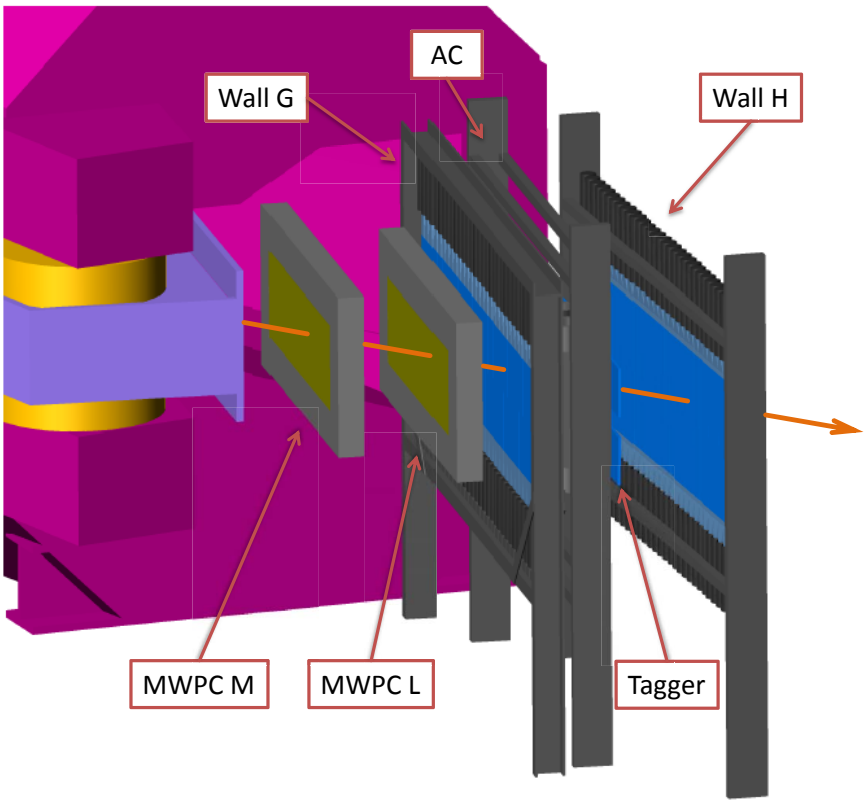

Figure 40: New scintillator wall H integrated in KAOS detector system. The distance from focal plane to the H wall has been increased in order to allow single arm TOF pid. The new Cherenkov detector can also be seen in the figure between both scintillator walls.

3.5 PARTICLE IDENTIFICATION

By definition, particles with equal momentum hit the focal surface of the spectrometer at the same position. According to Bhete-Bloch equation, energy deposition per unit length for a given charge state depends only on the particle velocity. If a thin detector could be shaped like and placed at the location of the focal manifold, particle identification (PID) would be neatly accomplished by measuring energy deposition at each detector point (since different particle types would in general have different masses and consequently different speeds).

The relativistic relation between momentum and speed introduces the first difficulty in this PID method. Since particle momentum can be increased with no limitation but velocity can not go beyond the speed of light, highly energetic particles would need high dE/dx resolutions for their proper identification. The statistical nature of energy deposition of charge particles in matter introduces an intrinsic limitation to that resolution. The second difficulty is related with the fact that practical detectors for energy deposition can not be easily curve shaped. Kaos spectrometer is equipped with two scintillator walls with flat geometry. One of them, F, has a relatively large overlap with the focal manifold. The second one, G, can also be considered a good PID detector since it sits very close to F. The fact that this two detectors do not coincide precisely with the focal manifold introduces an additional width in dE/dx vs position since some spreading in the momentum distribution is expected for each particle type at a given location. In addition, a phenomenological model is needed instead of Bethe-Bloch equation. This problem can be partially solved by using tracking information to calculate particle momentum (given by the intersection of linear track with focal manifold). A histogram of energy deposition vs momentum can then be constructed recovering to some extend the width the ideal detector would provide. Of course this procedure is limited by the intrinsic position resolution of the tracking detectors and the errors in the focal manifold calculation. From a practical point of view, both methods have to be compared and the one providing the best particle separation should be used.

Time of flight (TOF) information is also used in the data analysis as a PID method. Time of flight between two points separated by a distance L is related to particle momentum by $\Delta t = \frac{L}{c}\sqrt{1+\frac{m^2c^2}{p^2}}$. Consequently, particles with the same momentum but different masses will have different TOF. In order to measure a time difference, two timing signals are necessary. The original configuration of KAOS spectrometer at the GSI facilities made use of a start detector placed between the quadrupole (now absent) and the pole shoe dipole. Since this detector was removed from the spectrometer for its present configuration, the missing timing signal has to be provided by the electron arm spectrometer. Particle production at the target is considered simultaneous,

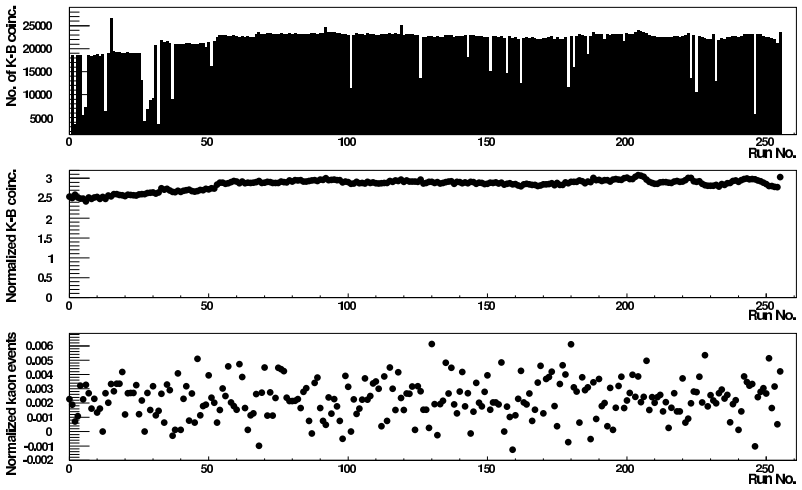

(a) (top) KAOS and Spectrometer B coincidences per run. When run time is taken into account, a normalized histogram is obtained (middle). Normalized number of identified kaons (bottom).

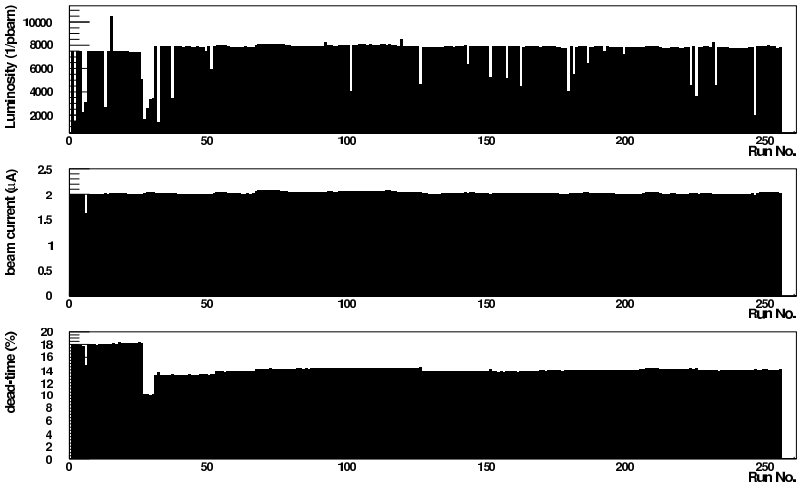

(b) Luminosity, beam current and data acquisition system dead time.

Figure 41: Several diagnostic tests are applied to physics runs in order to exclude those presenting abnormalities that might introduce uncontrolled errors in the cross section determination.

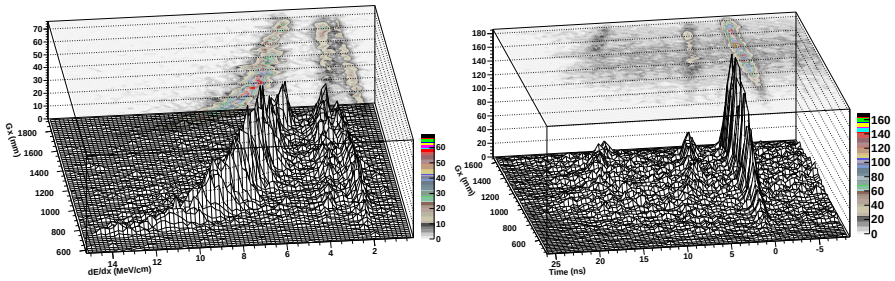

(a) Energy deposition per unit length as a function of horizontal coordinate (x) in G TOF wall after a cut in TOF for kaons. Protons (curved left band) are clearly separated but kaons (center) and pions (right) show some overlap.

(b) Time of flight as a function of x coordinate in G TOF wall after a cut in energy deposition for kaons. Here bands corresponding to protons (right), kaons (center) and pions (left) are clearly separated.

Figure 42

and since PID at the electron arm is trivial (pions are easily rejected by Cherenkov detector), the good tracking characteristics and momentum resolution of spectrometer B is used to determine the collision time.

Knowledge of particle momentum and MWPCs information (for proper track reconstruction) is then used for an offline path length calculation. When this information is employed for correcting the histogram of TOF vs horizontal position in the scintillator walls and a cut in kaon energy deposition is performed, nicely separated bands are obtained for each particle type.

PID based on energy deposition is more complicated since there is some overlap at large momentum of the pion and kaon bands (see Fig. 42).

3.6 GENERIC CUTS APPLIED TO THE DATA

In order to reduce pion contamination, PID energy cut has to be relatively narrow. Thinner particle bands allow a more effective PID and a signal to noise ratio improvement. For this purpose, a fine tuning of channel gain was performed. For the momentum acceptance covered by KAOS, pions are effectively m.i.p. . Gain calibration was performed by assuming that the profile obtained by taking the average value at each Gx bin should resemble as much as possible an straight line. Variable gain factors for each channel were used as parameters for a fit in which the absolute value of the difference between the profile values and the model was minimized. Fig. 43 shows the results of the code written for such a fit. On the top, black points indicate the G wall paddle joining points. The constant energy deposition assumed for m.i.p is plotted in red. The green curve is the original profile obtained from the analysis of data runs. In blue the profile after the fit is shown.

It can be observed that in some cases the gain was reduced while in others a correction larger than one was needed (see table 6).

Table 6: Gain correction factors (α) obtained by the fit shown in Fig. 43

channel	α	channel	α	channel	α
0	1	10	0.98547	20	1.02939
1	1	11	0.99599	21	1.03002
2	1	12	1.02585	22	1.02056
3	1	13	1.02974	23	1.04917
4	1	14	1.03469	24	1.04698
5	1	15	1.01149	25	1.03456
6	1	16	1.01121	26	0.999973
7	1	17	1.04263	27	0.902993
8	1	18	1.0459	28	1
9	1	19	1.02201	29	1

The fraction of kaons lost in the cut was calculated by fitting a set of three Gaussian functions plus a constant background to slices in Gx. The mean value of the kaon Gaussian for each x bin was recorded and used to extract a linear fit to the kaon band. This simple model was accurated enough for kaons in the momentum acceptance of spectrometer. Fig. 44 shows a sample of the outcomes of the program used for the cut efficiency determination. In the first plot (a), the set of three Gaussians plus constant background used for fitting one of the Gx slices is shown. Mean square deviation for the kaon Gaussian is shown in the next graph (b) for each slice. In plot (c) the linear fit to the kaon band is presented. Parallel lines defining the cut at one sigma distance are also visible.

A second calculation was performed in order to confirm the previous results. Here, a different approach was used. A model function of the two variables Gx and dE/dx was designed and fitted to the 2D histogram. The model function assumed a Gaussian shape in the dE/dx direction with a variable mean value following two straight lines (one for kaons with a non zero slope and a constant for pions). For the maximum value of each band at different Gx position, a constant value was taken for pions and a linear function for kaons. The results are shown in Fig. 44(d). The corresponding sigma value in this fit was 0.32, validating the results of the previous analysis.

Based on this fits, the specific energy loss corrected for the expected kaon energy loss was required to be within $|E_K| < 640$ keV. A similar analysis determined that the flight time corrected for the expected kaon flight time, t_K, should be required to be within $|t_K| < 1.2$ ns.

Electron identification in Spectrometer B was based on Cherenkov signals allowing an efficient rejection of negative pions. Especifically

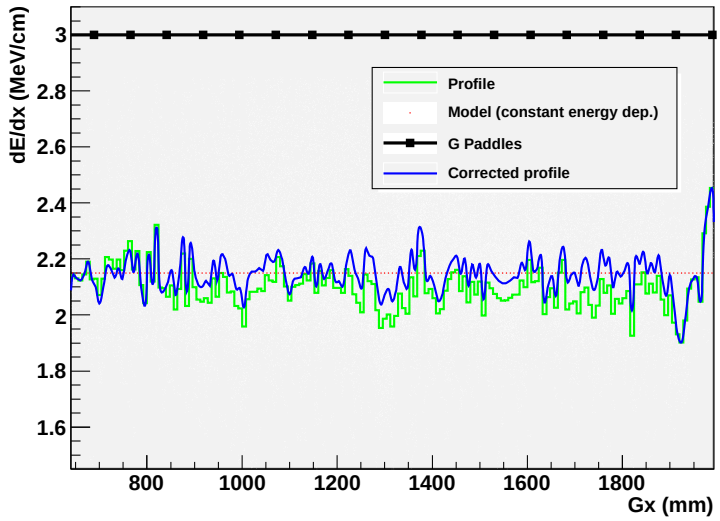

Figure 43: Results of the C code macro written for fine tunning of gain factors. On the top black points indicate the G wall paddle joining points. In red the constant energy deposition assumed for m.i.p.. The green curve is the original profile obtained from the analysis of data runs. In blue, the profile after the correction is shown. It can be observed that in some cases the gain was reduced while in others a correction larger that one was needed.

a signal in the sum of all five Cherenkov counter amplitudes was demanded in the data analysis. Angular and momentum cuts were also applied to the electron arm to constrain the analysis to a region of well known spectrometer performance. The polar angle at the target was required to be in the interval defined by -4.0° < θ_0 < 4.2° while the azimuthal angle was restricted to -1.2°< ϕ_0 < 1.1°. Deviation with respect to the central momentum was limited to 7 %. All these values were used before in several experimental setups with spectrometer B participation and are well documented and considered optimum.

Cuts in KAOS data were defined by:

-10.5°< θ_0< 7.3°

θ_0< 5° + 0.83° ×(δp+ 17 %)

θ_0> 0.2° ×(δp− 20 %) - 6.5°

to restrict the acceptance in the hadron arm to a region where agreement between the Monte Carlo simulation and the analyzed data was good (see Fig. 51).

Only a quality cut was applied to MWPC track reconstruction by demanding: Track quality > 10^{-3} what ensured that only good quality tracks were accepted.

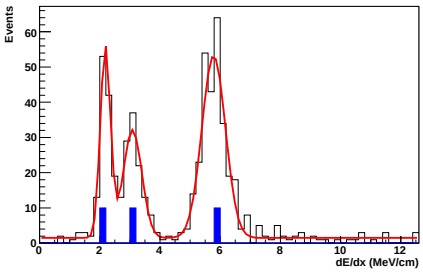

(a) Fit for energy deposition per unit length at fix Gx bin.

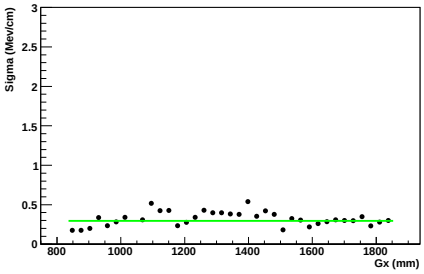

(b) Mean square deviation for each bin slice and average value.

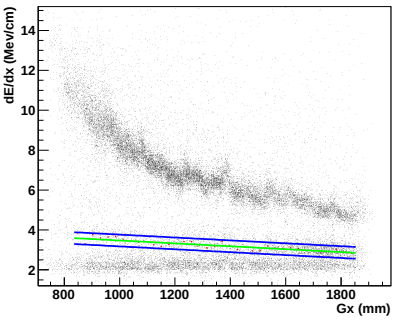

(c) Linear fit to the mean kaon Gaussian value. One sigma cut.

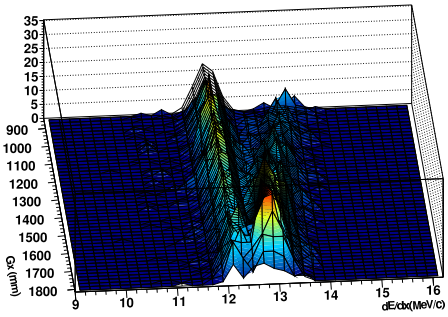

(d) Kaon and pion bands 2D fit.

Figure 44: Sample of the outcomes of the program used for the cut efficiency determination. In the first plot (a), the set of three Gaussians plus constant background used for fitting one of the Gx slices is shown. Mean square deviation for the kaon Gaussian is shown in the next graph (b) for each slice. In plot (c), the linear fit to the kaon band is presented. Parallel lines at one sigma distance are also visible. A model function of the two variables Gx and dE/dx was also designed and fitted to the 2D histogram. The result is shown in plot (d) (see text).

3.7 REACTION CHANNEL ID

The measured momenta of kaon and electron allow for a full reconstruction of the missing four momentum. The corresponding missing mass spectrum is shown in Fig. 45. Despite inaccuracies in the transfer matrix, mass resolution was sufficient to clearly separate Λ from Σ^0 hyperons. Random background events, identified by two averaged coincidence time side-bands (see fig. 46), and a small amount of kaonic background were subtracted with the appropriate weights. Missing mass cuts were applied to identify both reaction channels as follows: Λ events were assumed to be within (1110MeV, 1140MeV) and Σ^0 within (1185MeV, 1220MeV).

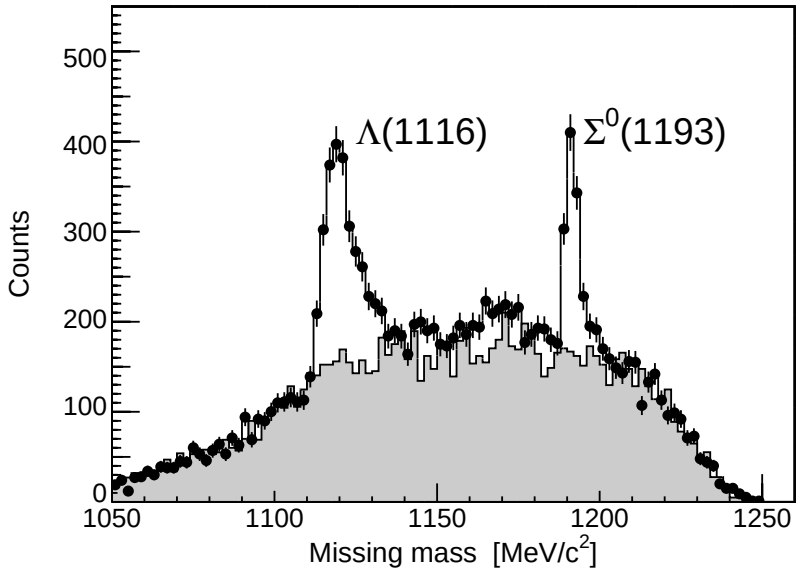

Figure 45: Missing mass spectrum in the $p(e,e'K^+)\Lambda,\Sigma^0$ reaction. The shaded histogram shows the missing mass distribution in two averaged (e',K^+) coincidence time side-bands with the appropriate weights and a small contribution of coincident background. The excess background yield at around 1160–1180 MeV/c^2 was attributed to coincident kaons from outside the spectrometer acceptance that scattered into the detectors.

3.8 SCALING METHOD FOR CROSS-SECTION EXTRACTION AND MONTE CARLO SIMULATION

As is was mentioned in chapter 2, electron detection was not performed by KAOS (as it will in future experiments) but by one of the existing spectrometers in the experimental hall (spectrometer B). Space limitations due to the exit beam line determined a minimum operational angle of 15.5 deg [6]. As Γ is a rapidly varying function of the

6 This was the minimum operational angle ever achieved with spectrometer B, and could only be obtained after several structures in the hall were temporarily removed.

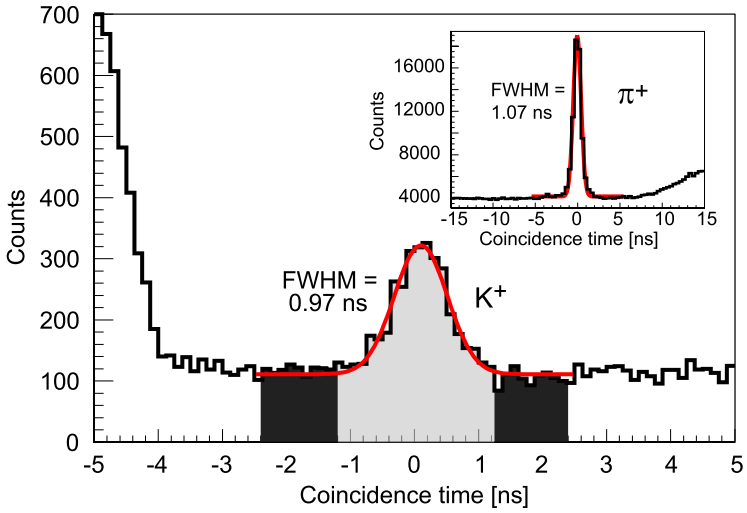

Figure 46: Coincidence time spectra for the $p(e,e'K)$ reaction as well as for the dominant $p(e,e'\pi^+)$ reaction (insert), after corrections for the reconstructed flight path and particle identification cuts. Gaussian distributions on top of a constant background were fitted to the spectra. The width of the (e',π^+) peak is $\Delta t_{FWHM} = 1.07$ ns, the width of the (e',K^+) peak is $\Delta t_{FWHM} = 0.97$ ns. The cut regions for true and random coincidences for selecting kaons are indicated.

electron scattering angle (see eq. 2.96), KAOS measurements in 2008 an 2009 were characterized by a relatively low virtual photon flux. For comparison table 7 shows kinematical settings of previous experiments at low Q^2 (dedicated to hypernuclear production). It can be seen that small detection angles were chosen in all cases for the electron arm, resulting in virtual photon fluxes one order of magnitude larger than for KAOS settings. Since according to eq. 2.6 electroproduction cross sections is directly proportional to Γ, the yield was comparatively smaller.

At the price of including some model dependency, if binning in one particular variable is prefered, the variation of the cross section with respect to the others can be acounted for by an appropriate model, so that all data in the corresponding phase space strip can be used for a single bin. This is of course convenient when the total yield is small. KAOS large angular acceptance sugested kaon center of mass angle as the most interesting variable for data binning. Differential cross-section was then calculated in the center of the acceptance for W and Q^2 as a function of $\cos\theta^*$. The scaling method is explained in what follows:

The general expression for the production yield is:

$$Y = L \times \int \left[\Gamma(Q^2, W) \frac{d^2\sigma}{d\Omega^*} \right] A(d^5V) R(d^5V) dQ^2 dW d\phi_e d\Omega_K^*$$

where the splitting in terms of virtual photon production cross section and photon flux has already been explicitly written. In this expres-

Table 7: Low Q^2 kaon electroproduction experiments

	E94-107	E01-011	E05-115	Mainz 08	Mainz 09
E_γ (GeV)	2.2	1.5	1.5	1.044	1.182
$W(GeV)$	2.2	1.9	1.9	1.67	1.75
$Q^2(GeV/c)^2$	0.07	0.01	0.01	0.05	0.036
E_{beam} (GeV)	~ 4	1.85	2.34	1.50	1.50
P_{e^-} (GeV/c)	~ 1.5	0.35	0.84	0.455	0.318
θ_{e^-}(Deg)	6	3.7-5.7	3-9	15.8	15.5
P_{K^+}(GeV/c)	1.96	1.2	1.2	0.466	0.540
θ_{K^+} (Deg)	6	1-13	1-13	31.5	31.5
$\Gamma(1/e^-/MeV/sr)$	0.02	0.02	0.04	0.005	0.004
Beam current (μA)	100	30	30	0.5	2-4
T. Thick. (mg/cm^2)	~ 100	~ 100	~ 100	~ 300	~ 300

sion L is the experimental luminosity (including global efficiencies such as dead-times and beam-current dependent corrections like the tracking efficiency) and A and W account for acceptance and radiative corrections respectively. Taking out the value of the cross section at the center of the acceptance (CA), the following expression results:

$$Y = L \times \left(\frac{d^2\sigma}{d\Omega^*}\right)_{CA} \times \int \left[\Gamma(Q^2, W) f(Q^2, W)\right] A(d^5V) R(d^5V) dQ^2 dW d\phi_e d\Omega_K^*$$

Where the scaling function f is defined as:

$$f(Q^2, W) = \frac{\frac{d^2\sigma}{d\Omega^*}(Q^2, W)}{\left(\frac{d^2\sigma}{d\Omega^*}\right)_{CA}}$$

According to our binning choice, segmenting the acceptance in small $d(cos\theta^*)$ intervals would allow us to extract the differential cross section as a function of the polar center of mass kaon angle if some reasonable assumption about the form of the function $f(Q^2, W)$ could be devised. With this method, the statistics of the full range of Q^2 and W could be used to compute the cross section at each angular bin. Isobaric models explained in chapter 1 were good candidates for this scaling procedure. Since Q^2 range was relatively small, the prediction of both models showed almost no variation. W was a more sensitive variable since although its range was also relatively small, it just sit in the middle of the resonance region where large variations were expected for small W differences. The decision was taken to use Saclay-Lyon as the model to scale the cross section. As explained above, this makes the measured cross-section slightly model dependent. By comparing to Kaon-Maid model in the same interval (see Fig. 47 for

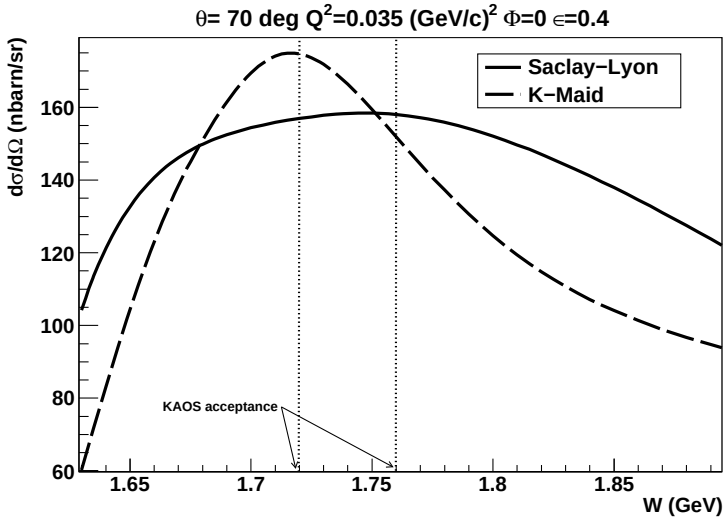

Figure 47: Predictions of Kaon-Maid and Saclay- Lyon isobaric models for the differential virtual photon cross-section as a function of the center of mass energy W. KAOS acceptance is indicated by vertical lines.

an example), it was concluded that the variation was relatively small giving rise to a systematic error sizable in the order of 2%

The measured yield can only be related with the cross section when the generalized acceptance $A(d^5V)$ for each kinematic bin is known. In order to determine this differential acceptance, a very accurate model of KAOS spectrometer including magnetic field, detectors and structural materials along particle trajectories was implemented in a Geant simulation. Kaon decay in flight and scattering was properly accounted for as well. The same tracking trigger paterns, defined by coincidences between F and G paddles used in the experiment, were included as an additional condition in the simulation. This code provided a detection probability for each set of target angles and kaon momentum. When combined with spectrometer B acceptance and after a propper change of variables to $Q^2, W, \epsilon, \phi, \theta^*_K$, the term $A(d^5V)$ could be calculated. The main source of error in this simulation was the overall spectrometer position and the relative positioning of the detectors with accuracies in the order of 1cm. The magnetic map was also a relatively large source of error in the acceptance edges where the calculated trajectories might differ substantially from the physical ones. Finally, inaccuracies in the transfer matrix did also contribute to the gradually increasing differences observed in the outer region of the acceptance.

The agreement between the calculated Λ and Σ^0 kinematic bands and the simulated and experimental acceptance in the p vs θ plane was considered very good ($\sim$ 5 %) in a region defined in Fig. 48.

The corresponding error in spectrometer B was known to be much smaller due to the long experience in its use and the corresponding improvement in its model, tested several times in measurements of well known cross-sections. A contribution to the total systematic error of 1% was assumed.

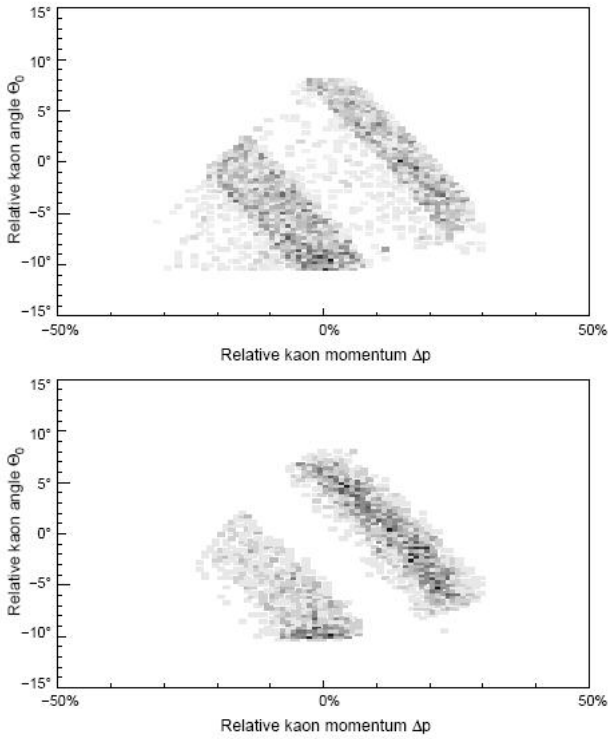

Figure 48: Phase-space for kaon scattering angle vs. kaon momentum in KAOS spectrometer simulated by the Monte Carlo method (top) and measured during the 2009 beam-time (bottom). The kaon data were extracted after particle identification and missing mass cuts. The simulation includes radiative corrections and energy-loss in the target.

Radiative corrections were fully incorporated on the electron arm but no attempt to include them for the charged kaon was done since their contribution was known to be much less significant. This small systematic error is directly related with the tail in the missing mass distribution. A fitted phenomenological model was used to minimize the relevance of this error. Its contribution was estimated in comparison with the effect on the electron arm to be of the order of 1%.

According to the Geant simulation, the products of in flight Kaon decay had a very small probability to be mistaken in the event reconstruction as kaons. The simulation proved that they typically differed by energy deposition and/or time of flight. Tracking trigger also excluded decaying particles out of the angular acceptance defined by paddle combinations. In Fig. 49, detection efficiency is given as a function of momentum for the case where decaying particles are accepted

or not in the cuts applied to the Geant simulation data. It can be readily seen that only a low contamination results from this kind of events. Clearly, for those decaying particles that manage to trigger the data acquisition system the threshold imposed on track quality for data analysis acts as a last strong filter reducing kaon mimicking events to a marginal effect. The dominant inefficiency is due to kaon decay, as can be seen by comparing to the case where decay has been artificially switched of (blue curve). The Kaon survival fraction varied between 0.2 and 0.35 for the range of detected momenta.

3.9 SYSTEMATIC ERRORS

The size of typical corrections to the data and the errors in the cross section associated with those corrections are shown in table 8. The systematic errors are broken into random and scale errors. For example, all of the run-by-run inefficiencies (tracking efficiencies, dead times) are random errors. Scale errors are global errors. An example of a global error is the uncertainty in the current measurement. The

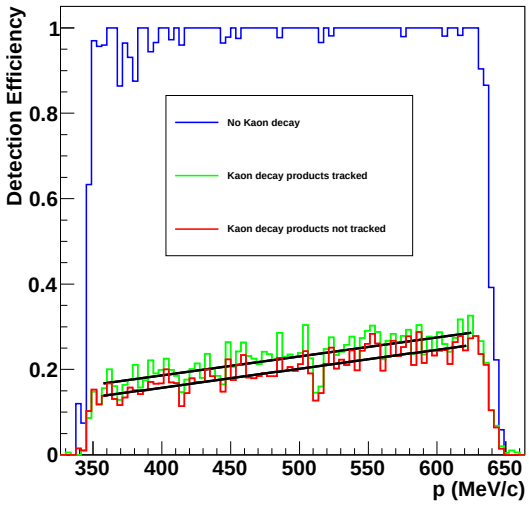

Figure 49: Detection efficiency is presented in this plot as a function of momentum (central track only) for the case where decaying particles are accepted or not in the cuts applied to the Geant simulation data. The unphysical case of non-decaying kaons (Blue) is also shown. From the plot, it is clear that a small fraction of the decaying kaons will be still accepted (although often wrongly reconstructed and rejected by track quality criteria). The largest inefficiency is clearly due to the in-flight kaon decay.

systematic uncertainty assigned to the absolute cross sections is 8 %, and it is dominated by the uncertainties in KAOS acceptance (5 %), MWPC tracking efficiencies (4 %), analysis cut efficiencies (3 %) and scaling model variation (2 %). The beam current was measured on the

1 % level. Other studied sources of systematic uncertainties included kaon survival probability, kaon decay particle misidentification, effective target length and target density fluctuations that introduced a systematic uncertainty on the percent level. These uncertainties are significantly smaller than the statistical uncertainties in the range of 10 to 25 %. Ongoing work is being done to refine these preliminary error values altough only small variations are expected.

Table 8: Systematic corrections and errors in the analysis.

Property	Typical Size	Random Error	Scale Error
KAOS Acceptance			5%
Speck. B Acceptance			1%
Cut Variation(acceptance)		3 %	
Scaling Model	0.9-1.1	0.5 %	2.0 %
Radiative Correction		1 %	1 %
Cut Variation(M_Y)		0.5%	
KAOS tracking Efficiency	0.75-0.90	4 %	
Speck.B Tracking Efficiency	0.9-0.95	1.0%	
KAOS Trigger Efficiency	1.0	0.1 %	
Speck.B Trigger Efficiency	1.0	0.1%	
Coincidence cut efficiency	1.0	0.1%	
TOF β cut efficiency	>0.99	0.5	
Decay Product Kaon Mimic	0.90-0.95	0.05 %	
Target Length/Density			0.4%
Target Density Fluctuation	0.992	0.4%	
Target purity	0.998		0.2%
Charge measurement			1.5%
Random Subtraction	2% to 5%	0.5%	
Total		5.3 %	5.8 %

4

CONCLUSIONS

The effort to understand the universe is one of the very few things that lifts human life a little above the level of farce, and gives it some of the grace of tragedy.

— Steven Weinberg

For the first physical measurement of the KAOS spectrometer, the elementary Λ and Σ^0 electroproduction cross section was chosen. The coincident detection of kaons and electrons allowed the reconstruction of the undetected hyperon mass, and consequently, the identification and separation of the two reaction channels, included in the combined acceptance of the spectrometers tandem. One of the existing spectrometers, B, was used for electron detection at the minimum attainable angle with respect to the electron beam, in order to maximize the virtual photon flux. Two data taking periods were approved for the years 2008 and 2009. Very low photon four momentum values were chosen at Q^2 = 0.03-0.055 $(GeV/c)^2$ with central values $Q^2 = 0.036$ and 0.005 $(GeV/c)^2$, and corresponding degrees of polarization $\epsilon = 0.4$ and $\epsilon = 0.54$. The hadronic system was excited to mean invariant energies of $W = 1.75$ GeV and $W = 1.67$ GeV.

Being Q^2 a measure of photon virtuality, this experiments used almost real photons, although with a relatively large degree of transverse linear polarization. Longitudinal and longitudinal-transverse interference terms are strongly suppressed in the total cross section by the small value of $\epsilon_L = \frac{Q^2}{\omega^2}\epsilon \approx 0.01$. The remaining transverse-transverse interference term does indeed take into account, that this virtual photons are partially linearly polarized, as explained in appendix A. Strictly speaking, then, electroproduction cross section at low Q^2 is not equivalent to unpolarized photoproduction. Experiments with real photons can measure σ_{TT} by combining linearly polarized and unpolarized measurements, since it can be proven that the asymmetry observable defined as $\Sigma = \frac{\sigma_\perp - \sigma_\parallel}{\sigma_\perp + \sigma_\parallel}$ (where $\sigma_\perp(\sigma_\parallel)$ is the differential cross section for the photon polarization normal (parallel) to the production plane) is related with σ_T and σ_{TT} by $\Sigma = \frac{-\sigma_{TT}(Q^2=0)}{\sigma_T(Q^2=0)}$. Isobaric model predictions for $\sigma_{TT}(Q^2 = 0)$ are very close to zero for our kinematics so we consider informative a direct comparison with unpolarized photoproduction results.

As we shall see, this timid departure from photon reality, although far from the "hot" small kaon angle region discussed in Chapter 1, still might hinder important features of the reaction dynamics.

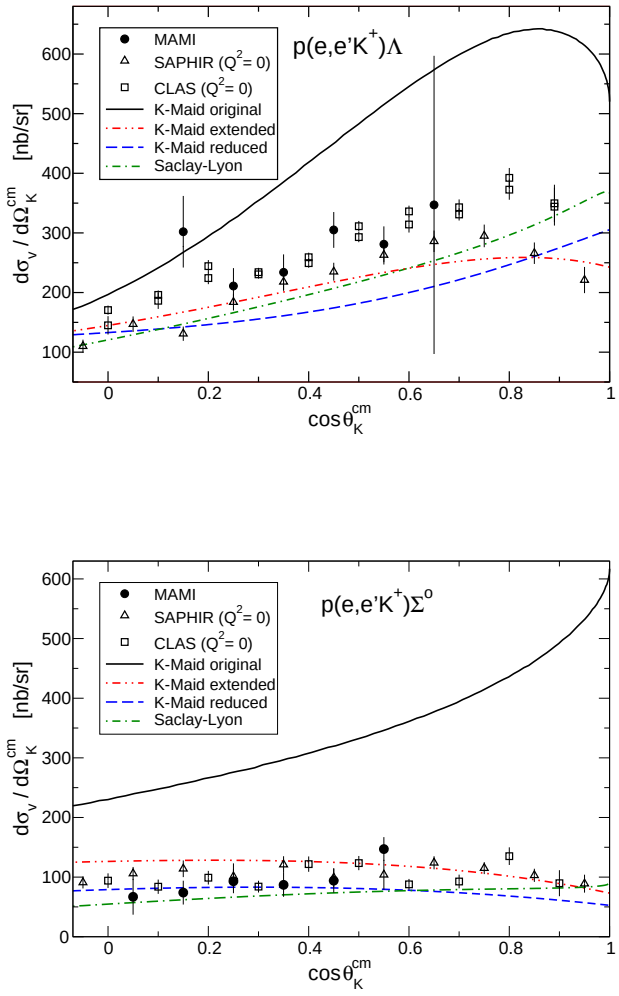

Figure 50: Differential cross sections of kaon electroproduction scaled to the center of the experimental acceptance at $\langle Q^2 \rangle = 0.036\,(\mathrm{GeV/c})^2$, $\langle W \rangle = 1750\,\mathrm{MeV}$ and $\langle \varepsilon \rangle = 0.4$. The MAMI data is compared to variants of the K-Maid model [68] (see appendix A for discussion on the variations) and the Saclay-Lyon model [26]. The model predictions were averaged in Q^2 between 0.030–0.045 $(\mathrm{GeV/c})^2$ and in W between 1740–1760 MeV. The photoproduction cross sections at $Q^2 = 0$ are from the SAPHIR experiment at $W = 1757\,\mathrm{MeV}$ [69] and from the CLAS experiment at $W = 1745$–$1755\,\mathrm{MeV}$ [43, 70]. From [71].

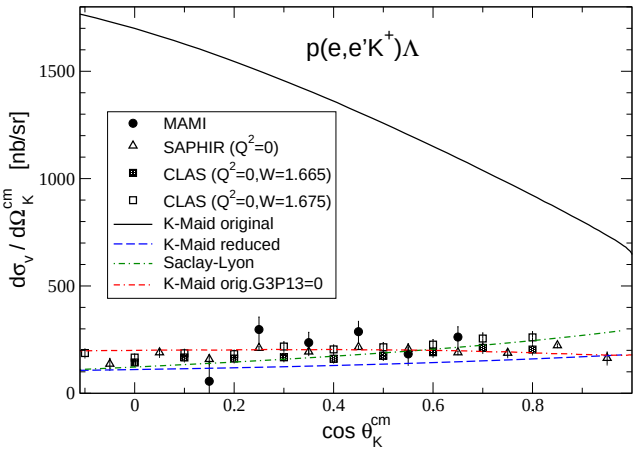

Figure 51: Angular dependence of the total electroproduction cross section for the $K^+\Lambda$ channel at $Q^2 = 0.05$ GeV^2, $W = 1.67$ GeV, and $\epsilon = 0.54$. The original K-Maid, two versions of K-Main reduced, and SL models are shown in comparison with SAPHIR and CLAS data. The latter are shown for two energies 1.665 and 1.675 GeV. An energy dependence is apparent from their relative systematical shift. In the reduced version of KM "K-Maid orig.G3P13=0" only the longitudinal coupling for the N*(1720) resonance was switched off. It can be seen that this makes the main effect of the longitudinal reduction. Behavior of the cross section from the original KM is strange as it has besides the huge magnitude also the opposite angular dependence than the data suggest.

Fig. 50 shows the measured differential cross-sections in angular bins for the two reaction channels. The data was scaled to the center value of the W and Q^2 acceptances by weighting each bin yield with an scaling function $f(Q^2, W)$, defined as the ratio of the predicted Saclay Lyon cross-section and its central value. As explained in chapter 3 this procedure allows the use of the full data sample at each $\cos\theta^*$ bin, at the price of introducing an small model dependence considered as a systematic error. Predictions of three versions of Kaon-Maid and the standard Saclay-Lyon models, explained in chapter 1, are shown for comparison. When compared with photoproduction data from SAPHIR and CLAS collaborations (also included in the plots), a remarkably good agreement is found. The almost flat angular dependence for Σ production and the increasing trend observed for the Λ channel are clearly mimicked by the electroproduction data. The original Kaon-Maid model is excluded with high confidence, describing the other three models the qualitative aspects of the data reasonably well. The reduced Kaon-Maid predicted curve seems to systematically underestimate the actual cross-section for Λ channel, but overestimate it for the Σ channel.

Error bars do not allow to make further statements concerning Saclay Lyon and Kaon-Maid reduced model, since both seem to agree

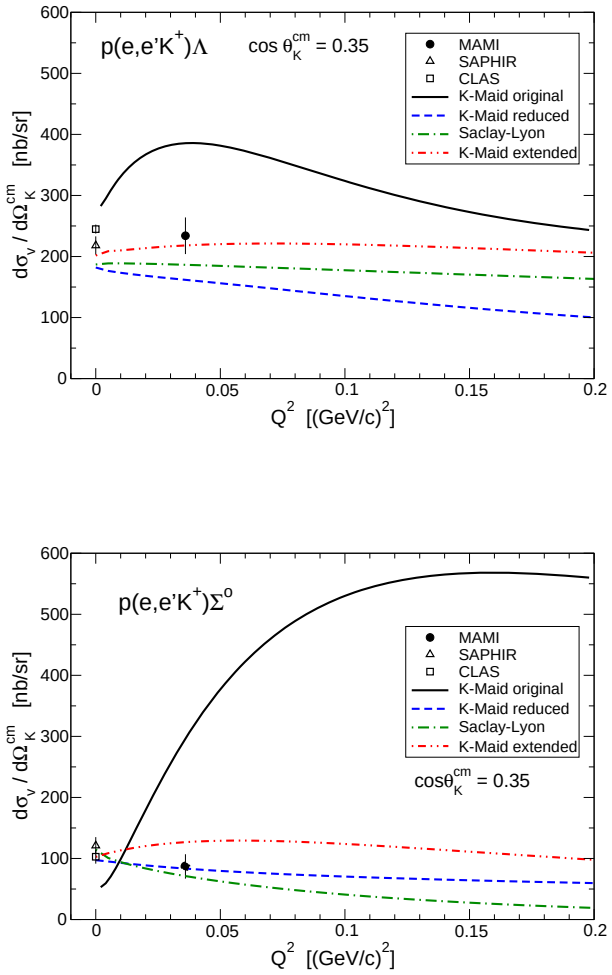

Figure 52: Dependence of the kaon electroproduction cross sections on the virtual photon's four-momentum Q^2. Model predictions and data points are the same as in Fig. 50. From [71].

well with the data. Results for the Λ channel differential cross section, obtained from the lower statistics 2008 data are shown in Fig. 51 together with model predictions. In the reduced version of Kaon-Maid (K-Maid orig.G3P13=0 in the figure), only the longitudinal coupling for the N*(1720) resonance was switched off. It can be seen that this makes the main effect of the longitudinal reduction. SAPHIR and CLAS data are shown for two energies: 1.665 and 1.675 GeV. An energy dependence is apparent from their relative systematical shift. Both data sets confirm that the transition from photoproduction to electroproduction proceeds in both channels smoothly in sharp contrast with the predictions of the original K-Maid model, as can be seen in Figs. 52 and 53, where electroproduction and photoproduction data are shown for a representative angular bin at $\cos\theta^* = 0.35$.

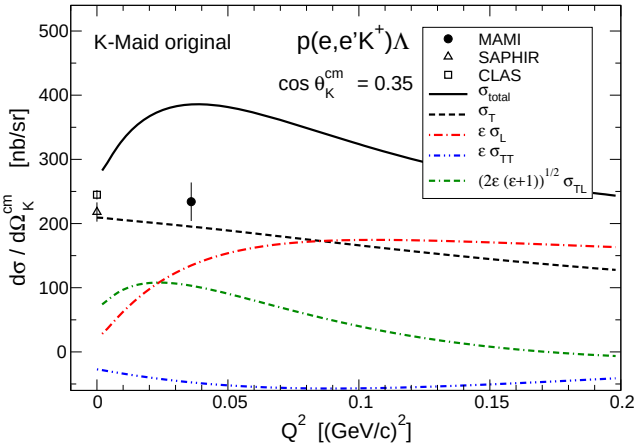

Figure 53: Predictions for the separated and total cross sections in the Λ electroproduction channel from the original K-Maid model for the kinematics probed at MAMI. A strong contribution of longitudinal, σ_L, and transverse-longitudinal interference, σ_{TL}, cross sections is noted. The transverse contribution, σ_T, is slowly decreasing with Q^2. From [71]

In the original Kaon-Maid model, the step rise of the cross-section as a function of Q^2 is specially apparent in Fig.53 at $W = 1.67$ GeV. This is the result of the strong longitudinal coupling to the resonance $P_{13}(1720)$. The data shows that the actual cross section does indeed decrease when entering the virtual photon region. This behavior has been also been documented by CLAS results on the unpolarized cross-section in the $K^+\Lambda$ channel (measured for $0.65 < Q^2 < 2.5$ $(Gev/c)^2$)(see Fig. 54). It is interesting to see that the Q^2 fits to a dipole form $C/(Q^2 + M^2)^2$ (where C is an arbitrary constant) for the K^+ data, significantly overshoot the photon point specially at forward-angles. This can not be explained by a significant contribution to the cross section from σ_L, since CLAS could also measure the separated contributions from σ_L and σ_T, proving that σ_L contribution is rather small. According to Janssen et al. [72], a Q^2 dependence of the kaon and proton form factors might explain the observed behavior. On the other hand, Bydžovský and Mart [36] have demonstrated that the behavior of forward-angle cross sections as a function of the energy for models that include the hadronic form factors is far from realistic. Although no data are available for direct comparison, such a strong damping has not been observed in the experimental data near forward angles. Clearly low Q^2 data is of relevance to clarify this problem.

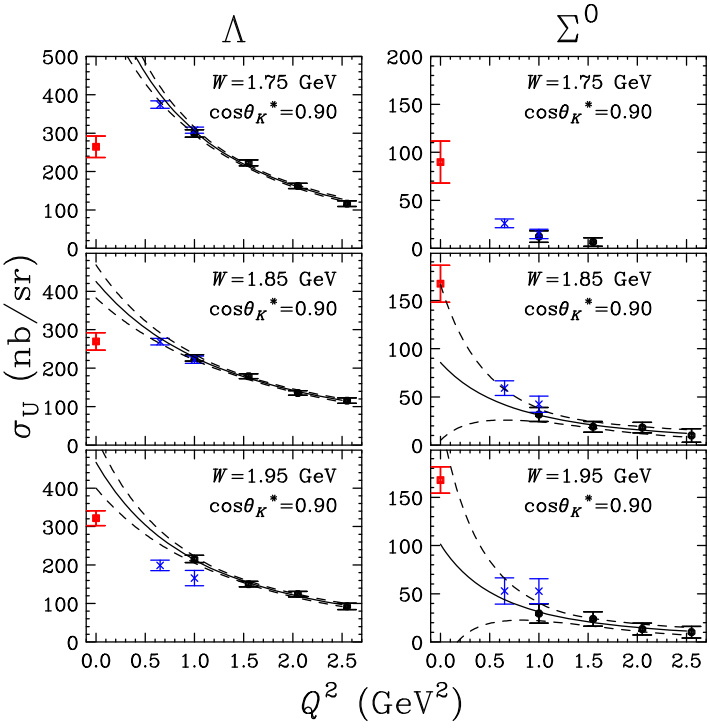

(a)

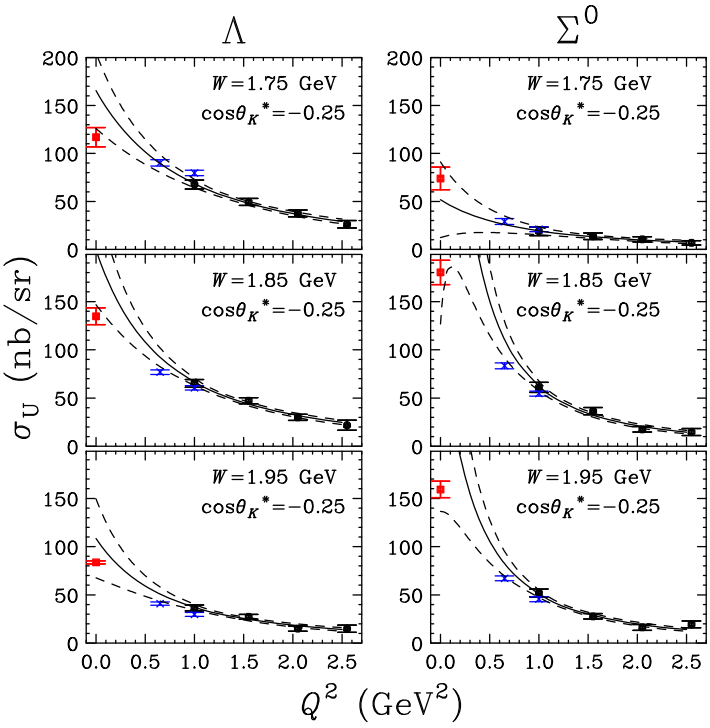

(b)

Figure 54: Q^2 distributions of $\sigma_T + \epsilon\sigma_L$ for the $K^+\Lambda$ and $K^+\Sigma^0$ final states (dark filled circles) at $\cos\theta^*_K = -0.90$ (top) and 0.25 (bottom) for three W points. Solid curves are from a dipole mass fit of the form $C(Q^2 + M^2)^{-2}$. The $Q^2 = 0$ points (solid squares) come from Bradford et al.[73]; two data points from the fit to a different data set (light crosses) are not included in the fits. Dashed lines represent error bands from the fits. From [74]

Part II

FEASIBILITY STUDIES FOR TRACKING DETECTORS

The simultaneous detection of scattered electrons and positive kaons with KAOS at very forward angles is of great theoretical importance and will also permit in the near future spectroscopic studies of hypernuclei [75]. For this program the existing detector system has to be completed with a package for the electron momentum and track reconstruction measuring the coordinate in dispersive direction (vertical sub-detector) and in non-dispersive direction (horizontal sub-detector). Timing and position information will be obtained simultaneously by scintillating fibers [76]. Multi-anode photomultipliers (MaPMT) have been used as read-out devices for the vertical sub-detector. Experience has shown that there are several drawbacks associated with MaPMT. In particular, optical cross-talk among neighboring channels has been observed giving rise to a reduced position resolution. In addition the need for high voltage supplies and magnetic shielding increases the overall price and complexity of the detector. Moreover, a light sensor for the horizontal component of the tracking detector has to be capable of a reliable operation in vacuum. Silicon photmultipliers (SiPM) have been suggested as the read-out device for the horizontal sub-detector of KAOS spectrometer electron arm. In addition the positive arm detector package could also be replaced in the near future by a fiber based detector system.

Silicon photomultipliers are based on a matrix of hundreds of pixels per mm^2 connected in parallel. Each pixel consists of an avalanche photodiode (APD) and a series quench resistor. APDs are operated in a limited Geiger mode a few volts above its breakdown voltage so that each photoelectron gives rise to a Geiger-type discharge with a typical charge gain of 10^6. The avalanche is rapidly interrupted by the built in quench resistor for pixel reactivation. The pixel structure is produced with high uniformity resulting in very small variations in gain. All SiPM pixels work on a common load giving rise to an output signal consisting in the sum of the signals from all pixels. Although each element operates as a binary device the set of all of them can be considered as an analogue detector capable of light intensity measurement. After a few years of R&D, silicon photomultipliers (SiPM) are today an interesting alternative to conventional vacuum phototubes in many applications due to the specific advantages of a solid state device: small size, low voltage operation and magnetic field insensitivity [78, 79, 80]. Nevertheless, the idea of grouping hundreds of miniature avalanche photodiodes in a planar array to form an analog device has found a limitation in the high rate of intrinsic dark pulses (generated by thermally created electron hole-pairs) of such a configuration. Only small active area devices are currently available and typical noise rates are of the order MHz/mm^2 with signal pile-up due to optical cross-talk[1].

1 At the time of submitting this thesis interesting improvements in the technology have reduced noise rates by one order of magnitude and almost eliminated optical cross-talk (see [81]).

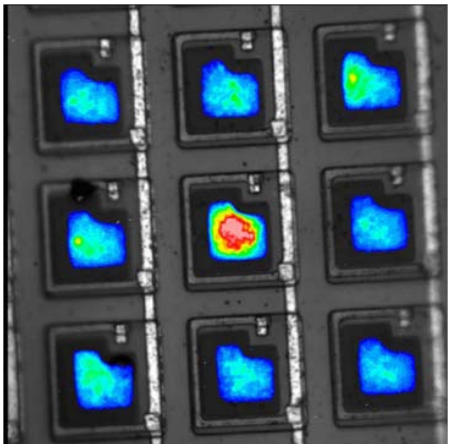

Figure 55: Emission microscope picture of some pixels in the SiPM matrix. A triggered APD is seen in red. Pixel separating tracks result in inactive areas that reduce photon detection efficiency. Aluminum connectors connecting all APDs in parallel are also visible in this picture. From [77]

This leads to the situation of a small photo-sensor that needs to detect a relatively large amount of light in order to achieve an acceptable signal-to-noise ratio. To our knowledge there has been no attempt to use SiPM in applications where only a few photons must be detected. This is for example the situation faced when using scintillating fibres as tracking detectors.

Next chapters will present experimental results on light attenuation, particle detection efficiency and accidental coincidence rates for a prototype set-up.

Since there was little information about radiation hardness of SiPM but clearly an increasing rate of dark pulses as a function of the radiation dose could be expected, making low light level detection difficult, it was considered mandatory to study the impact of the particular kind of radiation the detector will be exposed to on the characteristic parameters that should remain stable for a reliable operation. This was acomplished by the creation of a complete model for multi-photoelectron pulseheight distributions (MPHD) used to extract the main consequences of electromagnetic and hadronic irradiation on SiPM.

The presentation in this second part will be more condensed than in Part I since most of the results presented in the next two chapters have been already published in several papers listed at the beginning of this manuscript. We considered convenient to include at least a resumed version in the thesis since it formed a substantial part of the work developed during this PhD.

5

PROTOTYPING AND EFFICIENCY MEASUREMENTS

5.1 INTRODUCTION

As a first step for studying the feasibility of a tracking detector, based on long and thin scintillating fibers read out by SiPM, an experimental setup was arranged, consisting on a single fiber coupled to SiPMs in both extremes. Technical details concerning detector and fiber characteristics, along with a measurement of breakdown voltage based on signal quantization will be given in the first place. Excitation methods by means of UV laser light and a self triggered radioactive source module allowed precise measurements of light attenuation and detection efficiencies for different threshold levels. Results on photon detection efficiency for each SiPM and accidental coincidence rates as functions of bias voltage are given as well, showing characteristic linear and exponential behaviors, respectively. It is argued that, despite the fast increase in random coincidences, large bias voltages should be used, since most of them are due to single pixel spontaneous activation. Being the corresponding amplitudes small, a sufficiently large increase in threshold level reduces the rate substantially. It will be shown that efficiency is not strongly disturbed, since the number of detected photons is sufficient. A GEANT4 simulation proves that detection efficiencies measured with the Sr radioactive source can mimic minimum ionizing particle results if an appropriate threshold is chosen in the modular unit. Light propagation is modeled to predict detection efficiencies at different excitation points, and compared to data for different quantized threshold levels. Finally, the role of path length dispersion for photon trajectories within the fiber is discussed in the context of signal amplitudes.

5.2 EXPERIMENTAL SET-UP

A set-up for characterizing a 1.5 m long fiber read out in both extremes by SiPM was prepared. The 4.4 mm^2 Photonique device SSPM-0606BG4MM-PCB with typical photon detection efficiencies from 15 to 25 % over the wavelength range 500–650 nm in combination with $2 \times 2\,mm^2$ square, double cladding fibers with an emission peak wavelength at 492 nm from Bicron, type number BCF-20, were considered adequate for the application. Signals were brought into a compact electronic board incorporating a SiPM bias circuit and a trans-impedance amplifier optimized for the amplification of SiPM signals supplied by

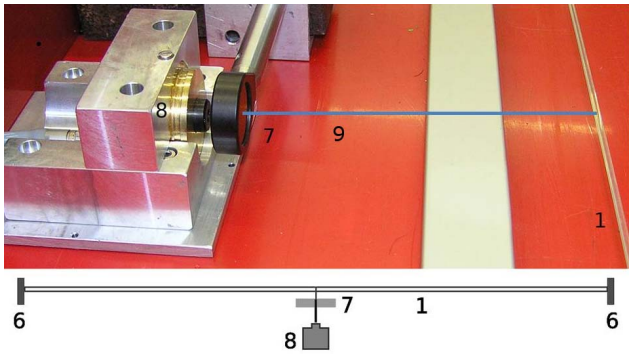

Figure 56: Experimental set-up for SiPM characterization: a fast pulsed (100 ps FWHM) UV laser (8) excited a BCF-20 scintillating fiber (1). Laser light (9) was attenuated by a neutral density filter (7) so that only few photons arrived to the SiPM (6).

the manufacturer of the SiPM (AMP-0611). Amplification factors in a range from 10 to 20 where obtained by varying the supply voltage between 4 V and 10 V. The output impedance was 200 Ω and the signal rise time 700 ps.

No special optical connection between fiber and SiPM was necessary because of the small difference in the refraction indices of the protecting epoxy layer used for the SiPM and the fiber core material. The extremes of the sample fiber where inserted into a slit made in a plastic block in order to obtain a tight junction. Fiber and plastic block were polished with a diamond edge fly cutter as a single unit in order to avoid cladding separation. For the sake of comparison we note that previous tests using a polishing with sand paper and a refinement with diamond paste showed a light yield ~ 7 % lower. A plexiglas connector was designed that allowed a reliable connection and mechanical stability of the full assembly as well as optical control of the relative position of fiber to SiPM for an accurate alignment. A 250 cm long light tight box was constructed to keep the experimental arrangement protected from external light sources. A fast UV laser attenuated by a neutral density filter was used to excite the fiber for calibration purposes, see Fig. 56. A clear peak-like structure could be observed in the charge spectrum, taken with an analog-to-digital converter (ADC), for low laser intensities when a narrow integration window is used, see Fig. 57. The first peak corresponds to the case in which no photons had been detected, the so-called pedestal. The following peaks were due to one, two and more fired pixels. The number of ADC channels between any pair of peaks could be used to calibrate the ADC in terms of number of fired pixels.

Both SiPM in the set-up were characterized by a measurement of the signal gain given by the peak spacing as a function of the bias voltage, V_{bias}, divided by the pre-amplifier gain as shown in Fig. 58. One of the devices showed saturation at around 3 V. The saturation

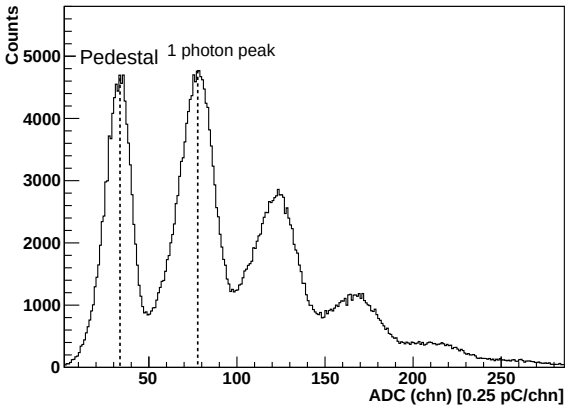

Figure 57: Charge spectrum obtained by UV laser excitation of the scintillating fiber, taken with an analog-to-digital converter (ADC). The first peak corresponds to the pedestal. The following peaks resolve the signals from single and multiple pixels of the SiPM. The peak structure could be obtained for these relatively large area devices by using a narrow integration window. The ADC calibration in terms of number of fired pixels was performed by measuring the distance between the pedestal and the single-pixel peak.

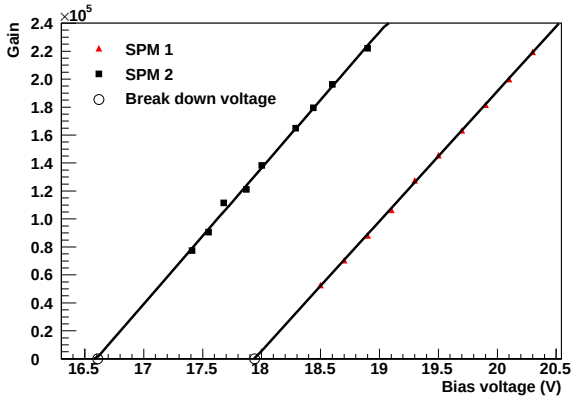

Figure 58: Signal gain computed from the distance between single-pixel peak and pedestal in the ADC spectrum and the pre-amplifier gain as a function of bias voltage for both SiPM in the set-up. The break-down voltage was obtained by extrapolation to zero gain.

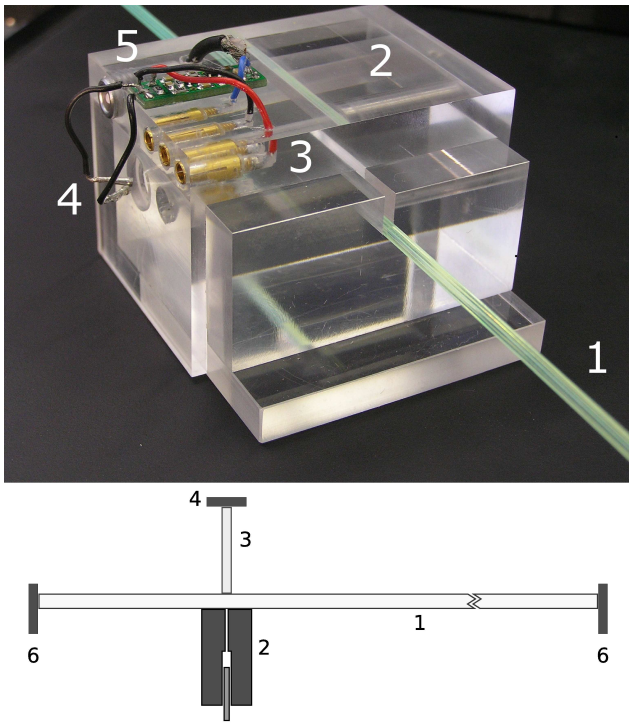

Figure 59: Modular plexiglas device used for measurements of the SiPM/fiber performance. A 1.5 m long green-emitting $2 \times 2\,mm^2$ fiber (1) was placed in a slit and kept in place by the top plexiglas cover. A lead collimator (2) containing a ^{90}Sr β-source with an opening of 0.7 mm was inserted in the central block perpendicular to the square fiber in good alignment with its center. The fraction of electrons that cross the first fiber penetrate a short blue-emitting fiber (3) co-linear with the collimator axis. The signal from this trigger fiber were read out by a blue-sensitivity SiPM (4) and amplified by a trans-impedance integrated amplifier (5). The ratio of coincident signals in left-and-right SiPM (6) to trigger signals (detection efficiency) could be studied for any position along the green fiber axis.

is known to happen at large bias voltages. Extrapolation to zero gain resulted in the break-down voltages, V_{break}. A relatively large difference was obtained for the two Photonique devices: (16.61 ± 0.03) V and (17.94 ± 0.03) V. The different response for large bias voltages above the break-down voltage (overvoltage) and the different break-down voltages most probably are due to manufacturing tolerances. Both SiPM were always operated at the same voltage above break-down to obtain a symmetrical behavior of the detectors. The voltage for the pre-amplifiers and the SiPM was supplied by chemical batteries the voltage of which was scaled down with variable voltage regulators. This method avoided the characteristic ripple of conventional power supplies and resulted in a better peak definition in the ADC spectra. The temperature was measured to be stable within 2 °C.

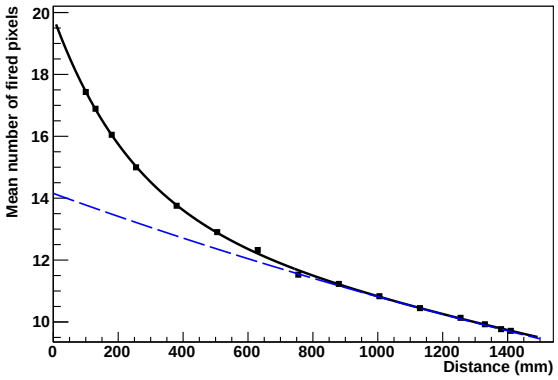

Figure 60: Measurement of light attenuation in a $2 \times 2\,mm^2$ fiber using the experimental set-up shown in Fig. 59. The ADC spectra were calibrated in number of pixels by means of a weak laser excitation of the scintillating fiber. The function $N(x) = N_1 \exp(-x/\Lambda_1) + N_2 \exp(-x/\Lambda_2)$ was fitted to the data, resulting in the two attenuation coefficients $\Lambda_1 = 24\,cm$ and $\Lambda_2 = 402\,cm$. The dashed curve shows the contribution obtained from long distance measurements.

Particle detection efficiency and signal attenuation were measured with a dedicated device consisting of a 3 cm long cylindrical lead collimator with an aperture of 0.7 mm in diameter and containing a ^{90}Sr β-source, see Fig. 59. Electrons were forced to cross the studied fiber perpendicularly by a plexiglas structure with a slit to accommodate the 2 m long fiber. A 2 cm long blue-scintillating fiber was introduced in the plexiglas parallel to the electron trajectory so that those electrons that were able to penetrate the studied fiber entered longitudinally the short one depositing most of their remaining energy there. The relatively large amount of generated photons was detected by a blue-sensitive Photonique device with type number SSPM- 0611B1MM-TO18. The signal amplifier was also located in the plexiglas block so that a very compact device was obtained that could be freely moved along the fiber. Practically no absorption took place in the short trigger fiber and high thresholds for the trigger discriminator could be chosen. The background rate in absence of the exciting source was to all practical purposes zero.

5.3 EXPERIMENTAL RESULTS

Light attenuation was measured by exciting the fiber at several points and by determining the corresponding change in the mean ADC value, that was calibrated in terms of number of pixels. The attenuation curved as shown in Fig. 60 was fitted with a sum of two exponential functions, $N(x) = N_1 \exp(-x/\Lambda_1) + N_2 \exp(-x/\Lambda_2)$, to take into account the different attenuation at short and long distances [82]. There

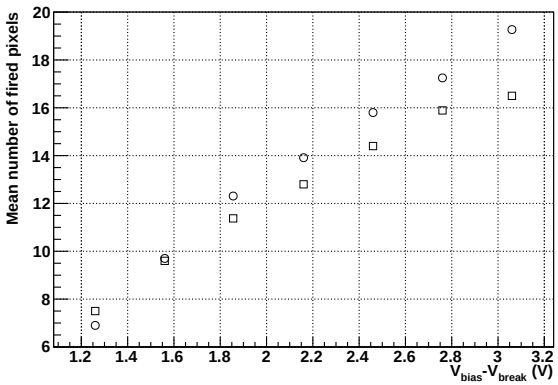

Figure 61: Measurement of the number of fired pixels as a function of overvoltage, $V_{bias} - V_{break}$, for excitation at the central fiber position. One of the devices showed saturation at around 3 V.

is a large difference between the two attenuation coefficients, $\Lambda_1 = 24\,\text{cm}$ and $\Lambda_2 = 402\,\text{cm}$, as a very strong light reduction is observed for short distances. Manufacturers normally only quote the larger coefficient obtained from long distance measurements. It is important to note that much more light is available in the near proximity to the detector.

The particle detection efficiency was defined as the ratio of the number of left-and-right coincidence signals to trigger signals. The efficiency was studied as a function of the threshold level in units of single pixel signals for different bias voltages. The dependence of the efficiency on the operating parameters was most directly seen in the variations of the number of fired SiPM pixels, a measure of the detected light yield. Fig. 61 shows a measurement of the light yield as a function of the overvoltage when the fiber was excited in the central position. The largest operating voltages correspond to a maximum PDE. The accidental coincidence rate, R_{acc}, was measured at a threshold of 1.5 pixels as function of the overvoltage, see Fig. 62. Despite the exponential increase of the accidental coincidence rate with increasing bias voltage a change of only one unit in the threshold level results in a drastic reduction of the rate. A compilation of the results is shown in Table 9.

Given the above results, the optimum operation parameters depend on the characteristics of the system, namely the true coincidence rate, R_{true}, the application of an external trigger or not, and in case any accidental signal generates a trigger also the inherent dead-time of the data acquisition system.

A fiber detector system that is externally triggered, like in a laboratory set-up as described, the ratio of detected true coincidences to the sum of true and accidental coincidences, $R = \varepsilon R_{true}/(R_{true} + R_{acc})$, is a figure-of-merit, *FOM*, generally adequate for many practical problems. If the detector itself triggers the data acquisition, and the dead-

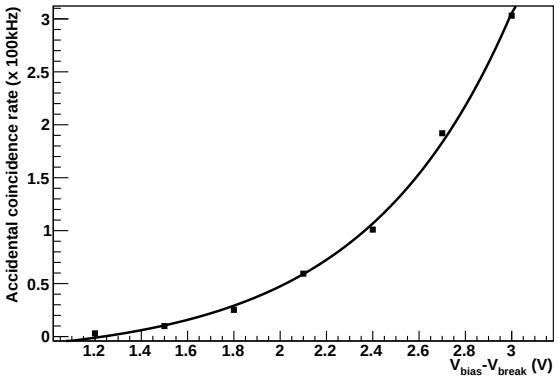

Figure 62: Measurement of the accidental coincidence rate for a threshold of 1.5 pixels as a function of overvoltage, $V_{bias} - V_{break}$, for excitation at the central fiber position. Despite the observed characteristic exponential behavior SiPM should be operated at high bias voltages for a good detection efficiency.

Table 9: Measured detection efficiencies, ε, and accidental coincidence rates, R_{acc}, for different threshold amplitudes, N_{thr}, and SiPM overvoltages, $V_{bias} - V_{break}$, for excitation at the central fiber position. Two figure-of-merits, *FOM*, are reported for the operation parameters that show the general trend to use high overvoltages and high thresholds. Definitions of the *FOM* are given in the text.

Overvoltage (V)	2				3			
N_{thr} (pixels)	1.5	2.5	3.5	4.5	1.5	2.5	3.5	4.5
ε (%)	97	85	77	64	> 99.9	99.6	95	86
R_{acc} (kHz)	19.7	0.23	10^{-3}	$< 10^{-3}$	300	3.4	0.09	0.004
R (*FOM*)	0.05	0.69	0.77	0.64	0.003	0.23	0.87	0.86
R_{DAQ} (*FOM*)	0.33	0.79	0.72	0.60	0.03	0.69	0.86	0.79

time, τ, corresponds to the time the whole system (not necessarily the fiber detector) is insensitive or paralysed, the observed rate of detected true coincidences to the number of detector output signals is relevant:

$$R_{DAQ} = \frac{\varepsilon R_{true} + R_{acc}}{(R_{true} + R_{acc})(1 + \tau(\varepsilon R_{true} + R_{acc}))} .$$

In Table 9 the numbers for these two *FOM* are shown using the conservative values of $\tau = 0.1$ ms and $R_{acc} = 1$ kHz applicable to the laboratory measurements. The high numbers at large overvoltages and high threshold amplitudes follow a general trend independent of the specific system parameters. For the laboratory set-up a detection efficiency of 95 % at an accidental coincidence rate of 87 Hz was the optimum value achieved at a threshold of $N_{thr} = 3.5$ pixels and an overvoltage of $V_{bias} - V_{break} = 3$ V. For the application of such a

detector in a spectrometer much higher particle rates of the order of MHz with much smaller dead-times of the front-end electronics and data acquisition system should be considered. In general it is recommended to operate at high overvoltages for the highest efficiency and to reduce the accidental coincidence rate by an increase in the threshold level to acceptable values.

5.4 DETECTION EFFICIENCIES FOR HIGHLY RELATIVISTIC ELECTRONS

The obtained results from the efficiency measurement with a ^{90}Sr β-source have to be converted to an expected efficiency valid for the real experimental conditions where highly relativistic electrons of typically 400 MeV energy must be detected. ^{90}Sr emits electrons with a maximum kinetic energy of $E_{max} = 546$ keV. It decays to ^{90}Y with a half-life of 29.12 years. The β-decay of the short-lived daughter has a much higher end point, $E_{max} = 2.28$ MeV, and a mean energy of $\langle E \rangle = 933$ keV. GEANT4 was used to simulate the tracks and energy deposition of the β-electrons from the collimated ^{90}Sr source in the sample and trigger fibers. Only the energy spectrum from the ^{90}Y component was modeled including phase-space factor and Fermi function correction as the results for the end point electrons of the Sr decay showed straggling paths that could not reach the trigger fiber. Electrons from the high energy tail of the ^{90}Y decay suffer smaller deflections.

The question arises of whether a threshold value can be chosen for the trigger detector resulting in an average energy deposition in the studied fiber as close as possible to that of highly relativistic electrons. Fig. 63 shows the mean energy deposition in the 2 mm thick fiber as a function of the energy threshold level required in the trigger detector. The blue dashed line shows the energy deposition for 400 MeV electrons ($\Delta E = 366$ keV). The root mean square deviation from the mean (*RMS*) of the corresponding distributions are represented by the vertical lines. A threshold level of $\Delta E_{thr} = 800$ keV allowed a precise emulation of the realistic working conditions with both distributions differing only slightly in their *RMS* values. The comparison of the count rate at the chosen energy threshold to the total rate allows for a practical determination of the corresponding voltage level in a leading edge discriminator. A trigger rate of 20 Hz remained for the chosen threshold.

5.5 MODELING OF LONG SCINTILLATING FIBERS READ OUT BY SIPM

An estimation of the detection efficiency for a given threshold can be obtained by multiplying the triggering probabilities of both SiPM. It is useful to use the single pixel amplitude as a threshold unit due to the

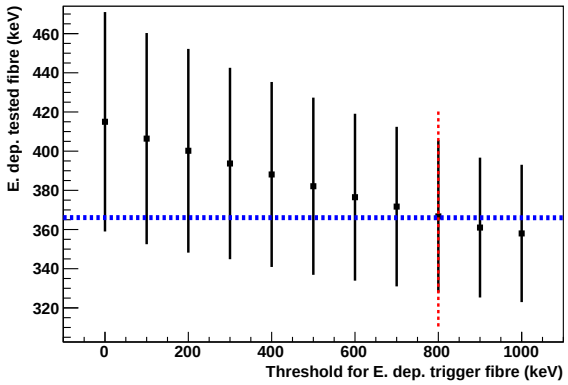

Figure 63: Results of a GEANT simulation for the average energy deposition in the studied fiber as a function of the energy threshold demanded in the trigger detector. Vertical lines represent the *RMS* of the energy distribution in the fiber (not the error of the mean value). The dotted lines show the energy deposition for 400 MeV electrons: $\Delta E = 366\,\text{keV}$ and $\sigma = 110\,\text{keV}$. A threshold of $\Delta E_{thr} = 800\,\text{keV}$ provided the same mean energy deposition (with $\sigma = 77.7$) at a trigger rate of 7 % of the total rate. A deviation in the energy deposition between laboratory set-up and relativistic electrons as large as 12 % is possible for low trigger thresholds.

intrinsic quantization of the SiPM signals. Using Poisson distribution normalization one can write the detection efficiency in terms of finite sums:

$$\varepsilon(N, x, v) = \left(1 - \sum_{n=0}^{N} \frac{\lambda_1(x,v)^n e^{-\lambda_1(x,v)}}{n!}\right)\left(1 - \sum_{n'=0}^{N} \frac{\lambda_2(x,v)^{n'} e^{-\lambda_2(x,v)}}{n'!}\right)$$

where N is the threshold level, and the mean number of detected photons in each detector, λ, is made explicitly dependent on the position along the fiber, x, and the bias voltage, v. If pile-up of dark pulses is neglected only optical cross-talk can bring noise signals to amplitudes beyond one pixel.

A simple model based on the voltage dependent probability, q, of single neighbor activation allows the probabilities for the formation of different clusters of APD to be calculated analytically. Based on this model a Monte Carlo calculation of the fiber and SiPM characteristics was used to predict the accidental coincidence rates for different detector geometries. This model is described in detail in Ref. [83] and explained in sec. 6.5. It uses as an input parameter the value $q = 0.028$ extracted from the fit to the ADC spectrum of the Photonique device SSPM-0701BG-TO18 operated at the manufacturer recommended bias voltage of 17.9 V (2.5 V over the break-down voltage) under low light level illumination. The mean number of detected photons per mm fiber thickness, $\lambda = 7$, was extracted from the measurement with a 0.85 mm diameter fiber that was excited by a ^{90}Sr source. The corresponding

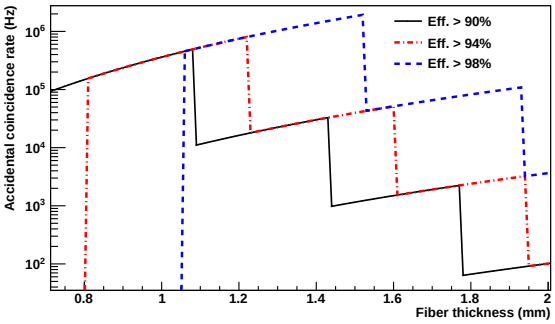

Figure 64: Numerical calculation of the accidental coincidence rate vs. fiber thickness, for matching detector area, when a detection efficiency larger than 90 % (full line), 94 % (dashed-dotted line), and 98 % (dashed line) is demanded. A quadratic increase in the rate proportional to the active area of the SiPM can be observed before a light level is reached where the threshold can be increased by one unit (single pixel amplitude) reducing abruptly the noise rate. For a given detection efficiency a minimum fiber thickness is necessary.

zero pixel cross-talk probability, $P(0) = \exp(-\lambda)$, was calculated by considering the number of events in the pedestal. This value was compatible with the one measured with a square fiber of $4\,mm^2$ cross-section. It is important to stress that in general the number of fired pixels does not follow a Poisson distribution due to optical cross-talk and after-pulsing. Nevertheless, the mean number of detected photons is correctly calculated with this expression as these effects only appear when at least one pixel has been fired.

Fig. 64 shows the calculated accidental coincidence rate as a function of fiber thickness assuming a matching area for the SiPM when a detection efficiency higher than 90 %, 94 %, and 98 % is required. It is seen that after each sharp drop of the noise level, when an increase of one unit in the threshold is achieved, there is a region in which the rate increases quadratically as the SiPM area does. Despite the fast increase in the accidental coincidence rate it is apparent that an adequate fiber thickness will result in an almost silent detector. A similar behavior appears when the bias voltage is increased: the PDE increases linearly while the dark count rate shows an exponential dependency, compare to Figs. 58 and 62 for an experimental measurement of these quantities. In addition, the optical cross-talk probability also will rise linearly. The steps are consequently less pronounced. One should conclude, that when signal pile-up can be neglected higher voltages are preferred for high efficiencies.

One needs to consider that path length dispersion and the decay time of the emitted photons reduce the effective pulse height and will have an effect on the efficiency for a detector based on long scintillating fibers. The spread of propagation times is given for a fiber of length L and refractive index n by $\Delta t_{prop} = (Ln/c)(1/\cos\theta_{max} - 1)$

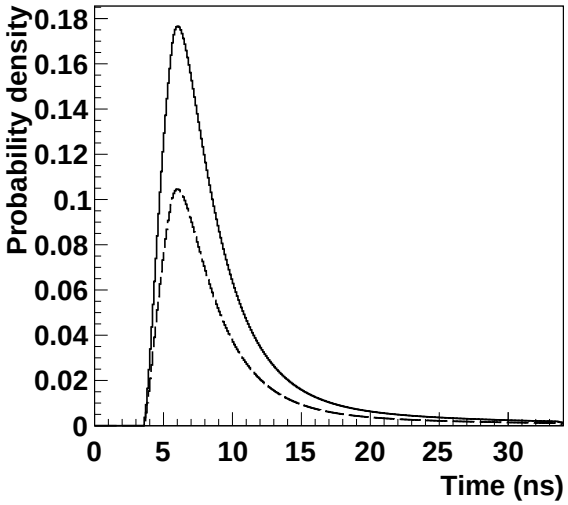

Figure 65: Result of a numerical convolution of the propagation time distribution and scintillator decay curve (solid line) for $x = 135\,\mathrm{cm}$. The time dispersion is reduced due to the stronger attenuation along helical photon paths when the light absorption is included in the model (dashed line).

for the minimum and maximum propagation times, $t_{min} = Ln/c$ and $t_{max} = (Ln/c)(1/\cos\theta_{max})$, where θ_{max} is the critical angle for total internal reflection. The probability density function of the propagation times of photons, $dN/(Ndt)$, produced by an event at $t = 0$, can be calculated from the angular distribution of photons inside the scintillator, $dN = 2\pi d\cos\theta$. It follows that $dN/dt = -2\pi Ln/(ct^2)$ and $N = \int_{t_{min}}^{t_{max}}(dN/dt)dt' = 2\pi(\cos\theta_{max} - 1)$. Finally, the probability density for the arrival times at the SiPM active area due to path length variations is $P_{prop}(t) = dN/(Ndt) = (Ln/ct^2)(1/(\cos\theta_{max} - 1))$. The arrival time probability density function for a realistic scintillator can be folded in as follows: $P(t) = \int_0^\infty I(t')P_{prop}(t - t')P_\Lambda(t - t')dt'$, where $P_\Lambda(t) = \exp(-ct/(n\Lambda))$ is survival probability depending on the average bulk absorption coefficient, Λ, in the material. The distribution of decay times of light emitting states, $I(t')$, is included with a light pulse shape of exponential form with a decay time of $\tau = 2.7\,\mathrm{ns}$. The probability density function of the transit time spread of electrons in the SiPM is not relevant since SiPM have excellent timing capabilities ($\Delta t \approx 50\,\mathrm{ps}$).

Based on the experimentally measured absorption curve, Fig. 60, an estimation of the bulk absorption lengths was obtained by solving numerically for the proportionality factor, k, the following equation:

$$N(x) = \int_{t_{min}}^{t_{max}} dt \frac{xn}{ct^2} \frac{1}{1 - \cos\theta_{max}} \left(N_1 \exp(-\frac{ct}{nk\Lambda_1}) + N_2 \exp(-\frac{ct}{nk\Lambda_2}) \right)$$

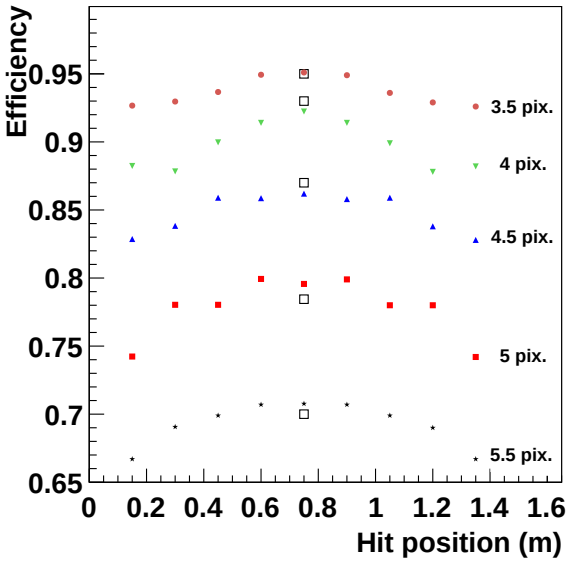

Figure 66: Result of the Monte Carlo simulation on detection efficiency as a function of threshold level and hit position. The results from the measurements at the central position were superimposed and are in good agreement.

where $N(x)$ is the number of detected photons at distance x and Λ_1, Λ_2, N_1 and N_2 are the parameters from the double exponential fit to the experimental points. The factor k corrects the fitted values Λ_1 and Λ_2, to provide the bulk absorption lengths as these parameters are linked to the average photon path length from the excitation point to the SiPM and not to the actual distance between them. Fig. 65 shows the resulting arrival time distribution with and without absorption. Being the dispersion comparable with the typical pulse width perfect pile-up of the signals will not be achieved resulting in an effective signal amplitude reduction.

Finally, Fig. 66 shows the result of the Monte Carlo simulation for the efficiency as a function of the position along a 1.5 m long fiber for different threshold values. The calculation shows that the relative variation of detector efficiency between center and extremes is an increasing function of the threshold value. The results from the measurements at the central position were superimposed and are in good agreement.

6

NOISE AND RADIATION DAMAGE IN SILICON PHOTOMULTIPLIERS EXPOSED TO ELECTROMAGNETIC AND HADRONIC RADIATION

6.1 INTRODUCTION

Solid state particle detectors are often exposed to high radiation doses. It is well known that generating centers are created during irradiation which increase the leakage current [84]. The bulk leakage current is multiplied in avalanche photodiodes (APD) by the gain factor and the resulting pulses are undistinguishable from photon generated events. Consequently, an increasing rate of dark pulses as a function of the radiation dose is seen in SiPM [85]. Adverse effects of irradiation on other characteristic parameters of SiPM such as gain uniformity, after-pulsing or optical cross-talk probability would be also detrimental for a detector.

When operated as a double spectrometer KAOS detectors will be located in close proximity to the electron beam [86]. In addition to a broad neutron spectrum high electromagnetic background levels are expected at the SiPM locations. Sophisticated trigger logic implemented in FPGAs will be used to minimize background disturbance but radiation hardness of the photon detectors is still an open issue. It is consequently imperative to study how operative parameters of SiPM can be affected in different radiation environments. A Monte Carlo simulation containing the most relevant operational parameters can be used to extract the impact of irradiation on the SiPM performance [83]. Photonique devices with an active area of $1\,mm^2$ composed of 500 APD have been irradiated directly by a 14 MeV electron beam and indirectly by placing them in close proximity to the beam-line. Shielding effects and annealing have also been investigated. The results will be presented in the following Sections.

6.2 SIPM CHARACTERIZATION

The SiPM photon counting capabilities are a consequence of the narrow response function. Two factors contribute to this fact. First the single pixel signal has a well defined amplitude due to the low excess noise factor (smaller than 1.1 for the studied SiPMs) and second the variation from pixel to pixel of that amplitude is small as a result of the fabrication process. Low light level detection is thus characterized by a multi-photoelectron pulse-height distribution (MPHD) with very clear

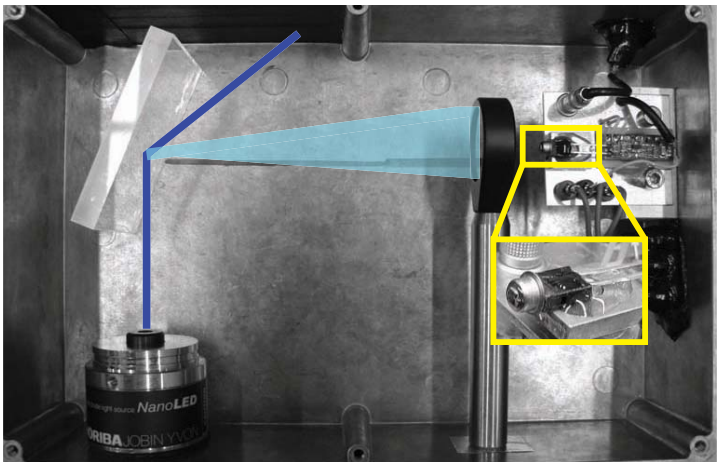

Figure 67: Experimental set-up for SiPM characterization: a fast pulsed UV laser (100 ps FWHM) excited a BC-408 plastic scintillator. Reflected UV light was absorbed in a black screen. The blue scintillation light was attenuated by a neutral density filter so that only few photons arrived to the SiPM (inset right).

peaks corresponding to the different number of activated pixels and a photon detection efficiency (PDE). It is revealing to measure with an analogue-to-digital converter (ADC) the output signal charge for a randomly generated integration window in the absence of light. SiPM characteristics such as optical cross-talk, after-pulsing and dark count rate have a direct impact on this ADC spectrum. These contributions explain the departure of the MPHD from a Poissonian distribution. Experience has shown that irradiation effects are readily observed in this spectra and Monte Carlo simulations are an appropriate tool to extract any change in SiPM working parameters. For example any increase in dark count rate will change the relative amplitude of the pedestal peak by populating the one or more pixel peaks.

A complete SiPM characterization was performed by measuring ADC spectra under low illumination levels and in addition in darkness with a randomly generated 30 ns wide window being the mean width of the single-pixel signal 9 ns. The low light level detection under reproducible conditions was realized by exciting a BC-408 plastic scintillator ($80 \times 50 \times 10$ mm^3) with a fast pulsed UV laser (100 ps FWHM). The measuring system can be seen in Fig. 67. Reflected UV light was absorbed in a black screen and the blue scintillation light was attenuated by a neutral density filter. The laser intensity could be regulated so that only few photons arrived to the SiPM.

6.3 SIPM IRRADIATION WITH THE ELECTRON BEAM

Controlled radiation dose studies are important in order to provide precise quantitative information about SiPM radiation hardness. Stage A of MAMI provides a high quality beam of 14 MeV electrons. We

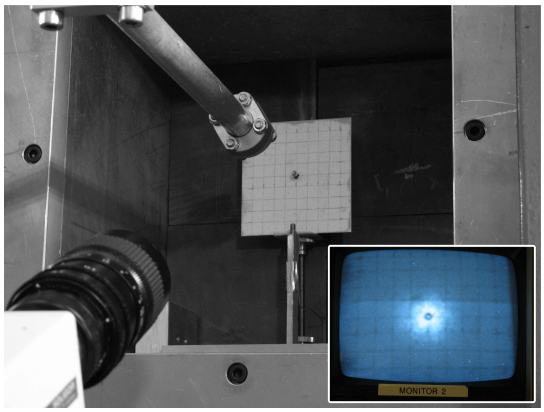

Figure 68: Experimental set-up for SiPM irradiation. 14 MeV electrons left the evacuated beam-pipe through a 0.3 mm aluminum window. Multiple Coulomb scattering of the beam generated a wide spot on the fluorescent screen. The beam position could be accurately steered so that the SiPM was at the centre of the spot as can be seen in the on-line monitor picture (inset lower-right). The small SiPM active area was considered as uniformly irradiated.

irradiated a sample of SSPM-0701BG-TO18 SiPM with a beam current of 10 nA. The electrons crossed a 0.3 mm thick aluminum window at 15 cm distance from the 1 mm^2 active area of the SiPM. Fluences on the SiPM were calculated taking into account multiple Coulomb scattering in the thin exit window and ranged from 3.1×10^9 to 3.8×10^{10} electrons/mm^2. For comparison with similar studies performed with other radiation sources and energies we quote the non-ionizing energy loss (NIEL) of 14 MeV electrons when crossing the SiPM active area being 1.1×10^{-4} MeV cm^2/g [87, 88]. Heat dissipation and damage on the transparent epoxy layer protecting the silicon material were also calculated and was proved to be negligible (less than 5% for the full integrated dose). Grounding of the SiPM was provided in order to avoid damage by the sudden release of accumulated charge. Fig. 68 shows the experimental set-up. The beam position was monitored with a fluorescent screen during the SiPM irradiation.

Fig.69 shows MPHD for the green sensitive Photonique SiPM (40% PDE at 560 nm) before and after irradiation for a fixed light intensity for the same operating voltage. Pedestal shift is a consequence of the increase in leakage current. Electron hole pairs generated in the active detector volume will give rise to a full pixel signal undistinguishable from photon generated pulses. The large increase of this type of events after irradiation results in signal pile up with the corresponding shift in the pedestal position. Pedestal shift has not been corrected as this effect is informative to the reader concerning the order of magnitude of dark count rate and can give rise to specific problems in particular applications.

For higher fluences the increase in noise rate is so large that a multi-pixel peak differentiation is no longer possible in the ADC spectrum.

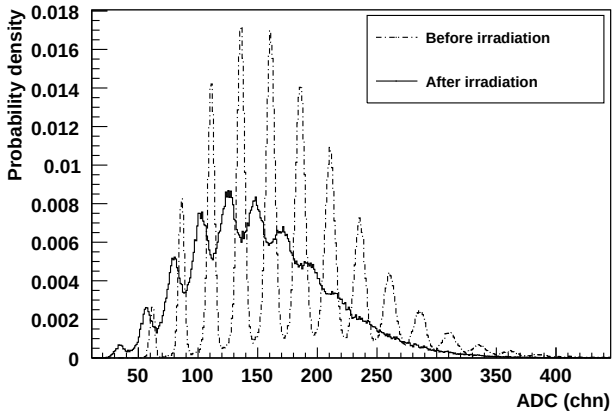

Figure 69: ADC spectra for low amplitude signals from green sensitive Photonique SiPM before and after irradiation with 3.1×10^9 electrons/mm^2.

The detectors were still able to operate giving an output signal proportional to number of incoming photons (within the dynamical range) but the signal-to-noise ratio was considerably worse for low light levels. The variation in the integrated pulse charge was studied by comparing the position of the maximum in the ADC spectra for large signals. The noise contribution to such a spectrum are considered irrelevant.

The result of such an investigation is shown in Fig. 70. A progressive reduction of the integrated charge was observed. This fact can be attributed to the loss of a progressively larger amount of pixels which remain permanently in the off-state, to the reduction in the PDE of each pixel, to a reduction in the single pixel amplitude or gain variation due to reduced bias voltage as a consequence of the larger voltage drop in the series resistor for increased leakage current. A combination of these factors is equally possible. This histograms are a demonstration of the kind of problematic that high radiation dose will cause in ADC spectra. No attempt is made to disentangle the different effects involved.

6.4 SIPM IRRADIATION BY HADRONIC AND ELECTROMAGNETIC BACKGROUND

In a second step a more realistic situation was arranged by placing the SiPMs in the experimental area close to where the actual detector will be located. A precise knowledge of the radiation field in the experimental hall for a future SiPM detector set-up is not available, as it happens to be strongly dependent on the experimental condition. As the radiation damage predictions based on the electron irradiation data (scaled appropriately) can only be approximate, it is consequently important to study the effect of the heterogeneous radiation present

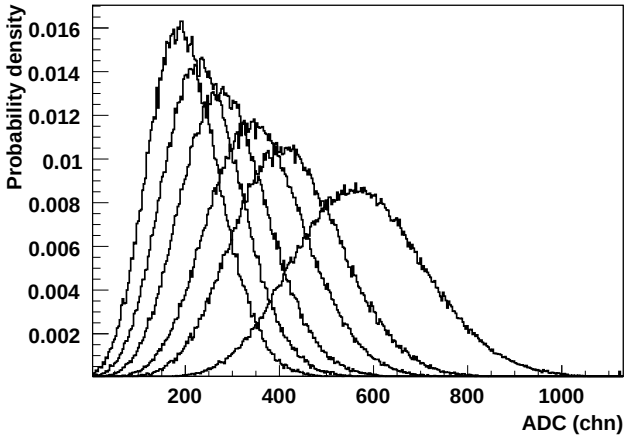

Figure 70: ADC spectra for fixed laser intensity after irradiation with 30.8, 77.0, 123, 185, 262 and 385 $\times$ 10^8 electrons. A progressive reduction of the photon detection efficiency or of the SiPM gain is suggested as an explanation for the observation of lower integrated charge with increased irradiation dose.

at the planned detector position on the SiPM performance. The blue sensitivity Photonique device SSPM-0611B1MM (16% PDE at 410 nm) was added to the sample in order to investigate possible radiation hardness differences. Noise spectra were taken for Photonique SSPM-0701BG-TO18 devices before irradiation and after 3 and 7 days of normal operation with typical electron beam currents of 10 µA on a carbon target in the experimental hall.

The electromagnetic component of the radiation field at the SiPM location was estimated by means of a digital dosimeter giving an average value of 30 mSv per day of exposure. At this relatively low level measurable effects on the SiPM due to photons or electrons will show up only after several months of exposure. Short term damage is mainly due to the large hadronic component present in the beam-dump proximity as a consequence of their much higher NIEL. High energy neutrons are particularly dangerous due to their long range in air and the practical impossibility to provide effective shielding for them. Thermal neutrons can be easily stopped by borated polyethylene (BPE) for example. Nuclear capture of such thermal neutrons frequently results in the production of photons, that can be accounted for by a few mm of lead shielding. One of the SiPM was shielded by 3 cm of BPE and 2 mm of lead. The amount of shielding used was compatible with the space available for the actual tracking detector.

The results are shown in Fig. 71. A large increase in the number of one pixel pulses as compared to the pedestal peak is observed after irradiation. For a randomly generated integration window this can be directly interpreted as an increase in the dark pulse rate. The variation found in the relative populations of the second and third peaks corresponding to one and two pixels before and after irradiation are a

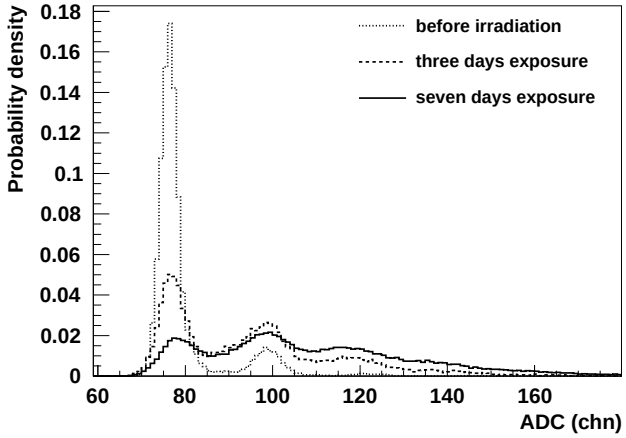

Figure 71: Noise spectra of a green sensitive Photonique SSPM-0701BG-TO18 device that was exposed to background irradiation close to the beam-line during one week of normal beam operation. Damage is shown for 3 and 7 days of exposure.

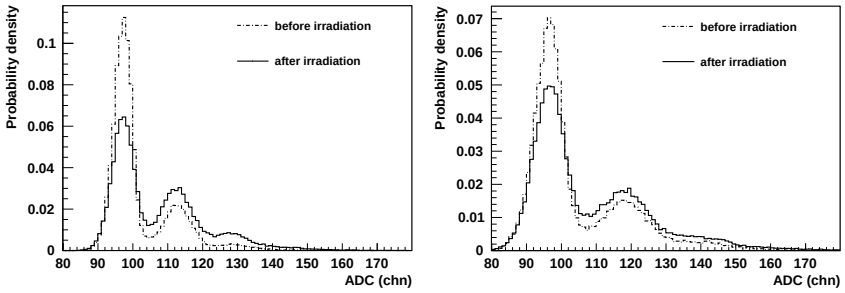

(a) without radiation shielding (b) with radiation shielding

Figure 72: (a) Noise spectra of blue sensitive Photonique SSPM-0611B1MM devices before and after irradiation close to the beam-line. (b) Same type of SiPM but protected by a radiation shield. A reduced damage is observed for the shielded SiPM.

consequence of an increase in the after-pulsing probability according to the Monte Carlo simulation.

Blue sensitive Photonique SSPM-0611B1MM devices were exposed to half of the full dose and the noise spectra with and without shielding are shown in Fig. 72. The shielding effect is clear but damage due to high energy neutrons is still observable. The device SSPM-0611B1MM seems to present a smaller damage than the green sensitive SiPM SSPM-0701BG-TO18 for the same irradiation period of 3 days.

A heat treatment (annealing) was attempted to reduce the observed damage. SiPMs were kept in a controlled temperature oven at 80° during two weeks. ADC spectrum for a randomly generated window is shown in Fig.73 for the green sensitivity device. Pedestal shifts have been subtracted for easer comparison. Only a partial recovery can be

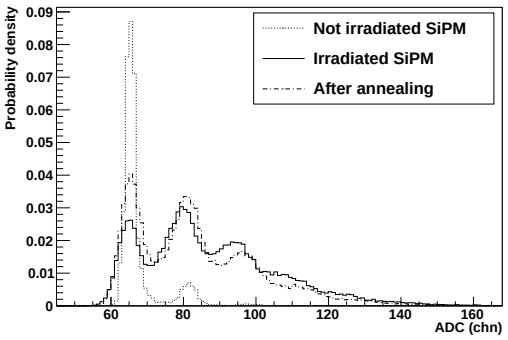

Figure 73: Annealing at 80° results only in partial recovery of the SiPM exposed to the radiation field in the experimental hall. Green sensitivity SiPM histograms are shown before and after irradiation for a randomly generated integration window. The same histogram is shown after the heat treatment.

observed in these histograms. Longer heating time did not produce any further improvement.

6.5 CHARACTERISATION OF RADIATION DAMAGE IN SILICON PHOTOMULTIPLIERS WITH A MONTE CARLO MODEL

6.5.1 *The Monte Carlo model for the detector output*

A complete model for the MPHD of SiPM was derived based on a Monte Carlo simulation. For the model, Poisson distributed photoelectron and dark signals are generated independently. Each of these signals can cause optical cross-talk and after-pulses according to a given probability distribution. For this set of pixels the distribution in time is generated with respect to an integration time window. Single pixels can contribute with varying gain to the generation of the detector output. Finally, the noise is added. The free parameters of the simulation are: mean signal amplitude (A), gain variation (σ_G), dark pulse rate (r), optical cross-talk probability (p_{opt}), after-pulse probability (p_{aft}), trap lifetime (τ), mean number of detected photons (λ), pedestal position (x_{ped}), and noise amplitude (σ_{ped}). In the following, the simulated processes are explained.

As SiPM are a set of APD connected in parallel many of their properties are thus inherited. Its dark count rate, r, is the sum of all the APD dark count rates. After-pulses appear in each pixel after a photon (or a thermically generated charge carrier) triggers an avalanche due to trapped carriers that are released after some time-delay. The after-pulse probability, p_{aft}, is defined as the fraction of events in which one additional signal is generated after the detection of a photon. It is the product of the trapping probability and the triggering probability, both

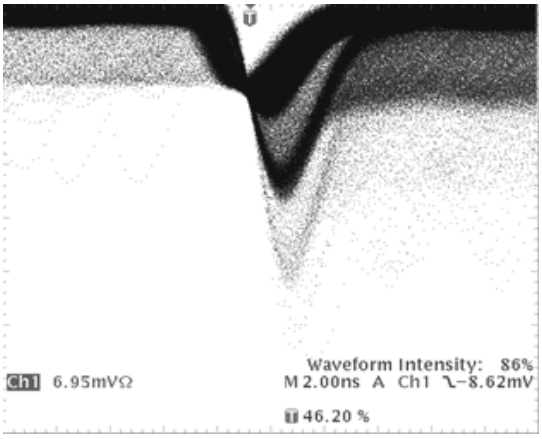

Figure 74: The simultaneous signals from up to three pixels are visible in this oscilloscope trace. Optical cross-talk between adjacent pixels that form a cluster generates these events. The MPHD model described in the text assumes all signals in a cluster to appear at the same time.

increasing linearly with the applied bias voltage. The trap lifetime, τ, determines the typical time-scale.

SiPM are manufactured so that signal uniformity from pixel to pixel is quite good, typically within 10 % [89]. The small variation, σ_G, together with the narrow single electron response function of each APD provides excellent photon counting capabilities and as many as 20 photons can easily be resolved in a typical pulse height spectrum [78]. The distance between multi-pixel peaks in the spectrum is a measure of the charge gain, A.

Surface leakage currents do not cross the multiplication region. Their fluctuations are merged with other noise sources to define the noise amplitude as measured by the pedestal width, σ_{ped}. A change in the surface leakage current should also appear as a shift in pedestal position, x_{ped}.

An avalanche of 10^6 carriers in any of the micro-metric APD forming the SiPM will create around 50 photons via hot carrier luminescence with enough energy to trigger any neighbouring pixel [90]. Devices without trenches filled with opaque material exhibit optical cross-talk, where at least one photon is able to cross the spacing between micro-cells to produce a simultaneous signal (within 100 ps). Fig. 74 shows the effect of optical cross-talk in the SiPM elementary signal. The well defined amplitudes of the multi-pixel events is a result of the simultaneity of the composing signals.

Optical cross-talk is modeled by considering the probability, q, of simultaneous activation of two isolated pixels when one of them has been triggered and deducing the probability for all possible clusters in the SiPM pixel matrix. No distinction is made when there is more than one neighbour active. Fig. 75 shows all independent cluster types

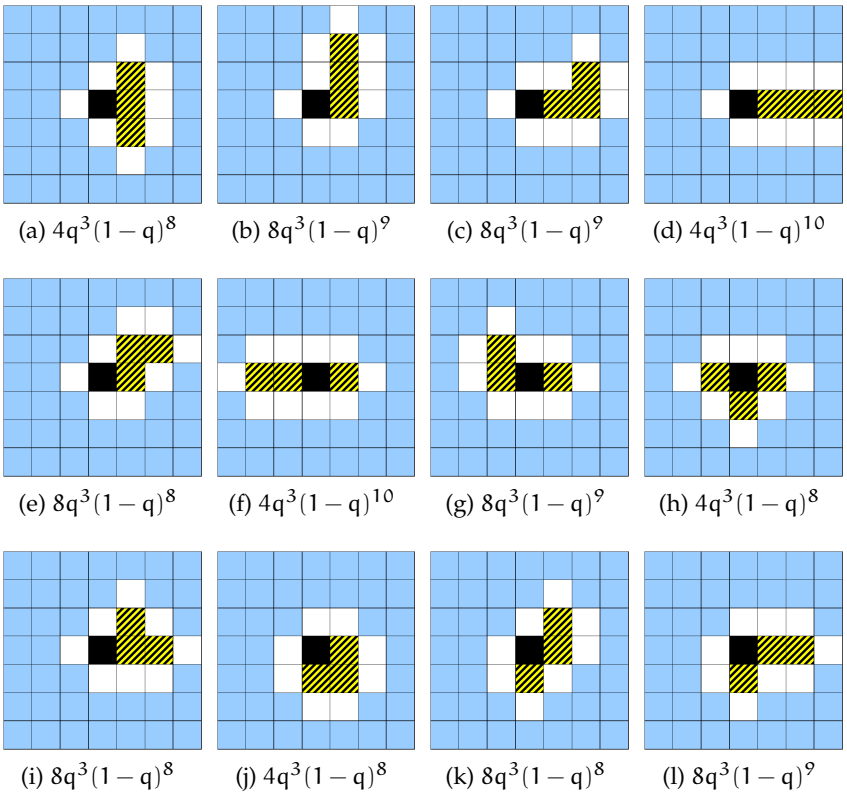

(a) $4q^3(1-q)^8$ (b) $8q^3(1-q)^9$ (c) $8q^3(1-q)^9$ (d) $4q^3(1-q)^{10}$

(e) $8q^3(1-q)^8$ (f) $4q^3(1-q)^{10}$ (g) $8q^3(1-q)^9$ (h) $4q^3(1-q)^8$

(i) $8q^3(1-q)^8$ (j) $4q^3(1-q)^8$ (k) $8q^3(1-q)^8$ (l) $8q^3(1-q)^9$

Figure 75: Independent clusters in which three pixels have been fired (crossed cells) in addition to the initial one (solid cell) as a consequence of optical cross-talk. Any of the possible 76 patterns can be derived from (a) to (l) by symmetry operations. White cells represent pixels which remain off. The sum of all terms equals $P(3) = q^3[36(1-q)^8 + 32(1-q)^9 + 8(1-q)^{10}]$, where q is the probability of activation of a single pixel. No distinction is made when there is more than one neighbour active.

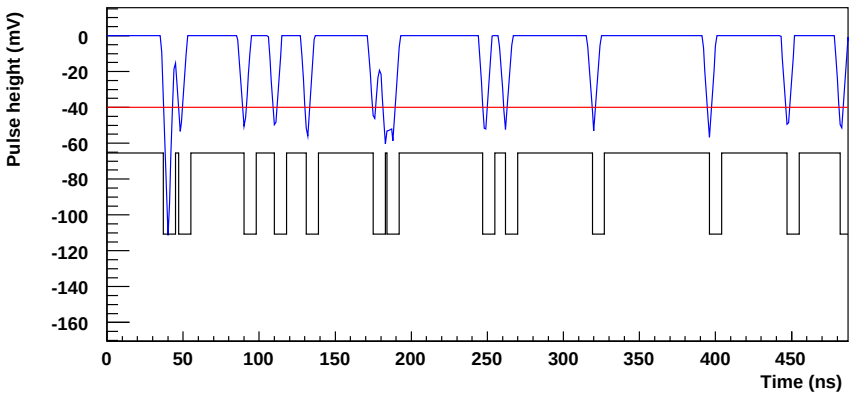

Figure 76: Signals generated by the MPHD model. The straight line is the variable threshold level. Output of the leading edge discriminator is shown below. Superposition of signals and optical cross-talk are visible in the first two peaks, a variation in the amplitude is observed for the next three single-pixel signals an after-pulse is visible in the next group of piled-up signals.

for the case of three additional pixels. Only pixels sharing one side are allowed as part of a cluster. Cluster probabilities are given by the zero pixel cross-talk probability $P(0) = (1-q)^4$, and the N-pixel cross-talk probabilities $P(1) = 4q(1-q)^6$, $P(2) = q^2[6(1-q)^8 + 12(1-q)^7]$, and $P(3) = q^3[32(1-q)^8 + 32(1-q)^9 + 8(1-q)^{10}]$. The terms with $(1-q)$ are a consequence of the requirement that the pixels outside the cluster have to remain off. In absence of optical cross-talk, noise and after-pulses the pixel number distribution should be Poissonian. The mean value of this distribution, λ, gives a measure of the photon detection efficiency for a known amount of photons impinging on the photo-detector surface.

A realistic leading edge discriminator was implemented taking into account the blocking time of the module while the output is active (10 ns). Fig. 76 shows some of the pulses generated by the MPHD model, the threshold line and the output of the leading edge discriminator. Superposition of signals and optical cross-talk are visible in the first two peaks, a variation in amplitude can be observed in the next three single pixel signals and an after-pulse is visible in the next group of piled-up signals.

Fig. 77 shows the measured pulse-height spectra for low amplitude signals induced by a short pulsed UV laser[1] exciting a plastic scintillator. The data was taken with five different bias voltages. Underlying curves are the results of the MPHD model. The residuum between MPHD model and data is shown in panel (f), where the curves for difference bias voltages are off-set by $n \times 0.004$ to improve visibility. Table 10 summarises the resulting set of parameters. Fig. 78 shows the measured noise rate for a bias voltage of 17.9 V. The step structure is

1 NanoLED by Horiba Jobin Yvon, http://www.jobinyvon.com/NanoLED (2007)

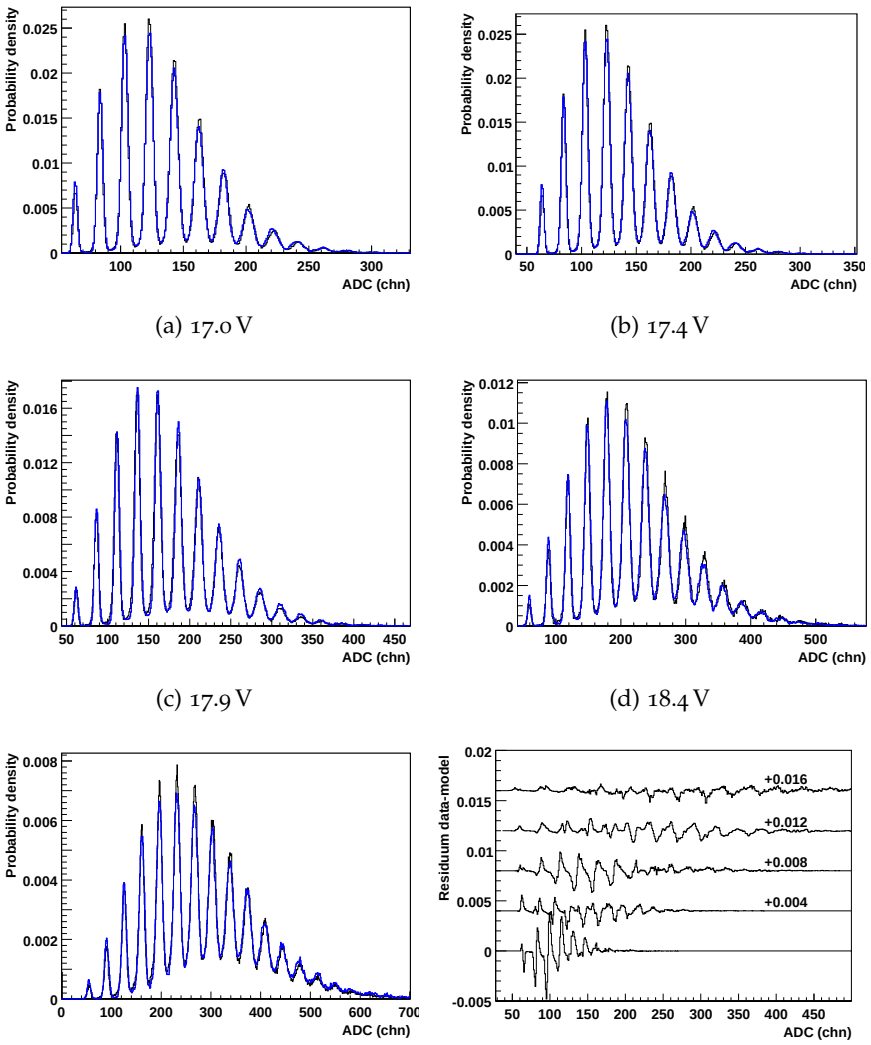

(a) 17.0 V

(b) 17.4 V

(c) 17.9 V

(d) 18.4 V

(e) 18.9 V

(f) Residuum data-model for all 5 bias voltages

Figure 77: Measured pulse-height spectra for five different bias voltages. Underlying curves are the result of the MPHD model described in the text, see Table 10 for the resulting set of parameters. Panel (f) shows the residuum between model and data, where the curves for difference bias voltages are off-set to improve visibility.

Table 10: MPHD model results for five bias voltages. The free parameters of the simulation are: mean signal amplitude (A), gain variation (σ_G), dark pulse rate (r), optical cross-talk probability (p_{opt}), after-pulse probability (p_{aft}), trap lifetime (τ), mean number of detected photons (λ), pedestal position (x_{ped}), and noise amplitude (σ_{ped}).

parameter	17.0 V	17.4 V	17.9 V	18.4 V	18.9 V
A (mV)	35.	43.	55.	66.	78.
σ_G (chn)	0.08	0.07	0.05	0.07	0.06
r (MHz)	3.21	4.06	4.50	6.35	7.33
p_{opt}	0.011	0.020	0.028	0.033	0.048
p_{aft}	0.02	0.08	0.10	0.13	0.17
τ (ns)	8.1	8.0	9.6	8.6	11.9
λ (ph.)	2.76	3.27	3.99	4.60	5.06
x_{ped} (chn)	65.2	63.9	61.6	59.0	54.9
σ_{ped} (chn)	1.49	1.69	2.10	2.45	3.40

due to the multi-pixel events caused by optical cross-talk. Its sharpness is governed by the gain uniformity over the pixels and by the narrowness of the single pixel response function. Last steps are less defined due to the higher number of pixels involved. The pixels are better resolved with increasing bias voltages as a result of well known increase in the charge gain. The strong increase of noise rate with bias voltage is also visible. The open symbols are a result of the Monte Carlo. Simulated noise amplitude and gain variation have the same value as given in Table 10.

6.5.2 *Observed damage*

The SiPM were characterized before and after irradiation by studying the noise rates and the pulse-height spectra for low amplitude signals as explained in section 7.3.2. Fig. 79 shows the noise rate before and after irradiation with 31×10^8 electrons of 14 MeV energy as a function of threshold in a leading edge discriminator. The figure includes curves for three different bias voltages. Two observations were made after the irradiation:

1. the rates of dark pulses are significantly larger.
2. the steps are much less pronounced than before irradiation.

The simulation shows that an increase in the dark count rate is insufficient to explain the curves and it confirms that either an increase in the noise amplitude or the loss of gain uniformity (or a combination of both) can reproduce the measured values.

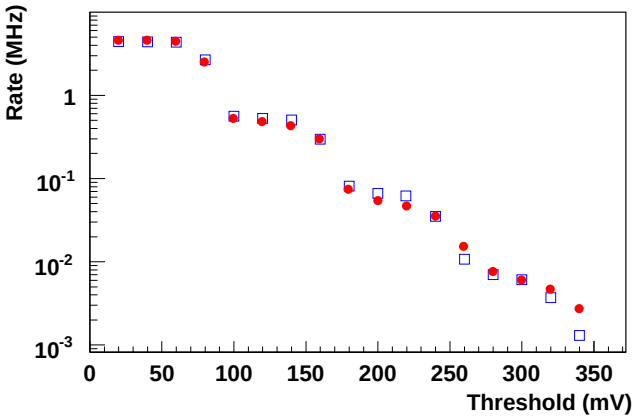

Figure 78: Measured noise rate as a function of discriminator threshold for a bias voltage of 17.9 V. The open symbols are the result of the MPHD model. Simulated noise amplitude and gain variation have the same values as given in Table 10.

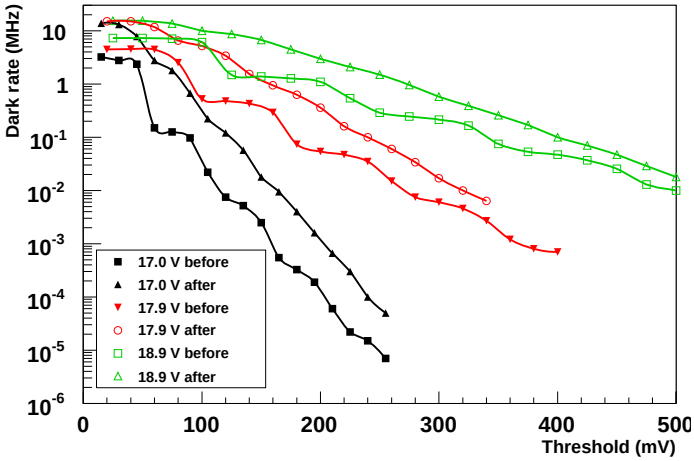

Figure 79: Measured noise rate before and after irradiation with 3.1×10^8 electrons/mm^2 of 14 MeV energy as a function of threshold in a leading edge discriminator. The plot shows curves for three different bias voltages. The step structure is due to the multi-pixel events caused by optical cross-talk. After irradiation the steps are less pronounced because of the much higher noise rate.

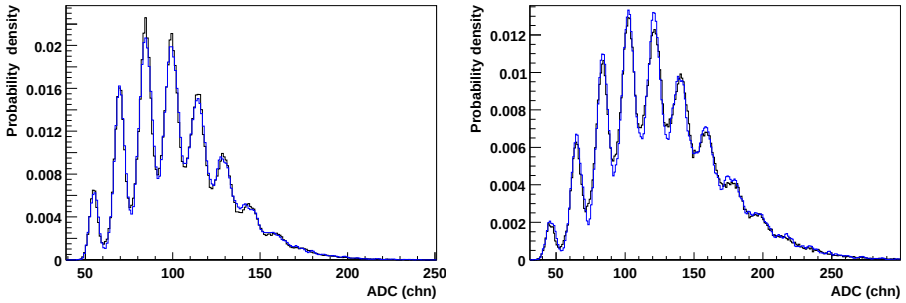

(a) bias voltage of 17.0 V (b) bias voltage of 17.4 V

Figure 80: Pulse-height spectra after irradiation with 3.1×10^8 electrons/mm^2 of 14 MeV energy for low amplitude signals. The underlying curves are a result of the MPHD model.

The histograms in Fig. 80 show measured ADC spectra for bias voltages of 17.0 and 17.4 V (compared to 17.9 V recommended voltage). The MPHD model was tested on this low photon yield data. The simulated integration of signals was performed in an interval of 30 ns, and the mean width of the single-pixel signal was 9 ns. The pedestal peak in this case was clearly separated from the one-pixel peak. After-pulse probability was set to zero and the values for the noise rate and optical cross-talk probability were deduced from the measured noise rates as a function of discriminator threshold. The value of q was given to a good approximation by the ratio of noise rates above and below the first step $P(2)/P(1) = 4(q^3 - 2q^2 + q)$.

The dark count rate might naively be taken from the measurement at lowest discriminator threshold, however, this value is not reliable due to the high probability of signal pile-up. If one assumes that the optical cross-talk probablility was not significantly modified by the low radiation doses the dark count rate can be calculated by multiplying the noise rate for a threshold between one and two pixels by $1/4(q^3 - 2q^2 + q)$. The distributions were well reproduced when noise amplitude and gain variation were allowed to change. The values for the gain variation before and after irradiation were 0.08 chn and 0.12 chn, respectively. The noise amplitude changed from 1.49 chn before to 2.44 chn after irradiation. The good matching of the two curves is a confirmation of the hypothesis of low after-pulse probability. It seems necessary to conclude that there has been an increase in leakage current and a severe loss of gain uniformity.

7

CONCLUSIONS

We have shown that the readout of $2 \times 2\,\mathrm{mm}^2$ square scintillating fibers by SiPM can lead to a high detection efficiency for highly relativistic electrons. Specific difficulties as light attenuation and time dispersion have been discussed and proved to be of relevance for tracking detectors based on long scintillating fibers read out by SiPM. The study showed that an accidental coincidence rate of around 100 Hz to 1 kHz per fiber is present for normal particle incidence when requiring efficiencies above 95 %. Numerical calculations on the accidental coincidence rate were performed for different fiber diameters to supply a convenient reference for particular applications. The horizontal tracking sub-detector at the electron arm of KAOS spectrometer will face a favorable situation with the average incident angle of the crossing particles is 60° with respect to the normal to the detector surface, effectively giving a 4 mm thick fiber read out by a 2 mm diameter photodiode. It is expected that with this geometry a near 100 % detection efficiency at an almost zero accidental coincidence rate is ensured for the detector. Multi-anode photomultipliers are routinely used for scintillating fibre detector read-out showing all the drawbacks of conventional phototubes: stiff cables, high voltage power supplies and magnetic field sensitivity in addition to the specific problem of optical cross-talk among their many channels. If SiPM could be used instead an overall price reduction and a considerable detector simplification would be obtained. Conventional experimental techniques used to deal with high noise rates such as coincidences of several detectors can be complemented with more sophisticated methods based on intelligent trigger algorithms implemented in FPGA chips in order to obtain a reliable tracking detector. Cooling Peltier modules would reduce dramatically the noise rates in case the mentioned methods prove to be insufficient [91].

Of course any change in the SiPM performance will compromise this acceptable although fragile situation.

The well known increase in leakage current of silicon detectors after irradiation and the high electromagnetic and hadronic background that the KAOS detectors will be exposed to needed a deeper understanding of how SiPM respond to irradiation. Electron beam irradiation has shown that a large increase in dark count rate and a partial loss of gain uniformity occur at relatively low doses. Surface effects are also appreciated in the pedestal position shift. Background irradiations in the experimental area under typical beam-time conditions also show similar effects. Realistic amounts of shielding have

been tested and found to have only a relatively poor performance. More massive external shielding and SiPM produced by different manufacturesis are under discussion. The observed increase in dark count rate can introduce an additional complication: Low light level detection does not require large dynamic range SiPMs. Consequently the number of pixels in the detector matrix can be kept relatively small what would result in an appropriate high PDE due to the resulting large fill factor. On the other hand spontaneous pixel activation is stimulated on irradiated SiPM giving rise to a reduced effective number of active pixels due to the time needed to charge the intrinsic capacitor trough the quenching resistor (dead time). Dynamic range is reduced as a consequence in irradiated SiPM and this effect has to be taken into account to choose the optimum number of APDs for applications in high radiation environments.

A

THEORETICAL BACKGROUND

Observations always involve theory.

— Edwin Hubble

A.1 OVERVIEW

In this appendix, we will derive in detail the general structure of the differential cross-section for the reaction $e(p, e'K^+)Y$ analyzed in this thesis. Our aim is providing a complete, unified and pedagogical reference within the text itself, where the constrains imposed by the known electromagnetic interaction on the cross-section can be clearly understood. The derivation is mostly based on references [7, 92, 93, 94, 95, 96, 97, 98, 99, 100] conveniently adapted for our particular case.

Starting from a simple example in non relativistic multichannel scattering theory, the concept of transition charge density is introduced. Relativistic electron scattering off the proton is then studied by considering the dynamics of its spinorial wave function in the external electromagnetic field produced by the evolving hadronic system, effectively described by a transition current density.

Following Bjorken and Drell, Green functions are introduced inspired by Huygens principle and used to derive the integral equation satisfied by the electron field. The scattering amplitude is then immediately obtained by a simple projection of the electron wave function at $t = +\infty$ onto the plane wave representing a possible final state. It is argued that if the interaction is weak, the state of the outgoing electron can be sufficiently well described by its initial wave function in the integral equation for the scattering amplitude (what defines the Born approximation). The result has the suggestive structure of two transition currents hocked together, the well known electron current and the structurally rich hadronic current. The squaring of this amplitude is written in terms of the contraction of the leptonic and hadronic tensors: The first one, fully determined by the electron kinematics and the second one, codifying the dynamics of the reaction channel.

Gauge invariance is used to establish some constrains on the components of these tensors. The general form of the cross-section, resulting from the remaining terms in the contraction, is then explicitly written by expressing the components of the leptonic tensor as functions of the electron variables and exploiting Lorentz covariance of the hadronic tensor to extract the azimuthal angle dependency.

A natural separation in terms of virtual photon flux and virtual photoproduction cross-section is obtained by comparing electro and

photoproduction amplitudes. The notion of virtual photon density matrix is introduced and the standard labeling of the cross-section components in terms of longitudinal and transversal degrees of freedom of the virtual photon is justified.

The resulting formalism proves that electron induced reactions are particularly interesting since the whole process gets reduced to a limited set of hadronic "responses" codifying the behavior of the system under electromagnetic excitations.

A.2 TRANSITION CHARGE DENSITY

Before facing the fully relativistic problem of the general form of the electroproduction cross-section at first order in perturbation theory (the so called one photon exchange approximation), we will work out in some detail a simpler, non-relativistic, scattering problem where many of the important concepts needed will appear in a clearer way, providing a useful guide for the relativistic generalization to the electroproduction case.

Let us then consider the collision of an electron with a Hydrogen atom. We will assume that the proton has no structure and it is infinitely heavy (this will allow us to identify the lab and the center of mass frames). Only Coulomb interaction between the particles will be taken into account. We will study the case where the electron is scattered to some final momentum $\mathbf{p}'$ leaving the atom in any of its possible bound states (so we consider simultaneously elastic and inelastic scattering). The "free" Hamiltonian now consists of two kinetic terms for the projectile and the bound electron and the Coulomb potential linking the proton and the orbiting electron:

$$H = \frac{\mathbf{p}_{e_1}^2}{2m_e} + \frac{\mathbf{p}_{e_2}^2}{2m_e} + V_{pe_2} \tag{A.1}$$

The scattering potential will reflect the interaction between the incoming electron and both the proton and the electron forming the bound state:

$$V = V_{e_1e_2} + V_{e_1p} \tag{A.2}$$

The Born approximation for this reaction is:

$$\begin{aligned}\left\langle \mathbf{p}', 2 \,\middle|\, V \,\middle|\, \mathbf{p}, 1 \right\rangle =& (2\pi)^{-3} \int d^3x_{e_1} \int d^3x_{e_2} e^{-i\mathbf{p}'\cdot\mathbf{x}_{e_1}} \phi_2(\mathbf{x}_{e_2})^* \\ & \times [V_{e_1e_2}(\mathbf{x}_{e_1e_2}) + V_{e_1p}(\mathbf{x}_{e_1})] e^{i\mathbf{p}\cdot\mathbf{x}_{e_1}} \phi_1(\mathbf{x}_{e_2}).\end{aligned} \tag{A.3}$$

Where $|\mathbf{p}, 1\rangle$ and $|\mathbf{p}', 2\rangle$ are basis vectors in channel subspaces 1 and 2 respectively, obtained as a direct product of a plane wave for the

electron motion and the corresponding bound state wave function[1] $\phi_1(\mathbf{x}_{e_2})$ or $\phi_2(\mathbf{x}_{e_2})$.

We will now add the further conditions $V_{e_1 p} = 0$ and $\phi_2 = \phi_1$. That is, we will consider elastic scattering and ignore the interaction of the projectile with the proton (since the proton state does not suffer any change, its contribution is trivial), to get:

$$\begin{aligned}\langle \mathbf{p}', 2 \,|\, V \,|\, \mathbf{p}, 1 \rangle &= (2\pi)^{-3} \int d^3x_{e_1} e^{i\mathbf{q}\cdot\mathbf{x}_{e_1}} \int d^3x_{e_2} V_{e_1 e_2}(\mathbf{x}_{e_1} - \mathbf{x}_{e_2}) |\phi_1(\mathbf{x}_{e_2})|^2 \\ &= (2\pi)^{-3} \int d^3x_{e_1} e^{i\mathbf{q}\cdot\mathbf{x}_{e_1}} \tilde{V}(\mathbf{x}_{e_1}) \end{aligned} \tag{A.4}$$

where $\mathbf{q} = \mathbf{p} - \mathbf{p}'$ is the momentum transfer. The second expression has exactly the form of the Born approximation for scattering by the potential $\tilde{V}(\mathbf{x}_{e_1})$, resulting from averaging $V_{e_1 e_2}$ with respect to the distribution $|\phi_1(\mathbf{x}_{e_2})|^2$. That is, if we compute the elastic electron-atom amplitude using the Born approximation, we obtain the same result as if we consider the scattering of the electron by the static charge distribution defined by the orbiting electron. We could then say that, in the Born approximation, the distortion of the electronic cloud generated by the projectile is ignored.

What would be the situation for the case of inelastic scattering? Now there are two different wave functions and correspondingly two different charge distributions. Clearly the amplitude can be written in the following way:

$$(2\pi)^{-3} \int d^3x_{e_1} e^{i\mathbf{q}\cdot\mathbf{x}_{e_1}} \int d^3x_{e_2} V_{e_1 e_2}(\mathbf{x}_{e_1} - \mathbf{x}_{e_2}) \phi_1(\mathbf{x}_{e_2}) \phi_2^*(\mathbf{x}_{e_2}) \tag{A.5}$$

We could again call the second integral $\tilde{V}(\mathbf{x}_{e_1})$ and speak about an static scattering in that potential. As expected, this effective potential involves both wave functions and can be written in the suggestive form:

$$\tilde{V}(\mathbf{x}_{e_1}) = \int d^3x_{e_2} \frac{1}{e} V_{e_1 e_2}(\mathbf{x}_{e_1} - \mathbf{x}_{e_2}) \int d^3x \phi_2^*(\mathbf{x}) e\delta(\mathbf{x}_{e_2} - \mathbf{x}) \phi_1(\mathbf{x}) \tag{A.6}$$

where the second integral is just the matrix element of the charge density operator $\rho(x) = e\delta(\mathbf{x}_{e_2} - \mathbf{x})$. We may well say that the scattering takes place in the field created by the transition charge density $\langle \phi_2 \,|\, \rho \,|\, \phi_1 \rangle$.

A.3 RELATIVISTIC SCATTERING IN AN EXTERNAL ELECTROMAGNETIC FIELD

Motivated by the previous example, we will split the electroproduction problem in two parts: First, we will assume that the electromagnetic

1 Here we follow [92] where more details on non relativistic quantum multichannel scattering theory can be found. See also [93] for a shorter but enlightening and self-contained presentation.

effect of the whole reaction process on the proton side can be described by an effective electromagnetic field created by a "transition current". Second, we will consider the scattering of the electron in that given external field.

In this section, we will study the relativistic scattering of electrons in general external electromagnetic fields. For a complete derivation we refer the reader to [94]. The calculation is entirely based on the Dirac wave equation for the electron integrated with hole-theory boundary conditions (positrons are interpreted as negative-energy electrons running backwards in time). This propagator approach, originally developed by Feynman, allows the formulation of a working theory in a simple and intuitive way and avoids the troubles of the heavy formalism of quantum field theory. Here we will just give a condensed derivation (it has the value of going straight to the point showing the core of the idea).

First we need to know the equation that governs the evolution of a Dirac spinor in the presence of an external electromagnetic field. This one is obtained from the Dirac equation, $(i\gamma^\mu\partial_\mu - m)\Psi(x) = 0$, just by making the substitution $p^\mu \to p^\mu - eA^\mu$ (where $p^\mu = i\partial^\mu$ in the space-time representation). The resulting equation can be written in the suggestive form:

$$(i\gamma^\mu\partial_\mu - m)\Psi(x) = e\gamma^\mu A_\mu(x)\Psi(x) \tag{A.7}$$

Here the roll of the term $e\gamma^\mu A_\mu(x)\Psi(x)$ as a source for $\Psi(x)$ itself should be clear.

We see that the difference between the evolution of the free Dirac field and the one coupled to an external electromagnetic field is just that at each point in space-time there is a source $\rho(x) \equiv e\gamma^\mu A_\mu(x)\Psi(x)$ of spherical waves whose effect has to be added to any free solution. The evolution of this spherical wave is dictated by the solution of the Dirac equation with a delta function as a source and with the boundary condition of having only outgoing positive energy waves. Calling $S_F(x-y)$ at the mentioned solution at space-time point x for excitation at a point y, we can simply write (using $\rho(x)$ as a weight for each spherical wave):

$$\Psi(x) = \psi_i(x) + e\int d^4y S_F(x-y)\gamma^\mu A_\mu(y)\Psi(y) \tag{A.8}$$

If we think of $\psi_i(x)$ as a free solution representing the incoming electron, clearly the remaining term will represent the scattered wave. Apparently, we have not gone very far since the the unknown field $\Psi(x)$ appears in both sides of the equation, but in this form a clear approximation scheme can be developed by iteration if the interaction is weak.

In an scattering experiment we are interested in the form of $\Psi(x)$ in the remote future ($x_0 \to +\infty$). In order to calculate the amplitude

for finding the outgoing electron in a given state represented by a plane wave $\psi_f(x)$, we have to calculate $\int d^3x\bar{\psi}_f(x)\Psi(x)$. The first term clearly gives δ_{fi}. For the second one we realize that:

$$\int d^3x\bar{\psi}_f(x)S_F(x-y) = \bar{\psi}_f(y) \tag{A.9}$$

since it is easy to prove that the free propagator $S_F(x-y)$ carries $\bar{\psi}$ backwards in time.

This allows us to write:

$$S_{fi} = \delta_{fi} - ie\int d^4y\overline{\psi}_f(y)\gamma^\mu A_\mu(x)\Psi_i(y) \tag{A.10}$$

To lowest order $\Psi(x)$ reduces to the incident plane wave $\psi_i(x)$ and the amplitude for a transition between the distinct initial and final electron states represented by the four dimensional Dirac spinors[2] $\psi_i(x) = \sqrt{\frac{m_e}{E_eV}}u(p_e,s)e^{-ip_ex}$ and $\bar{\psi}_f(x) = \sqrt{\frac{m_e}{E'_eV}}\bar{u}(p'_e,s')e^{ip'_ex}$ will be given by:

$$S_{fi} = -i\int d^4x[e\bar{\psi}_f(x)\gamma^\mu\psi_i(x)]A^\mu(x) \tag{A.11}$$

A.4 SCATTERING IN THE FIELD OF THE EVOLVING HADRONIC SYSTEM

Knowing how the electron will scatter in an external field is now the moment to consider how to calculate such a field for the problem at hand.

The classical field A^μ can be calculated if the source current J^μ is known using again the propagator technique:

$$A^\mu(x) = \int d^4yD_F(x-y)J^\mu(y) \tag{A.12}$$

where D_F is the Feynman propagator:

$$D_F(x-y) = \int \frac{d^4q}{(2\pi)^4}e^{-iq(x-y)}\left(\frac{-1}{q^2+i\epsilon}\right) \tag{A.13}$$

It represents the outgoing spherical wave resulting from a delta excitation at the space-time point y (these boundary conditions are satisfied thanks to the $i\epsilon$ term in the denominator what amounts to the zero value of the propagator for $y_0 > x_0$). The reader should realize that since the source term in the Maxwell equation $\partial^2A^\mu = j^\mu$ does not involve the field itself, the given equation is indeed a method for obtaining $A^\mu(x)$ for a given electromagnetic current.

2 We normalize to unit probability in a box of volume V.

A physically appealing choice for J^μ suggested by the non relativistic example given above is the transition matrix element of the proton current[3]. For an structureless proton this is just:

$$J^\mu(x) = e_p \bar{\psi}^p_f(x)\gamma^\mu\psi^p_i(x) \tag{A.14}$$

The symmetric form obtained for the S matrix with this choice increases our faith on it since clearly there must be a proton-electron symmetry in this result (we could well say that it is the proton who suffers the scattering in the field created by the electron). It is also very well known from quantum field theory that the resulting expression for the scattering of two distinct point like Dirac fermions is correct.

For an structured proton, a well defined electromagnetic current operator $J^\mu(\mathbf{x}, t)$ exists and the corresponding transition matrix element between initial and final hadronic states $\langle f | J^\mu(\mathbf{x}, t) | i \rangle$ will be the source of the four potential A^μ. The states can be taken as eigenstates of four-momentum so the entire space-time dependence can be extracted as[4]:

$$\langle f | J^\mu(\mathbf{x}, t) | i \rangle = \langle f | J^\mu(0) | i \rangle \, e^{i(p'_p - p_p)x} \tag{A.15}$$

---

3 Interestingly, when recoil is allowed (here the motion of the proton clearly contributes to the current), the apparently very different physical situation is in fact intimately connected -in this approximation- with the scattering off a fixed proton. In fact, in the interaction of two point like charge particles with or without spin, the effect of recoil in the cross section is always given by a multiplicative factor $f_{rec} = k/k' = 1 + (2k/M)\sin^2(\theta/2)$ [95, 94]. One can show that the main contribution to this recoil factor comes from the modified density of final states. In more complex situations, the dynamical contribution is hidden in the unknown transition current. It is a common practice assuming that the target does not recoil in order to calculate from hadronic models the corresponding transition current and taking recoil effects into account only through the phase space factor. The center-of-mass motion can in fact be handled correctly in the usual non-relativistic many-body problem. See appendix B of [96] for a short discussion or [97] for a more detailed explanation. The extension to the fully relativistic case is still an open problem.

4 The transformation of a field operator F(x) under an space-time translation $x' = x + a$ is given by a unitary operator defined by:

$$F(x) \to F'(x') = U(a)F(x)U^{-1}(a) = F(x + a)$$

Using Heisenberg equations of motion:

$$i\partial^\mu F(x) = [P^\mu, F(x)]$$

(where P^μ are the energy-momentum operators), it is easy to prove that:

$$U(a) = e^{i a_\mu P^\mu}$$

Taking $a_\mu = -x_\mu$ we can relate the current matrix element at point x with its value at zero:

$$\langle f | J^\mu(\mathbf{x}, t) | i \rangle = \left\langle f \left| U^{-1}(-x)J^\mu(0)U(-x) \right| i \right\rangle = e^{-ix(p_i - p_f)} \langle f | J^\mu(0) | i \rangle$$

where in the last step we have used that initial and final states have well defined energy and momentum.

When this expression is used in (A.12) we get:

$$A^\mu(x) = \int d^4q \, \langle f | J^\mu(0) | i \rangle \left(\frac{-1}{q^2 + i\epsilon} \right) e^{-iqx} \int \frac{d^4y}{(2\pi)^4} e^{i(q+p'_p-p_p)y} = \\ = \langle f | J^\mu(0) | i \rangle \left(\frac{-1}{(p_e - p'_e)^2 + i\epsilon} \right) e^{-i(p'_p-p_p)x} \tag{A.16}$$

where we have use momentum conservation $p'_p - p_p = p_e - p'_e$.

Extracting also the space-time dependence in the electron transition current, the required S-matrix takes the form:

$$\langle f | S | i \rangle = -ee_p \sqrt{\frac{m_e^2}{E_e E'_e V^2}} \bar{u}_f \gamma_\mu u_i \frac{1}{q^2} \langle f | J^\mu(0) | i \rangle (2\pi)^4 \delta^4(p'_p - p_p - q) \tag{A.17}$$

Since we are interested in kaon electroproduction, we will specify to a two-particle final state $|p_\Lambda p_K\rangle$. This is an exact eigenstate of the total Hamiltonian. To go to states with Lorentz invariant norm, one defines:

$$J_\mu \equiv \left(\frac{2E_K E_\Lambda E_P V^3}{m_P m_\Lambda} \right)^{1/2} \langle p_\Lambda p_K | J_\mu(0) | p_P \rangle \tag{A.18}$$

We will also use the notation $j_\mu \equiv \bar{u}_f \gamma_\mu u_i$.

Applying these definitions we get:

$$\langle f | S | i \rangle = -ee_p \left(\frac{m_e^2 m_P M_\Lambda}{E_e E'_e E_K E_\Lambda E_P V^5} \right)^{1/2} j_\mu \frac{1}{q^2} J^\mu (2\pi)^4 \delta^4(p_\Lambda + p_K - p_p - q) \tag{A.19}$$

A.5 FROM THE S MATRIX TO THE CROSS-SECTION. THE LEPTONIC AND HADRONIC TENSORS

To calculate a cross section, we first form a transition rate per unit volume dividing $|S_{fi}|^2$ by the time interval of observation and the spatial volume of the interaction region. This gives:

$$w_{fi} = \frac{|S_{fi}|^2}{VT} = \frac{m_e^2 m_P m_\Lambda}{E_e E'_e E_K E_\Lambda E_P V^5} (2\pi)^4 \delta^4(p_\Lambda + p_K - p_p - q) |ee_p j_\mu \frac{1}{q^2} J^\mu|^2 \tag{A.20}$$

We will use the notation:

$$\mathfrak{M}_{fi} \equiv ee_p j_\mu \frac{1}{q^2} J^\mu \tag{A.21}$$

for the invariant amplitude obtained by the contraction of the two Lorentz four-vectors. The apparently odd square of the δ^4 function can be handled quite easily when the finite space-time volume VT is

taken into account and actually has the convenient effect of removing the VT denominator of the transition rate per unit volume since:

$$(2\pi)^4\delta^4(0)(2\pi)^4\delta^4(p_\Lambda + p_K - p_p - q) \to VT(2\pi)^4\delta^4(p_\Lambda + p_K - p_p - q) \tag{A.22}$$

Next, we divide the transition rate per unit volume by the flux of incident particles $|J_{inc}|$ and by the number of target particles per unit volume; which is $1/V$ according to our normalization. Finally, to get a physical cross section, we must sum over a given group of final states.

The number of states for the final electron in a big box with periodic boundary conditions is $dN = \frac{V}{(2\pi)^3} d^3p'_e$ and similarly for K^+ and Λ.

$$d\sigma = \int V^3 \frac{d^3p'_e}{(2\pi)^3}\frac{d^3p_K}{(2\pi)^3}\frac{d^3p_\Lambda}{(2\pi)^3}\frac{V}{|J_{inc}|}w_{fi} \tag{A.23}$$

Along the electron direction, the incident flux times the remaining volume factor is given by ($m_e = 0$):

$$J_{inc}V = \frac{V_{rel}}{V}V \approx 1 \tag{A.24}$$

what allow us to write:

$$d\sigma = \int \frac{m_e m_p}{E_e E_p}|\mathfrak{M}_{fi}|^2 \frac{m_e d^3p'_e}{(2\pi)^3 E'}\frac{d^3p_K}{(2\pi)^3 E_K}\frac{m_\Lambda d^3p_\Lambda}{(2\pi)^3 E_\Lambda}(2\pi)^4\delta^4(p_\Lambda + p_K - q - p_P - q) \tag{A.25}$$

or

$$d\sigma = \frac{4\alpha^2}{q^4}\frac{d^3p'_e}{2E'_e}\frac{1}{E_e E_p}L_{\mu\nu}W^{\mu\nu} \tag{A.26}$$

where

$$W^{\mu\nu} = \frac{m_p m_\Lambda}{(2\pi)^3}\int \frac{d^3\vec{p}_K}{2E_K}\frac{d^3\vec{p}_\Lambda}{2E_\Lambda}\delta^4(p_k + p_\Lambda - q - p_p)\frac{1}{2}\sum J^\mu J^{+\nu} \tag{A.27}$$

and

$$L_{\mu\nu} = \frac{(2m_e)^2}{2}\sum j_\mu j^+_\nu = 2(p'_{e_\mu}p_{e_\nu} + p'_{e_\nu}p_{e_\mu}) - g_{\mu\nu}Q^2 \tag{A.28}$$

Here we have already assumed that the electron beam and proton target are unpolarized, and that we do not measure the polarization of the outgoing particles. The summatory symbol, then, stands for averaging over initial state polarizations and summing over final states.

In the final form of $L_{\mu\nu}$ we have used standard trace techniques for spin summation [94]. These two expression are manifestly Lorentz second rank tensors. We follow the common practice to evaluate the

electron kinematics in the lab frame but express the triple differential cross section in terms of the final $K^+\Lambda$ variables in their center of mass frame.

We can then write:

$$\frac{d^5\sigma}{dE'_e d\Omega'_e d\Omega^*_K} = \frac{\alpha^2}{Q^4}\frac{E'^{lab}_e}{E^{lab}_e} L_{\mu\nu}\overline{W}^{\mu\nu} \tag{A.29}$$

where we have used the super index lab to indicate that in this expression all quantities have to be evaluated in the hadronic CM frame if they are not labeled lab.

We have also defined:

$$\overline{W}^{\mu\nu} = \frac{1}{(2\pi)^3}\frac{m_p m_\Lambda}{E_p E_\Lambda}\int d|\vec{p}_K|\frac{|\vec{p}_K|^2}{2E_K} d^3\vec{p}_\Lambda \delta^4(p_k + p_\Lambda - q - p_p)\frac{1}{2}\sum J^\mu J^{+\nu} \tag{A.30}$$

A.6 CONSTRAINS ON THE CROSS SECTION STRUCTURE DUE TO GAUGE INVARIANCE

Charge conservation for the evolving hadronic system is ruled by the continuity equation:

$$\partial_\mu \langle p_\Lambda p_K | J^\mu(x) | p_P\rangle = e^{i(p_p - p_\Lambda - p_K)\cdot x} i(p_p - p_\Lambda - p_K)\langle p_\Lambda p_K | J^\mu(0) | p_P\rangle = 0 \tag{A.31}$$

This equality must hold for each space-time point x, implying that the virtual photon four momentum and the transition current are linked by:

$$q_\mu \langle p_\Lambda p_K | J^\mu(0) | p_P\rangle = 0 \tag{A.32}$$

Being $W^{\mu\nu}$ essentially a sum of products of two such currents, we can write:

$$q_\mu W^{\mu\nu} = q_\nu W^{\mu\nu} = 0 \tag{A.33}$$

A similar argument applies to the lepton tensor but since we have an explicit expression for it, we directly use Dirac equation to get:

$$q^\mu j_\mu = \bar{u}_f q^\mu \gamma_\mu u_i = -\bar{u}_f(\gamma_\mu p'^\mu_e - \gamma_\mu p^\mu_e)u_i = 0 \tag{A.34}$$

Choosing the virtual photon direction along the z-axis $q^\mu = (\omega, 0, 0, |\vec{q}|)$ results in the following constrains between tensor components [98]:

$$L^{00} = \left(\frac{|\vec{q}|}{\omega}\right)^2 L^{zz} \tag{A.35}$$

and

$$L^{0i} = \frac{|\vec{q}|}{\omega} L^{zi} \tag{A.36}$$

for the lepton tensor, and

$$W^{00} = \left(\frac{|\vec{q}|}{\omega}\right)^2 W^{zz} \tag{A.37}$$

$$W^{0i} = \frac{|\vec{q}|}{\omega} W^{zi} \tag{A.38}$$

for the hadronic tensor.

Making use of these relations, we can get rid of all time components. The remaining terms in the contraction of both tensors can be conveniently grouped in the following form:

$$\begin{aligned} L_{\mu\nu}\overline{W}^{\mu\nu} =& L^{xx}\overline{W}^{xx} + L^{yy}\overline{W}^{yy} - \frac{Q^2}{\omega^2}(L^{zx}\overline{W}^{zx} + L^{xz}\overline{W}^{xz}) + \frac{Q^4}{\omega^4}L^{zz}\overline{W}^{zz} + \\ & L^{xy}\overline{W}^{xy} + L^{yx}\overline{W}^{yx} - \frac{Q^2}{\omega^2}(L^{yz}\overline{W}^{yz} + L^{zy}\overline{W}^{zy}) \end{aligned} \tag{A.39}$$

where repeated use of the defining equation of momentum transfer $Q^2 = |\vec{q}|^2 - \omega^2$ has been made.

A.7 EXPLICIT FORM OF THE LEPTONIC TENSOR

According to the kinematics shown in Fig. 81 and assuming massless electrons we have:

$$\sin\alpha = \frac{E'_e}{|\vec{q}|}\sin\theta_e \tag{A.40}$$

$$\cos\alpha = \frac{E_e - E'_e\cos\theta_e}{|\vec{q}|} \tag{A.41}$$

Introducing these values in the defining equation for the leptonic tensor A.28 we get:

$$L_{xx} = 4p_{e_x}p'_{e_x} + Q^2 \tag{A.42}$$

Since by definition the change in the electron momentum is along the z direction, we can write:

$$p_{e_x} = p'_{e_x} = E_e\sin\alpha = \frac{E_e E'_e\sin\theta_e}{|\vec{q}|} \tag{A.43}$$

Inserting these values in A.42 we get:

$$L_{xx} = Q^2\left(4\frac{E_e^2 E_e'^2\sin^2\theta_e}{Q^2|\vec{q}|^2} + 1\right) \tag{A.44}$$

Now using that:

$$Q^2 = (p_e - p'_e)^2 = 4E_e E'_e \sin^2 \frac{1}{2}\theta_e \tag{A.45}$$

we arrive at:

$$L_{xx} = Q^2 \left(\frac{E_e E'_e \sin^2 \theta_e}{|\vec{q}| \sin^2 \frac{1}{2}\theta_e} + 1 \right) = Q^2 \left(\frac{E_e E'_e 4 \sin^2 \frac{1}{2}\theta_e \cos^2 \frac{1}{2}\theta_e}{|\vec{q}| \sin^2 \frac{1}{2}\theta_e} + 1 \right) =$$
$$= \frac{Q^2}{|\vec{q}|} \cot^2 \frac{1}{2}\theta_e + 1 = Q^2 \frac{1+\epsilon}{1-\epsilon} \tag{A.46}$$

where we have defined:

$$\epsilon = \left(1 + \frac{2|\vec{q}|^2}{Q^2} \tan^2 \frac{\theta_e}{2} \right)^{-1} \tag{A.47}$$

This quantity is invariant under boosts along the virtual photon direction and for convenience we will evaluate it in the lab frame.

Since by definition the electron scatters in the xz plane, we have:

$$L_{yy} = Q^2 \tag{A.48}$$

and since $g_{\mu\nu} = 0$ for $\mu \neq \nu$, we have:

$$L_{xy} = L_{yx} = 0 \tag{A.49}$$

Now for the components containing z:

$$L_{zz} = 4 p_{e_z} p'_{e_z} + Q^2 \tag{A.50}$$

$$p_{e_z} = E_e \cos \alpha = E_e (E_e - E'_e \cos \theta_e)/|\vec{q}| \tag{A.51}$$

$$p'_{e_z} = p_{e_z} - |\vec{q}| = E'_e (E_e \cos \theta_e - E'_e)/|\vec{q}| \tag{A.52}$$

and the reader can check that this reduces to:

$$\frac{Q^4}{\omega^4} L^{zz} = Q^2 \frac{Q^2}{\omega^2} \frac{2\epsilon}{1-\epsilon} \tag{A.53}$$

and similarly:

$$\frac{Q^2}{\omega^2} L^{zx} = Q^2 \sqrt{\frac{Q^2}{\omega^2}} \frac{\sqrt{2\epsilon(1+\epsilon)}}{1-\epsilon} \tag{A.54}$$

and, of course:

$$L^{yz} = L^{zy} = 0 \tag{A.55}$$

Inserting the calculated components of $L_{\mu\nu}$ in A.39, the following expression results for the five-fold differential cross-section A.29:

$$\frac{d^5\sigma}{dE'_e d\Omega'_e d\Omega^*_K} = \frac{\alpha^2}{Q^2} \frac{E'_e}{E_e} \frac{1}{1-\epsilon} [(\overline{W}^{xx} + \overline{W}^{yy}) + \epsilon(\overline{W}^{xx} - \overline{W}^{yy}) +$$
$$2\epsilon \frac{Q^2}{\omega^2} \overline{W}^{zz} - \sqrt{2\epsilon(1+\epsilon)} \sqrt{\frac{Q^2}{\omega^2}} (\overline{W}^{zx} + \overline{W}^{xz})] \tag{A.56}$$

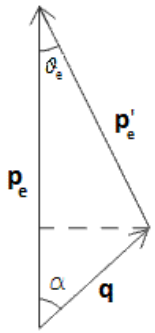

Figure 81: Geometry of the lepton scattering plane

A.8 ϕ DEPENDENCE

In order to extract the ϕ dependence explicitly from W^{ij}, we introduce the most general covariant expression for $W^{\mu\nu}$.

$$\begin{aligned} W^{\mu\nu} =& W_1(-g^{\mu\nu} + \frac{q^\mu q^\nu}{q^2}) + \frac{W_2}{m_p^2}(p^\mu - \frac{p\cdot q}{q^2}q^\mu)(p^\nu - \frac{p\cdot q}{q^2}q^\nu) \\ &+ W_3(\hat{k}^\mu - \frac{\hat{k}\cdot q}{q^2}q^\mu)(\hat{k}^\nu - \frac{\hat{k}\cdot q}{q^2}q^\nu) \\ &+ \frac{W_4}{m_p}\left[(p^\mu - \frac{p\cdot q}{q^2}q^\mu)(\hat{k}^\nu - \frac{\hat{k}\cdot q}{q^2}q^\nu) + (\hat{k}^\mu - \frac{\hat{k}\cdot q}{q^2}q^\mu)(p^\nu - \frac{p\cdot q}{q^2}q^\nu)\right] \end{aligned} \tag{A.57}$$

where $\hat{k}^\mu$ is a unit vector of the kaon momentum and we have simply used p for the proton four momentum. W_1, W_2, W_3 and W_4 are called structure functions. The reader can easily verify that this symmetric tensor[5], by construction, satisfies the current conservation conditions and that it is built out of the three independent vectors available.

Inserting values of p^μ, q^μ and $\hat{k}^\mu$ in the $K^+\Lambda$ center of mass system (see Fig. 82) we have:

$$\begin{aligned} W^{xx} + W^{yy} &= W_1 + W_3\hat{k}^x\hat{k}^x + W_1 + W_3\hat{k}^y\hat{k}^y = 2W_1 + W_3\sin^2\theta^*_K = \\ &= (W^{xx} + W^{yy})_{\phi=0} \end{aligned} \tag{A.58}$$

$$\begin{aligned} W^{xx} - W^{yy} &= W_1 + W_3\hat{k}^x\hat{k}^x - W_1 - W_3\hat{k}^y\hat{k}^y = W_3\sin^2\theta^*_K\cos 2\phi = \\ &= (W^{xx} - W^{yy})_{\phi=0}\cos 2\phi \end{aligned} \tag{A.59}$$

Similarly:

$$W^{zz} = W^{zz}_{\phi=0} \tag{A.60}$$

$$W^{zx} - W^{xz} = (W^{zx} - W^{xz})_{\phi=0}\cos\phi \tag{A.61}$$

5 Any antisymmetric part will not contribute when contracted with the symmetric $L_{\mu\nu}$.

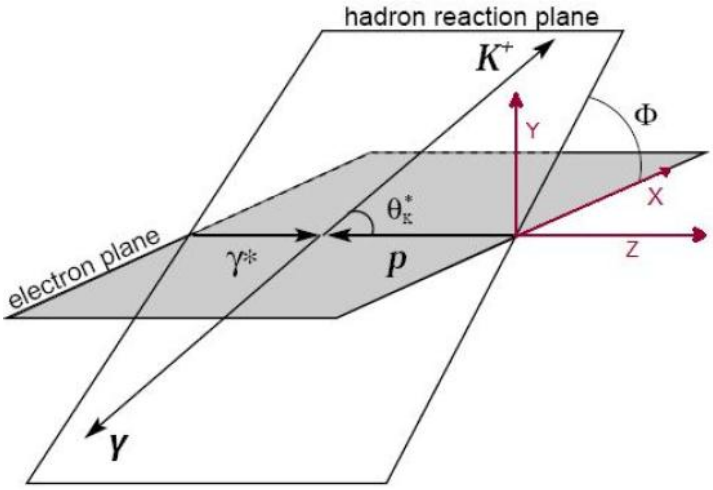

Figure 82: The electron scattering and hadronic reaction planes, as viewed from the hadronic center-of-momentum frame

A.9 FINAL EXPRESSION FOR THE CROSS-SECTION

It is convenient to introduce the virtual photon flux[6]:

$$\Gamma = \frac{\alpha K_H}{2\pi^2 Q^2}\frac{E'_e}{E_e}\frac{1}{1-\epsilon} \tag{A.62}$$

where we have defined $K_H = (W^2 - M_p^2)/2M_p = \omega - \frac{Q^2}{2m_N}$. This is the energy a real photon would have in the laboratory frame to excite a hadronic state of energy W. This quantity is sometimes called in the literature *photon equivalent energy*.

Working out the phase space integral for the final hadrons in the hadronic center of mass frame [96]:

$$\Phi = \int \frac{d^3p_K}{2E_K}\int \frac{d^3p_\Lambda}{2E_\Lambda}\delta^4(p_e + p_P - p'_e - p_K - p_\Lambda) = \frac{|\vec{p_K}|}{4W}d\Omega_K \tag{A.63}$$

we obtain the final form of the five-fold differential cross section:

$$\begin{aligned}\frac{d^5\sigma}{dE'_e d\Omega'_e d\Omega^*_K} &= \Gamma\frac{d\sigma}{d\Omega^*_K}(W, Q^2, \epsilon, \theta_K, \phi_K) = \\ &= \Gamma\left[\frac{d\sigma_T}{d\Omega^*_K} + \epsilon\frac{d\sigma_L}{d\Omega^*_K} + \epsilon\frac{d\sigma_{TT}}{d\Omega^*_K}\cos 2\phi + \sqrt{2\epsilon(1+\epsilon)}\frac{d\sigma_{LT}}{d\Omega^*_K}\cos\phi\right]\end{aligned} \tag{A.64}$$

6 See section A.10 for a detailed discussion of the virtual photon flux concept.

where σ_T, σ_L, σ_{TT} and σ_{LT} are defined by:

$$\frac{d\sigma_T}{d\Omega_K^*} = \frac{1}{(2\pi)^2 K_H} \frac{m_p^2 |\vec{p}_K|}{E_p W} \frac{1}{4} \sum e^2 (|J^x(p_k p_\Lambda, q p_p)|^2 + |J^y(p_k p_\Lambda, q p_p)|)^2{}_{\phi=0} \tag{A.65}$$

$$\frac{d\sigma_L}{d\Omega_K^*} = \frac{1}{(2\pi)^2 K_H} \frac{m_p^2 |\vec{p}_K|}{E_p W} \frac{1}{2} \sum e^2 \frac{Q^2}{\omega^2} |J^z(p_k p_\Lambda, q p_p)|^2{}_{\phi=0} \tag{A.66}$$

$$\frac{d\sigma_{TT}}{d\Omega_K^*} = \frac{1}{(2\pi)^2 K_H} \frac{m_p^2 |\vec{p}_K|}{E_p W} \frac{1}{4} \sum e^2 (|J^x(p_k p_\Lambda, q p_p)|^2 - |J^y(p_k p_\Lambda, q p_p)|^2)_{\phi=0} \tag{A.67}$$

$$\frac{d\sigma_{LT}}{d\Omega_K^*} = \frac{1}{(2\pi)^2 K_H} \frac{m_p^2 |\vec{p}_K|}{E_p W} \frac{1}{2} \sum e^2 \sqrt{\frac{Q^2}{\omega^2}} Re(J^z(p_k p_\Lambda, q p_p) J^{x*}(p_k p_\Lambda, q p_p))_{\phi=0} \tag{A.68}$$

Here, we follow the standard notation where labels T and L refer to transverse and longitudinal components of the virtual photon, that in the Feynman picture mediates the interaction between the electron and proton. In our approach, these labels are justified more directly by the involved components of the hadronic transition current. Next section will introduce the connection between photo- and electroproduction cross-sections by invoquing the concept of virtual photon. We will see that contrary to real photons, virtual photons do have longitudinal polarization giving rise to a purely longitudinal cross-section component and a transverse-longitudinal interference term.

A.10 VIRTUAL AND REAL PHOTONS

We will now briefly review the notion of polarization state for a real photon. Density matrix formalism -as the natural framework for mixed polarization states- will also be discussed.

The requirement of locality in Quantum Field Theory precludes the use of the electromagnetic field tensor in favor of the four vector potential.

The evolution of A^μ is governed by:

$$\Box A^\nu - \partial^\nu (\partial_\mu A^\mu) = j^\nu \tag{A.69}$$

This equation can be simplified by working in the so called Lorentz gauge defined by:

$$\partial_\mu A^\mu = 0 \tag{A.70}$$

The most general solution for the resulting wave equation can be written as:

$$A^\mu(x) = \sum_\lambda \int \frac{d^3\mathbf{k}}{(2\pi)^3 \sqrt{2\omega}} [\epsilon^\mu(k,\lambda)\alpha(k,\lambda)e^{-ikx} + \epsilon^{\mu*}(k,\lambda)\alpha^*(k,\lambda)e^{-ikx}]$$

(A.71)

When A.71 is oblied to fulfill A.70, the polarization vector ϵ^μ and the wave vector k^μ are linked by:

$$k \cdot \epsilon = 0 \tag{A.72}$$

Lorentz condition A.70 does not exhaust completely the gauge freedom since $A^\mu - \partial^\mu \chi$, provided that $\Box\chi = 0$, will still fulfill it. This freedom corresponds to changing ϵ^μ by a multiple of k^μ. The fact the $k^2 = 0$ (photon mass is zero) implies that:

$$(\epsilon^\mu + \beta k^\mu)k_\mu = \beta k^2 = 0 \tag{A.73}$$

for this new ϵ as well.

It is therefore clear that we can arrange for the time component of ϵ^μ to vanish so that the Lorentz condition reduces to the 3-vector condition:

$$\mathbf{k} \cdot \boldsymbol{\epsilon} = 0 \tag{A.74}$$

This means that there are only two independent polarization vectors, both transverse to $\mathbf{k}$. For a wave traveling in the z-direction, a possible choice is:

$$\boldsymbol{\epsilon}_{(1)} = (1, 0, 0) \tag{A.75}$$

$$\boldsymbol{\epsilon}_{(2)} = (0, 1, 0) \tag{A.76}$$

Note that the reduction to only two independent field components relays on the fact that the photon is massless.

Using $\mathbf{B} = \nabla \times \mathbf{A}$ and $\mathbf{E} = -\nabla V - \frac{\partial \mathbf{A}}{\partial t}$, it is easy to see that the corresponding $\mathbf{E}$ and $\mathbf{B}$ fields are linearly polarized. Circularly polarized radiation can be obtained by choosing:

$$\boldsymbol{\epsilon}(\lambda = +1) = -\frac{1}{\sqrt{2}}(1, i, 0) \tag{A.77}$$

$$\boldsymbol{\epsilon}(\lambda = -1) = \frac{1}{\sqrt{2}}(1, -i, 0) \tag{A.78}$$

Photons are elementary quantum excitations of field modes. As an example of a constrained system, several problems are found when the standard techniques of canonical quantization are applied to the electromagnetic field. These difficulties can be , nevertheless, overcome by allowing indefinite metrics in the corresponding Hilbert space and keeping all four polarizations in intermediate calculations. The pure transverse character of the electromagnetic field is recovered

by showing that only those degrees or freedom survive in the final results. In particular, only transverse photons are allowed as incoming or outgoing particles in any reaction.

Let us now consider the absorption of one of this transverse photons by a nucleon [100]. To first order in perturbation theory (Born approximation), the amplitude for this process is given by:

$$T_{fi} = e \langle f | J_\mu | i \rangle \epsilon^\mu \tag{A.79}$$

where ϵ_μ is the polarization of the real photon. $|T_{fi}|$ has to be squared to be converted in the probabilistic factor used in the cross-section:

$$|T_{fi}|^2 = e^2 \langle f|J_\nu|i\rangle^* \langle f|J_\mu|i\rangle \epsilon^{\nu *}\epsilon^\mu = e^2 W_{\mu\nu}\eta^{\mu\nu} \tag{A.80}$$

where we have defined:

$$\eta^{\mu\nu} = \epsilon^{\nu *}\epsilon^\mu \tag{A.81}$$

$$W_{\mu\nu} = \langle f|J_\nu|i\rangle^* \langle f|J_\mu|i\rangle \tag{A.82}$$

Since for real photons $\epsilon^0 = 0$, we can reduce $\eta^{\mu\nu}$ to the so called density matrix $\rho^{ij} = \eta^{ij}$. The density matrix formalism in Quantum Mechanics allows the calculation of any expected value for a mixture of states with real weights.

If the beam of photons is not polarized, the corresponding amplitude will involve an average over the two possible polarizations and since both are equally probable:

$$\rho = \frac{1}{2}\epsilon^{\nu *}_{(1)}\epsilon^\mu_{(1)} + \frac{1}{2}\epsilon^{\nu *}_{(2)}\epsilon^\mu_{(2)} \tag{A.83}$$

or

$$\rho = \begin{pmatrix} 1/2 & 0 & 0 \\ 0 & 1/2 & 0 \\ 0 & 0 & 0 \end{pmatrix} \tag{A.84}$$

For a partially linearly polarized beam with relative strength $(1+\epsilon)$ in the x direction and $(1-\epsilon)$ in y direction:

$$\rho = \begin{pmatrix} \frac{1}{2}(1+\epsilon) & 0 & 0 \\ 0 & \frac{1}{2}(1-\epsilon) & 0 \\ 0 & 0 & 0 \end{pmatrix} \tag{A.85}$$

In principle, a 2×2 matrix is all that is needed for transverse photons, but we have kept the longitudinal components as well, since our purpose is showing that reactions generated by virtual photons

can be characterized also by the product of a hadronic tensor and a virtual photon density matrix. Since virtual photons are not on shell, for them k^2 is not zero, and a longitudinal polarization component is expected being the corresponding density matrix 3×3.

We have seen that the amplitude for the electron nucleon collision in the one photon approximation is:

$$\mathfrak{M}_{fi} \equiv e e_p j_\mu \frac{1}{q^2} J^\mu \tag{A.86}$$

Clearly after squaring, the same structure than in (A.80) will be obtained with the exception of the $1/q^4$ factor. We have already calculated the explicit form of $L_{\mu\nu}$ and seen that if we include the factor $-(k^2/k_0^2)$ coming from current conservation, we can write:

$$|\mathfrak{M}_{fi}|^2 = \frac{1}{Q^4} \frac{2Q^2}{1-\epsilon} \rho_{ij} J^i J^{+j} \tag{A.87}$$

where we have defined:

$$\rho = \begin{pmatrix} \frac{1}{2}(1+\epsilon) & 0 & -\frac{1}{2}\sqrt{\frac{Q^2}{\omega^2}}\sqrt{2\epsilon(1+\epsilon)} \\ 0 & \frac{1}{2}(1-\epsilon) & 0 \\ -\frac{1}{2}\sqrt{\frac{Q^2}{\omega^2}}\sqrt{2\epsilon(1+\epsilon)} & 0 & \frac{Q^2}{\omega^2}\epsilon \end{pmatrix} \tag{A.88}$$

and

$$\epsilon = \left[1 + 2(|\mathbf{k}|^2/k^2)\tan^2\frac{1}{2}\Psi\right]^{-1}$$

We will also define:

$$\epsilon_L = (k^2/k_0^2)\epsilon$$

So we see that we can take out a group of purely electronic factors and leave the product of a density matrix times the hadronic tensor.

When the complete cross-section is written, the resulting prefactor is:

$$\Gamma = \frac{\alpha^2}{Q^2}\frac{E'_e}{E_e}\frac{2}{1-\epsilon} \tag{A.89}$$

Since we can always include appropriate factors in the response functions, several definitions of a "flux of virtual photons" are possible (the reader should keep in mind that the flux of virtual particles is not a well defined concept).

One common definition in the literature is:

$$\Gamma = \frac{\alpha^2}{2\pi^2 Q^2}\frac{E'_e}{E_e}\frac{|\vec{q}|}{1-\epsilon} \tag{A.90}$$

With this definition, the virtual photon cross section is defined in complete analogy with the real photon case [100]. Other definitions are of course possible. We have used:

$$\Gamma = \frac{\alpha^2}{2\pi^2 Q^2} \frac{E'_e}{E_e} \frac{K_H}{1-\epsilon} \tag{A.91}$$

The advantage of it is that K_H has a simpler analytic form than $|\vec{q}|$. We have also absorbed the factors ϵ_L in the longitudinal response functions.

Both definitions are suitable for comparison with real photoproduction since in both cases we recover the photoproduction cross-section in the limit $Q^2 \to 0$.

We also see that in the scattering of unpolarized leptons the density matrix of the virtual photon is the incoherent sum of the two pure states:

$$\epsilon_a = (\left[\frac{1}{2}(1+\epsilon)\right]^{1/2}, 0, -\epsilon_L^{1/2}) \tag{A.92}$$

$$\epsilon_b = (0, \left[\frac{1}{2}(1-\epsilon)\right]^{1/2}, 0) \tag{A.93}$$

This result shows that experiments using unpolarized leptons are equivalent in the small k^2 limit to those using partially linearly polarized photons.

BIBLIOGRAPHY

[1] Albert Einstein. Fundamental ideas and problems of the theory of relativity. *Nobel Lecture delivered to the Nordic Assembly of Naturalists at Gothenburg, July 11, 1923*.

[2] Lui Lam. *Introduction to non-linear physics*. Springer-Verlag, 1997.

[3] Robert M. Wald. *Quantum Field Theory in Curved Spacetime and Black Hole Thermodynamics*. The university of Chicago Press, 1994.

[4] M. E. McCracken. The fate of particles in quantum field theories with interactions. *Forthcoming in Studies in History and Philosophy of Modern Physics*, 2008.

[5] Claude Itzykson and Jean Bernard Zuber. *Quantum Field Theory*. McGraw-Hill, 1980.

[6] S. Capstick and W. Roberts. Strange decays of nonstrange baryons. *Phys. Rev. D*, 58:74011, 1998.

[7] Anthony W. Thomas and Wolfram Weise. *The Structure of the Nucleon*. Wiley-VHC, 2001.

[8] F. Halzen and A. D. Martin. *Quarks and Leptons: An introductory course in Modern Particle Physics*. Ed. John Wiley, 1984.

[9] T. P. Cheng and L. F. Li. *Gauge Theory of Elementary Particles*. Oxford Univ. Press, 1991.

[10] D. J. Gross and F. Wilczek. Ultraviolet behavior of non-abelian gauge theories. *Phys. Rev. Lett.*, 30:1343–1346, 1973.

[11] H. J. Rothe. *Lattice Gauge Theories: An Introduction*. World Scientific, 2005.

[12] Gerhard Ecker. Chiral perturbation theory. *Progress in Particle and Nuclear Physics*, 35, 1997.

[13] S. Steininger and G. Meissner. Threshold kaon photo- and electroproduction in SU(3) baryon chiral perturbation theory. *Physics Letters B*, 391:446–450, 1997.

[14] R. A. Adelseck and B. Saghai. Kaon photoproduction: Data consistency, coupling constants, and polarization observables. *Phys. Rev. C*, 42:108, 1990.

[15] R. A. Adelseck and L. E. Wright. Electromagnetic production of kaons. *Phys. Rev. C*, 38:1966, 1988.

[16] J. C. David, C. Fayard, G. H. Lamot, and B. Saghai. Electromagnetic production of associated strangeness. *Phys. Rev. C*, 53:2614, 1996.

[17] S. S. Hsiao, D. H. Lu, and Shin Nan Yang. Pseudovector versus pseudoscalar coupling in kaon photoproduction reexamined. *Phys. Rev. C*, 61:68201, 1996.

[18] H. Thom. Phenomenological analysis of $K^+\Lambda$ photoproduction. *Phys. Rev.*, 151:1322–1336, 1966.

[19] A. Usov and O. Scholten. K-lambda and K-Sigma photoproduction in a coupled-channels framework. *Phys. Rev. C*, 72:025205, 2005.

[20] Wen-Tai Chiang, B. Saghai, and H. Lee F. Tabakin. Dynamical coupled-channel model of kaon-hyperon interactions. *Phys. Rev. C*, 69:65208, 2004.

[21] S. R. Cotanch, R. A. Williams, and C. R. Ji. Kaon electromagnetic production and radiative capture near hyperon thresholds. *Phys.Scripta*, 48:217–225, 1993.

[22] Particle Data Group D.E. Groom *et al. Eur. Phys. J. C*, 15:1, 2000.

[23] Stijn Janssen. *Strangeness Production on the Nucleon*. PhD thesis, Universiteit Gent, 2002.

[24] R. Dolen, D. Horn, and C. Schmid. Prediction of regge parameters of ρ poles from low-energy πN data. *Phys. Rev. Lett*, 19:402–407, 1967.

[25] R. Dolen, D. Horn, and C. Schmid. Finite-energy sum rules and their application to πN charge exchange. *Phys. Rev.*, 166:1768–1781, 1968.

[26] T. J. David, C. Fayard, G. H. Lamot, and B. Saghai. Electromagnetic production of associated strangeness. *Phys. Rev. C*, 53:2613, 1996.

[27] R. A. Williams, Chueng-Ryong Ji, and S. R. Cotanch. Hyperon electroproduction in a crossing and duality constrained model. *Phys. Rev. C*, 46:1617–1634, 1992.

[28] M. Benmerrouche, R. Davidson, and N. Mukhopadhyay. A new resonance in $K^+\Lambda$ electroproduction: The $D_{13}(1895)$ and its electromagnetic form factors. *Phys. Rev. C*, 39:2339, 1989.

[29] H. Haberzettl, C. Bennhold, T. Mart, and T. Feuster. Gauge-invariant tree-level photoproduction amplitudes with form factors. *Phys. Rev. C*, 58:R40, 1998.

[30] K. Ohta. Electromagnetic interactions of extended nucleons. *Phys. Rev. C*, 40:1335–1346, 1989.

[31] F. X. Lee, T. Mart, C. Bennhold, H. Haberzettl, and L. E. Wright. Quasifree kaon photoproduction on nuclei. *Nucl. Phys. A*, 695:237–272, 2001.

[32] T. Mart and T. Wijaya. Extending isobar model for kaon photoproduction up to 16 GeV. *Acta Phys. Polon. B*, 34:2651–2664, 2003.

[33] T. Mart and A. Sulaksono. Kaon photoproduction in a multipole approach. *Phys. Rev. C*, 74:055203, 2006.

[34] P. P. Bydžovský, M. Sotona, T. Motoba, K. Itonaga, K. Ogawa, and O. Hashimoto. Photo- and electro-production of medium mass Λ-hypernuclei. *arXiv:0706.3836 [nucl-th]*, 2007.

[35] T. Mizutani, C. Fayard, G.-H. Lamot, and B. Saghai. Off-shell effects in the electromagnetic production of strangeness. *Phys. Rev. C*, 58:75–90, 1998.

[36] P. Bydžovský and T. Mart. Analysis of the consistency of kaon photoproduction data with Λ in the final state. *Phys. Rev. C*, 76:065202, 2007.

[37] T. Mart. Progress and issues in the electromagnetic production of kaon on the nucleon. In *Strangeness in nuclear and hadronic systems, Sendai 08*, pages 2361–2363, December 2008.

[38] T. Azemoon *et al.* Production of hyperons by virtual photons. *Nucl. Phys.*, B95:77, 1975.

[39] C. J. Bebek *et al.* Scalar - transverse separation of electroproduced $K^+\Lambda$ and $K^+\Sigma^0$ final states. *Phys. Rev. Lett.*, D15:3082, 1977.

[40] P. Brauel *et al.* Electroproduction of π^+n, π^-p and $K^+\Lambda$ and $K^+\Sigma^0$ final states above the resonance region. *Zeit. Phys.*, C3:101, 1979.

[41] C. N. Brown *et al.* Coincidence measurements of single K^+ electroproduction. *Phys. Rev. Lett.*, 28:1086–1089, 1972.

[42] R. M. Mohring. *A comparison of the longitudinal and transverse cross sections in the* $e(p,e'K^+)\Lambda$ *and* $e(p,e'K^+)\Sigma^0$ *reactions*. PhD thesis, Faculty of the Graduate School of the University of Maryland, 1999.

[43] R. Bradford. Differential cross sections for $\gamma + p \rightarrow K^+ + Y$ for Λ and Σ^0 hyperons. *Phys.Rev.C*, 73:035202, 2006.

[44] M. Bockhorst *et al.* A new resonance in $K^+\Lambda$ electroproduction: The $D_{13}(1895)$ and its electromagnetic form factors. *Z. Phys. C*, 63:37–47, 1994.

[45] M. Q. Tran *et al.* Measurement of $\gamma p \to K^+\Lambda$ and $\gamma p \to K^+\Sigma^0$ at photon energies up to 2 GeV. *Phys. Lett. B*, 445:20–26, 1998.

[46] S. Goers *et al.* Measurement of $\gamma p \to K^0\Sigma^+$ at photon energies up to 1.55 gev. *Phys. Lett. B*, 464:331–338, 1999.

[47] R. Lawall *et al.* Measurement of the reaction $\gamma p \to K^0\Sigma^+$ at photon energies up to 2.6 GeV. *Eur. Phys. J. A*, 24(2):275–285, 2005.

[48] K. H. et al Glander. Measurement of $\gamma p \to K^+\Lambda$ and $\gamma p \to K^+\Sigma^0$ at photon energies up to 2.6 GeV. *Eur. Phys. J.*, A19:251–273, 2004.

[49] T. Mart and C. Bennhold. Evidence for a missing resonance in kaon photoproduction. *Phys. Rev. C*, 61:012201(R), 2000.

[50] R. G. T. Zegers *et al.* Beam-polarization asymmetries for the $p(\vec{\gamma}, K^+)\Lambda$ and $p(\vec{\gamma}, K^+)\Sigma^0$ reactions for E_γ = 1.5-2.4 GeV. *Phys. Rev. Lett.*, 91:092001, 2003.

[51] M. Sumihama *et al.* The $\gamma p \to K^+\Lambda$ and $\gamma p \to K^+\Sigma^0$ reactions at forward angles with photon energies from 1.5 to 2.4 GeV. *Phys.Rev. C*, 73:035214, 2006.

[52] A. Lleres *et al.* Polarization observable measurements for $\gamma p \to K^+\Lambda$ and $\gamma p \to K^+\Sigma^0$ for energies up to 1.5 GeV. *Eur. Phys. J. A*, 31:79–93, 2007.

[53] A. Lleres *et al.* Measurement of beam-recoil observables Ox ,Oz and target asymmetry t for the reaction $\gamma p \to K^+\Lambda$. *Eur. Phys. J. A*, 39(2):149–161, 2008.

[54] P. P. Bydžovský and T. Mart. Analysis of the data consistency on kaon photoproduction with lambda in the final state. *Phys. Rev.*, C76:065202, 2007.

[55] C. Paterson. *Polarization observables in strangeness photoproduction with CLAS at Jefferson Lab*. PhD thesis, University of Glasgow, 2098.

[56] R. Bradford. First measurement of beam-recoil observables cx and cz in hyperon photoproduction. *Phys.Rev.C*, 75:035205, 2007.

[57] T. Mart. Electromagnetic productions of $K\Lambda$ and $K\Sigma$ on the nucleons. *AIP Conf. Proc.*, 31:1056, 2008.

[58] D. S. Carman *et al.* First measurement of transferred polarization in the exclusive $\vec{e}p \to K^+\vec{\Lambda}$. *Phys. Rev. Lett.*, 90:131804, 2003.

[59] R. Nasseripour *et al.* Polarized structure function $s_{LT'}$ for $^1H(\vec{e}, e'K^+)\Lambda$ in the nucleon resonance region. *Phys. Rev.*, C77:065208, 2008.

[60] A. Jankowiak. The Mainz microtron MAMI –past and future. *Eur. Phys. J. A*, so1 28:149–160, 2006.

[61] K. H. Kaiser *et al.* The 1.5 GeV harmonic double-sided microtron at mainz university. *Nuclear Instruments and Methods in Physics Research A*, 593:159–170, 2008.

[62] T. Pospischil. *Aufbau und Inbetriebnahme eines Protonen-Polarimeters an MAMI und Messung der Proton-Polarisation in der Reaktion* $p(\vec{e}, e'\vec{p})\pi^0$ *in paralleler Kinematik im Bereich der D(1232) resonanz*. PhD thesis, Institut für Kernphysik, Johannes Gutenberg-Universität Mainz, 2000.

[63] Lars Nungesser. *Aufbau und Simulation des Kaos-Spektrometers für Koinzidenzmessungen in der assoziierten Kaonproduktion*. PhD thesis, Institut für Kernphysik, Johannes Gutenberg-Universität Mainz, 2009.

[64] M. Bösz. Datenerfassung und spurerkennung mit den vieldrahtproportionalkammern für das kaos-spektrometer an mami. Diplomarbeit, 2009.

[65] K. I. Blomqvist *et al.* The three-spectrometer facility at the mainz microtron MAMI. *Nucl. Instr. and Meth. Phys. Res. A*, 403:263–301, 1998.

[66] P. Achenbach *et al.* Particle tracking in kaon electroproduction with cathode-charge sampling in multi-wire proportional chambers. *Nucl. Instr. and Meth. A*, 641:105–113, 2011.

[67] Florian Schulz. *Teilchenidentifikation unter kleinen Streuwinkeln in der Pionzerfallsspektroskopie von Hyperkernen*. PhD thesis, Institut für Kernphysik, Johannes Gutenberg-Universität Mainz, 2011.

[68] T. Mart and C. Bennhold. An effective lagrangian model for kaon photo and electroproduction on the nucleon. *Phys. Rev. C*, 61:012201, 2000.

[69] K. H. Glander. Measurement of $\gamma p \to K^+\Lambda$ and $\gamma p \to K^+\Sigma^0$ at photon energies up to 2.6 GeV. *Eur. Phys. J. A.*, 19:251, 2004.

[70] M. E. McCracken. Differential cross section and recoil polarization measurements for the $\gamma p \to K^+\Lambda$ reaction using CLAS at Jefferson lab. *Phys. Rev. C*, 81:025201, 2010.

[71] P. Achenbach *et al.* Exclusive electroproduction of $K^+\,\Lambda$ and $K^+\,\Sigma^0$ final states at Q^2 = 0.030-0.055 $(GeV/c)^2$. *arXiv:1104.4245*, 2011.

[72] S. Jannsen, J. Ryckebusch, and T. Van Cauteren. Constraints on background contributions from $K^+\Lambda$ electroproduction. *Phys. Rev. C*, 67:052201, 2003.

[73] R. Bradford *et al.* Differential cross sections for $\gamma + p \to K^+ + Y$ for Λ and Σ^0 hyperons. *Phys.Rev.C*, 73:035202, 2006.

[74] Ambrozewicz *et al.* Separated structure functions for the exclusive electroproduction of $k^+\lambda$ and $k^+\sigma^0$ final states. *Phys. Rev. C*, 75:045203, 2007.

[75] J. Pochodzalla. Future of hypernuclear physics at MAMI-C and PANDA-GSI. *Nucl. Phys. A*, 754:430c, 2005.

[76] P. Achenbach. Probing hypernuclei at $\overline{\mathrm{P}}$ANDA and at MAMI-C. In Th. Walcher J. Pochodzalla, editor, *J. Pochodzalla, Th. Walcher (Eds.), Proceedings of the IX International Conference on Hypernuclear and Strange Particle Physics, Johannes Gutenberg-Universität, Mainz, 10–14 October 2006*, page 79, Berlin/Heidelberg, 2007. Springer.

[77] M. Mazzillo *et al.* Silicon photomultipliers for nuclear medical imaging applications. In *Optical sensors 2008*, 2008.

[78] P. Buzhan et al. An advanced study of silicon photomultiplier. *ICFA Instr. Bull.*, 23:28–41, 2001.

[79] Dolgoshein. Silicon photomultipliers in particle physics: Possibilities and limitations. In *Proceedings of the 42nd Workshop on Innovative Detectors for Supercolliders*, pages 79–84, Erice, Italy, 2004. World Scientific.

[80] B. Dolgoshein et al. Status report on silicon photomultiplier development and its applications. *Nucl. Instr. and Meth. A*, 563:368–376, 2006.

[81] Giancarlo Barbarino *et al. Photodiodes - World Activities in 2011. Chapter: Silicon Photo Multipliers Detectors Operating in Geiger Regime: an Unlimited Device for Future Applications*. InTech, 2011.

[82] N. A. Amos et al. Optical attenuation length measurements of scintillating fibers. *Nucl. Instr. and Meth. A*, 297:396–403, 1990.

[83] S. Sánchez Majos, P. Achenbach, and J. Pochodzalla. Characterization of radiation damage in silicon photomultipliers with a monte carlo model. *Nucl. Instr. and Meth. A*, 594:351, 2008.

[84] C. Leroy and P.G. Rancoita. Particle interaction and displacement damage in silicon devices operated in radiation environments. *Rep. Prog. Phys*, 70:493–625, 2007.

[85] Y. Musienko et al. Radiation damage studies of multipixel geiger-mode avalanche photodiodes. *Nucl. Instr. and Meth. A*, 581:433, 2007.

[86] P. Achenbach *et al.* New detectors for the kaon and hypernuclear experiments with KAOS at MAMI and with $\overline{\text{P}}$ANDA at GSI. In V. Luth, editor, *Proceedings of the IX International Symposium on Detectors for Particle, Astroparticle and Synchrotron Radiation Experiments*, page 144. eConf C0604032, 2006.

[87] G. P. Summers *et al.* Damage correlations in semiconductors exposed to gamma, electron and photon radiation. *IEEE Trans. Nucl. Sci.*, NS-40:1372, 1993.

[88] S.R. Messenger *et al.* Nonionizing energy loss (NIEL) for heavy ions. *IEEE Trans. Nucl. Sci.*, NS-46:1595, 1999.

[89] D. Renker. Geiger-mode avalanche photodiodes, history, properties and problems. *Nucl. Instr. and Meth. A*, 567:48–56, 2006.

[90] N. Otte. The silicon photomultiplier a new device for high energy physics, astroparticle physics, industrial and medical applications. In *Proceedings of the IX International Symposium on Detectors for Particle, Astroparticle and Synchrotron Radiation Experiments*, page 18, 2006.

[91] P. Eraerds, M. Legré, A. Rochas, H. Zbinden, and N. Gisin. SiPM for fast photon-counting and multiphoton detection. *Opt. Express*, 15:14539–14549, 2007.

[92] John R. Taylor. *Scattering Theory: The Quantum Theory on Nonrelativistic Collisions*. John Wiley and Sons, Inc., 1972.

[93] Albert Messiah. *Quantum Mechanincs Volume I*. North-Holland publishing company Amsterdam, 1961.

[94] James D. Bjorken and Sidney D. Drell. *Relativistic Quantum Mechanincs*. McGraw-Hill, 1964.

[95] I. J. R. Aitchison and A. J. G Hey. *Gauge theories in Particle Physics. Volume I: From Relativistic Quantum Mechanincs to QED*. Institute of Physics publishing, London, 1996.

[96] John Dirk Walecka. *Electron scattering for nuclear and nucleon structure*. Cambridge University Press, 2001.

[97] L. L. Foldy and J. D. Walecka. On the theory of the optical potential. *Ann. of Phys.*, 54:447–504, 1969.

[98] S. Nozawa and T. S. H. Lee. Electroproduction of pions on the nucleon (ii). polarization observables. *Nuclear Physics A*, 513:543–556, 1990.

[99] V. Dmitrasinovic and F. Gross. Polarization observables in deuteron photodisintegration and electrodisintegration. *Phys. Rev. C*, 40(6), 1989.

[100] N. Dombey. Hadronic interactions of electrons and photons. In J. Cumming, editor, *Proceedings of the eleventh session of the scottish universities summer school in Physics,1970*, pages 17,45, Glasgow, 1970. Academic Press London and New York.

LIST OF FIGURES

Figure 1 Predicted resonances 5
Figure 2 The electron scattering and hadronic reaction planes in the lab frame 9
Figure 3 Born and extended born terms 12
Figure 4 Resonant contributions 13
Figure 5 Contributions of the different resonances to the total cross-section 17
Figure 6 photon 19
Figure 7 Old data 20
Figure 8 DESY spectrometers 21
Figure 9 Saphir data 22
Figure 10 Rastered beam profile in calibration screen 26
Figure 11 Plan of accelerator facilities and experimental halls 27
Figure 12 Cryo target scheme 28
Figure 13 Experimental hall of the A1 collaboration 30
Figure 14 Detectors equipping KAOS spectrometer 31
Figure 15 Elastically scattered electrons of 450 MeV energy, back-traced from the detector system of the Kaos spectrometer to the target. 34
Figure 16 Electrodes and electric field configuration of MWPC 35
Figure 17 Efficiency MWPC 36
Figure 18 Scheme of scintillator walls electronics 37
Figure 19 Calibration ADC spectrum of a sample paddle 38
Figure 20 Absorption fits for F 39
Figure 21 FG trigger 40
Figure 22 Photographs of first (left) and second generation (right) FPGA logic modules: VULOM and VUPROM used in the tracking trigger for the positive-arm of the KAOS spectrometer. Both VME modules were equipped withs VIRTEX-4 FPGA chips and flash memory. Different trigger programs could be loaded into the FPGA via a JTAG connector or directly by means of the VME interface. VUPROM allowed a larger number of channels to be handled by the same module (256 I/O channels) by means of high density connectors. 42
Figure 23 KAOS-scheme 43

Figure 24 Spek B dipole optics 44
Figure 25 Detectors equipping spectrometer B 45
Figure 26 Simplified scheme of coincidence electronics 46
Figure 27 Diagram of tracking logic 47
Figure 28 Clusters in MWPC 53
Figure 29 Efficiency counters 56
Figure 30 Reconstructed x and y coordinates in MWPC L at 2 and 4 uA beam currents 57
Figure 31 Event display 58
Figure 32 Q^2 distributions of $\sigma_T + \epsilon\sigma_L$ 59
Figure 33 Anomalous band in Δt vs Gy 60
Figure 34 Vertical band in M chamber removed by time difference quality factor 60
Figure 35 ADC spectrum for G paddle within the acceptance of the efficiency counters 61
Figure 36 Q^2 distributions of $\sigma_T + \epsilon\sigma_L$ 62
Figure 37 Radiation damage on F scintillators 63
Figure 38 Inefficiencies due to the F wall gaps 64
Figure 39 Scintillator Walls extension 65
Figure 40 New scintillator wall integrated in Kaos detector system 66
Figure 41 Diagnostic test applied to physics runs 68
Figure 42 69
Figure 43 Fit for gain correction factors 71
Figure 44 Example of the outcomes of the program used for the cut efficiency determination 72
Figure 45 Missing mass spectrum in the $p(e, e'K^+)\Lambda, \Sigma^0$ reaction 73
Figure 46 Coincidence time spectra for the $p(e, e'K^+)$ reaction 74
Figure 47 Predictions of Kaon-Maid and Saclay Lyon isobaric models for scaling 76
Figure 48 Phase-space for kaon scattering angle vs. kaon momentum 77
Figure 49 Detection efficiency as a function of momentum for the case where decaying particles are accepted or not 78
Figure 50 Differential cross sections of kaon electroproduction scaled to the center of the experimental acceptance 82
Figure 51 Angular dependence of the total electroproduction cross section 83
Figure 52 Dependence of the kaon electroproduction cross sections on the virtual photon's four-momentum Q^2 84

Figure 53 Predictions for the separated and total cross sections in the Λ electroproduction channel from the original K-Maid model 85
Figure 54 Q^2 distributions of $\sigma_T + \epsilon\sigma_L$ 86
Figure 55 SiPM matrix 90
Figure 56 Experimental set-up for SiPM characterization 92
Figure 57 Charge spectrum obtained by UV laser excitation of the scintillating fiber 93
Figure 58 Signal gain as a function of bias voltage 93
Figure 59 Modular plexiglas device used for measurements of the SiPM/fiber performance 94
Figure 60 Measurement of light attenuation in a $2 \times 2\,mm^2$ 95
Figure 61 Fired pixels as a function of overvoltage 96
Figure 62 Measurement of the accidental coincidence rate for a threshold of 1.5 pixels as a function of overvoltage 97
Figure 63 Results of a GEANT simulation for the average energy deposition in the studied fiber as a function of the energy threshold demanded in the trigger detector 99
Figure 64 Numerical calculation of the accidental coincidence rate vs. fiber thickness, for matching detector area 100
Figure 65 Result of a numerical convolution of the propagation time distribution and scintillator decay curve 101
Figure 66 Result of the Monte Carlo simulation on detection efficiency as a function of threshold level and hit position 102
Figure 67 Experimental set-up for SiPM characterization 104
Figure 68 Experimental set-up for SiPM irradiation 105
Figure 69 ADC spectra for low amplitude signals from green sensitive Photonique SiPM before and after irradiation 106
Figure 70 ADC spectra for fixed laser intensity after irradiation with 30.8, 77.0, 123, 185, 262 and 385×10^8 electrons 107
Figure 71 Noise spectra of a green sensitive Photonique SSPM-0701BG-TO18 device that was exposed to background irradiation close to the beam-line during one week of normal beam operation 108
Figure 72 Noise spectra of blue sensitive Photonique SSPM-0611B1MM devices before and after irradiation close to the beam-line 108

Figure 73 Annealing at 80° of the SiPM exposed to the radiation field in the experimental hall 109
Figure 74 Oscilloscope trace of optical cross-talk 110
Figure 75 Independent clusters in which three pixels have been fired 111
Figure 76 Signals generated by the MPHD model 112
Figure 77 Measured pulse-height spectra for five different bias voltages 113
Figure 78 Measured noise rate as a function of discriminator threshold for a bias voltage of 17.9 V 115
Figure 79 Measured noise rate before and after irradiationas as a function of threshold in a leading edge discriminator 115
Figure 80 Pulse-height spectra after irradiation with 3.1×10^{8} electrons/mm^2 of 14 MeV energy for low amplitude signals 116
Figure 81 Geometry of the lepton scattering plane 130
Figure 82 Electronic and hadronic planes in CM 131

LIST OF TABLES

Table 1 Model Kaon-Maid for Λ and Σ^0 production. Parameters of assumed resonances. 16
Table 2 Model Saclay-Lyon for Λ and Σ^0production. Parameters of assumed resonances. 18
Table 3 Spectrometers properties 33
Table 4 Laboratory kinematics of the kaon electroproduction campaigns 48
Table 5 Tracking efficiencies for different beam currents 62
Table 6 Gain correction factors 70
Table 7 Low Q^2 kaon electroproduction experiments 75
Table 8 Systematic corrections and errors in the analysis 79
Table 9 Measured detection efficiencies, ε, and accidental coincidence rates, R_{acc}, for different threshold amplitudes, N_{thr}, and SiPM overvoltages 97
Table 10 MPHD model results for five bias voltages 114